CHARACTERIZATION OF ARTICULAR CARTILAGE, CHONDROCYTE AND BONE PROPERTIES USING NANO- AND MICROSCALE TECHNIQUES

Teză destinată obţinerii
titlului ştiinţific de doctor inginer
la
Universitatea Politehnica Timişoara
în domeniul INGINERIE MECANICĂ
de către

Ing. Cristina Florea

Conducători ştiinţifici:	Prof. univ. dr. ing. Arjana Davidescu Conf. univ. dr. fiz. med. Rami Korhonen
Referenţi ştiinţifici:	Conf. univ. dr. fiz. med. Mikko Hakulinen Conf. univ. dr. med. Romulus-Fabian Tatu Prof. univ. dr. ing. Viorel-Aurel Şerban
Ziua susţinerii tezei:	09.05.2014

Seriile Teze de doctorat ale UPT sunt:

1. Automatică
2. Chimie
3. Energetică
4. Ingineria chimică
5. Inginerie civilă
6. Inginerie electrică
7. Inginerie electronică şi telecomunicaţii
8. Inginerie industrială
9. Inginerie mecanică
10. Ştiinţa calculatoarelor
11. Ştiinţa şi ingineria materialelor
12. Ingineria sistemelor
13. Inginerie energetică
14. Calculatoare şi tehnologia informaţiei
15. Ingineria materialelor
16. Inginerie şi management

Universitatea Politehnica Timişoara a iniţiat seriile de mai sus în scopul diseminării expertizei, cunoştinţelor şi rezultatelor cercetărilor întreprinse în cadrul şcolii doctorale a universităţii. Seriile conţin, potrivit H.B.Ex.S Nr. 14 / 14.07.2006, tezele de doctorat susţinute în universitate începând cu 1 octombrie 2006.

România, 300159 Timişoara, Bd. Republicii 9,
tel. 0256 403823, fax. 0256 403221
e-mail: editura@edipol.upt.ro

Preface

This thesis was done in a joint degree between Politehnica University of Timişoara, Romania under the supervision of Prof. Arjana Davidescu in the Department of Mecatronics and University of Eastern Finland, Finland, under the supervision of Assoc. Prof. Rami Korhonen in the Department of Applied Physics.

First of all, I would like to thank my supervisor Prof. Arjana Davidescu from Politehnica University of Timişoara for her help in finalizing this thesis. Special thanks to Assoc. Prof. Rami Korhonen, my co-supervisor, for being always there, supporting and responding to any question I had, so quickly and also for creating such a stimulating research and social environment. Many thanks for his support in the last few months of my thesis in which I felt really in need for. I would also like to thank him for the "ranch" parties organized at his place with the whole research group. I would like to express my deep gratitude to my former supervisor Prof. Mircea Dreucean, for encorouraging me to start this PhD journey. Sadly, he passed away much too soon and left a great emptiness in our hearts. This journey would have not been possible without his support and I, therefore, dedicate this thesis to him.

I further would like to thank the members of my dissertation committee: Dr. Mikko Hakulinen, Prof. Aurel-Viorel Serban and Dr. Romulus-Fabian Tatu, for their ideas, comments and constructive criticism to improve this thesis. I would like to thank my co-authors Dr. Mika Mononen, Markus Malo, Prof. Jukka Jurvelin, Prof. Mikko Lammi, Prof. Miika Nieminen, Dr. Mikko Laasanen, Asmo Jakorinne, Petri Tanska, Jari Rautiainen, Janne Mäkelä, for their contributions. I owe my sincere thanks and gratitude to Dr. Mikko Laasanen for valuable insight into the Atomic force microscopy world that has immensely influenced this research. I would like to thank my colleague and friend Ari Halvari, for offering me practical support in AFM nanoindentation and a whole-hearted friendship.

I owe special thanks to my colleagues from the Cell and Tissue Biomechanics and Biophysics of Bone and Cartilage research groups for the many invaluable discussions and constant help. Special thanks go to Dr. James Fick for the encouragement and interesting talks related to the cartilage research. I would like to acknowledge the staff of the Institute of Biomedicine for their efforts on the sample preparation and all related issues. In addition, I would like to thank all my friends in Kuopio, who gave me the necessary distractions from my research and made my stay in Finland memorable. Also, I thank all my friends from Romania, in particular to Karla Kun for the encouragement and support to complete this thesis.

The following sources of funding are acknowledged: POSDRU Romania 2007-2013 co-financed by the European Social Fund POSDRU/CPP107/DMI1.5/S/ 77265 (2010), Doctoral Programme in Medical Physics and Engineering, Sigrid Juselius Foundation, European Research Council (grant 281180), Magnus Ehrnrooth Foundation and International Doctoral Programme in Biomedical Engineering and Medical Physics. I acknowledge Atria Suomi Oy, Kuopio, Finland for providing bovine joints as research material.

Finally, my deep and sincere gratitude to my family, especially my mother and my fiancée for their continuous love and support and their deep believe in my capabilities.

Timişoara, April 2014 Eng. Cristina Florea

To Prof. Dr. Eng. Mircea DREUCEAN, with my highest consideration.

This thesis was jointly supervised between *Politehnica University of Timişoara, Romania* and *University of Eastern Finland, Kuopio, Finland.*

Thesis title: Characterization of articular cartilage, chondrocyte and bone properties using nano- and microscale techniques

Thesis author: Eng. Cristina Florea

Supervisors:

Prof. Dr. Eng. Arjana Davidescu	*Politehnica University of Timişoara*
Assoc. Prof. Dr. Rami Korhonen	*University of Eastern Finland*

Reviewers:

Assoc. Prof. Dr. Med. Phys. Mikko Hakulinen	*Kuopio University Hospital*
Assoc. Prof. Dr. Med. Romulus-Fabian Tatu	*"Victor Babes" University of Medicine and Pharmacy of Timişoara*
Prof. Dr. Eng. Viorel-Aurel Şerban	*Politehnica University of Timişoara*

Opponent:

Asst. Prof. Nadeen Chahine	*The Feinstein Institute for Medical Research, New York*

Thesis defense date: 13.06.2014, Kuopio, Finland

Florea, Cristina

Characterization of articular cartilage, chondrocyte and bone properties using nano- and microscale techniques

Teze de doctorat ale UPT, Seria 9, Nr. 151, Editura Politehnica, 2014, 115 pagini, 31 figuri, 7 tabele.

ISSN:1842-4937

ISBN:978-606-554-836-7

Cuvinte cheie:
microscop de forţă atomică, nanoindentare, cartilaj, os, condrocite, microtomografie computerizată, secţionarea ligamentului incrucişat anterior

Rezumat,
Această cercetare a îmbinat progresele recente din domeniul ingineriei la scară nano- cu diferite tehnici experimentale la scară micro- pentru a evalua relaţia structură-funcţionalitate a cartilajului articular şi a osului subcondral atât la nivel celular cât şi la nivel tisular.

TABLE OF CONTENTS

INDEX OF FIGURES

INDEX OF TABLES

LIST OF ABBREVIATIONS AND SYMBOLS

2D	Two-dimensional
3D	Three-dimensional
AC	Alternating current
ACL	Anterior cruciate ligament
ACLT	Anterior cruciate ligament transection
AFM	Atomic force microscopy
AU	Absorption unit
BAF2	Barium floride
BV/TV	Bone volume fraction
CCD	Charge-coupled device
CL	Non-operated control
Cr-Au	Chromium gold
CT	Computed tomography
CTRL	Contralateral control
CV	Coefficient of variation
CytoD	Cytochalasin D
DD	Digital densitometry
DMEM	Dulbecco's modified Eagle's medium
DNase	Deoxyribonuclease
ECM	Extracellular matrix
EDTA	Ethylenediaminetetra-acetic acid
FC	Femoral condyle
FCS	Fetal calf serum
FE	Finite element
FE-SEM	Field emission scanning electron microscopy
FTIR	Fourier transform infrared
GAG	Glycosaminoglycan
Glc	Glucose
IR	Infrared
Lat	Lateral
LCL	Lateral collateral ligament
MCL	Medial collateral ligament
Med	Medial
Micro-CT	Micro-computed tomography
MRI	Magnetic resonance imaging
MSE	Mean squared error
OA	Osteoarthritis
OD	Optical density
PBS	Phosphate buffered saline
PCL	Posterior cruciate ligament
PCM	Pericellular matrix
PG	Proteoglycan
PLM	Polarized light microscopy
PSPD	Position-sensitive photodetector
Pt.Th	Subchondral bone plate thickness
REML	Restricted maximum likelihood

SD	Standard deviation
SMI	Structural model index
STM	Scanning tunneling microscopy
Tb.Sp	Trabecular separation
Tb.Th	Trabecular thickness
VOI	Volume of interest
Z_{scan}	Displacement of the piezoelectric scanner
A	Oscillation amplitude of the cantilever
A_b	Absorbance
a'	Inner radius of the micropipette
a_1	Wavelength-dependent absorptivity coefficient
a_c	Contact radius
α	Rotation angle of the polarization plane
$\bar{B}$	Cauchy-Green deformation tensor
b	Thickness
c_a	Concentration
C_{10}, D_1	Material constants dependent on temperature
d	Cantilever deformation
δ	Material deformation
E	Young's modulus
E_0	Instantaneous modulus
E_∞	Relaxation modulus
e	Volumetric change
e_0	Initial void ratio
ε	Strain
ε'	Indentation depth
ε_s	Infinitesimal strain tensor
F	Force
ΔF	Applied external suction pressure
$\bar{F}$	Deformation gradient tensor
f	Resonant frequency
$\phi_P(\eta)$	Function of the inner and outer radii of the micropipette
ϕ^s, ϕ^f	Volume fractions for solid and fluid phase
$\bar{g}_i^p$	Shear relaxation modulus
H_A	Aggregate modulus
θ	Reflection angle
ν	Poisson's ratio
μ	Apparent viscosity
I	Unit tensor
$\bar{I}_1$	First deviatoric strain invariant
I'	Intensity of light
I_0	Initial intensity of light
J	Elastic volume ratio
K_0	Bulk modulus
k	Permeability
k'	Cantilever spring constant
k_B'	Boltzmann's constant
L	Length
λ_i	Principal stretches
$\bar{\lambda}_i$	Deviatoric stretches
λ_s, μ_s	First and second Lamé constants for the solid phase

$\Gamma_i(\omega)$	Hydrodynamic function of the cantilever
m	Cantilever mass
m^*	Added mass
m_0	Effective mass
η	Coefficient of viscosity
Q	Quality factor
p	Hydrostatic pressure
S_0	Stokes parameter, total intensity of light
S_1	Stokes parameter, amount of linear/horizontal polarization
S_2	Stokes parameter, amount of $+45^o$ or -45^o polarization
S_3	Stokes parameter, amount of right or left circular polarization
σ	Stress
σ_{rr}	Radial component of the Cauchy stress tensor
$\sigma_{\theta\theta}$	Circumferential component of the Cauchy stress tensor
σ_{rz}	Shear components of the Cauchy stress tensor
σ_s	Cauchy stress tensor
σ_{zz}	Axial component of the Cauchy stress tensor
ρ	Density
T	Transmittance
t	Time
τ_1	Relaxation time
U	Strain energy density function
w	Width
ψ	Orientation angle of a polarization ellipse
ω	Radial resonant frequency

ABSTRACT

Osteoarthritis (OA) is a debilitating joint disease affecting not only articular cartilage, but also the whole joint, including the bone. During OA, structural and mechanical changes occur in both structures at tissue and cellular scales. In fact, changes occurring at the nano- and microscale reflect in the macroscale properties of articular cartilage and bone. The ability to assess these changes can provide valuable insights into health and disease. This thesis explores the applications of different nano- and micro techniques with the end goal of characterizing the biomechanical and structural properties of articular cells, cartilage and underlying bone.

Articular cartilage is composed of cells and extracellular matrix that consist mainly of interstitial fluid, collagen and proteoglycans (PGs). Chondrocytes, the sole cellular component of cartilage, are remarkable because they produce all the matrix components and thus are crucial to the structural integrity and biomechanical function of the tissue. Moreover, it has been shown that the chondrocytes actively respond to mechanical stimuli by modulating their mechanical microenvironment. However, the mechanisms by which mechanical loading modulates single chondrocyte behavior are not fully understood and may involve changes in the local mechanical properties of the chondrocyte or in the intracellular structural components. Degradation of the intracellular structural components has a major influence on the mechanical behavior of the chondrocytes, which leads to dysfunction with age, injury and disease, such as OA.

Located just underneath the articular cartilage, subchondral bone includes the subchondral bone plate and the underlying trabecular bone and has an important role in maintaining the integrity of the articular cartilage. Changes in both subchondral bone plate and trabecular bone architecture could lead to altered loading patterns, which may play a crucial role in the OA initiation and progression. While the contribution of the cartilage and subchondral bone in advanced OA is well-studied, little is known about the role of subchondral bone at the onset of the disease.

Atomic force microscope (AFM) is a unique tool for probing the local mechanical properties of single cells at nanolevel. For this purpose, a reliable AFM methodology was initially developed using a nanoindenter tip to quantify the local elastic properties of soft materials (agarose gel) using the traditional Hertz model. Furthermore, single cell stress-relaxation curves were acquired at 5%, 10% and 15% deformation of the cell thickness and consequently the elastic modulus was determined. The elastic modulus of the chondrocytes decreased with increasing indentation, indicative of non-linear chondrocyte mechanical properties due the combined effects of mechanical properties of the membrane and underlying cytoskeleton. Moreover, hindering the formation of the actin cytoskeleton using a disrupting agent Cytochalasin D led to a statistically significant decrease of the cell elastic properties only at 5% of the cell thickness. In fact, by disrupting the actin cytoskeleton located at the cortical region of the chondrocytes, there were no significant changes between elastic modulus at 5%, 10% and 15% of the cell thickness. These results suggest that the actin cytoskeleton may contribute to the non-linear mechanical response of chondrocytes in nanoindentation. Moreover,

chondrocytes exhibit viscoelastic behavior in response to an applied stress. This has been attributed to flow-independent mechanisms (viscoelasticity of the cytoskeleton) as well as flow-dependent mechanisms (fluid-solid interactions) or combination of those two. However, the mechanisms that govern the viscoelastic behavior of chondrocytes under nanoindentation are largely unknown. To address this question, a combined approach of experimental AFM nanoindentation with computational modeling was proposed, taking into account more complex material models (hyperporoelastic, hyperviscoelastic, hyperporoviscoelastic). The AFM experimental stress-relaxation responses of chondrocytes were captured the best using the hyperporoviscoelastic model. This suggests that the viscoelasticity of chondrocytes under nanoindentation is due to the combination of both intrinsic viscoelastic phenomena and biphasic behavior. Understanding the mechanical responses of single chondrocytes and quantifying their mechanical properties is crucial for understanding normal cell physiological behavior as well as elucidating the pathogenesis of OA.

Further, the need to clarify the early events that occur at tissue level in both cartilage and underlying bone at the onset and during the early progression of OA has motivated the use of animal models. Although, cartilage structural and compositional changes have been previously studied in a rabbit model of early OA, it is still not known whether these changes in cartilage occur concurrently with structural changes in the underlying bone. For this purpose, a high resolution micro-computed tomography scanner was used to assess the three-dimensional microarchitecture and volume in the subchondral bone plate and trabecular bone. Additionally, depth-wise changes in the proteoglycan content, collagen orientation angle and collagen content as well as biomechanical properties of cartilage were quantified using digital densitometry, polarized light microscopy, Fourier transform infrared microspectroscopy and indentation testing, respectively. The experiments revealed that the very early OA changes of cartilage preceded those of subchondral and trabecular bone in the lateral knee joint compartment, while in the medial compartment, cartilage and bone experienced degenerative alterations simultaneously. This study highlights the importance of considering both cartilage and bone and abnormal joint loading in the initiation of OA, which occur in a highly site-specific manner.

In conclusion, the combination of nano- and microscale techniques used in this thesis were proven to be useful tools to study structural and biomechanical properties of cartilage at tissue and cell level and underlying bone as well. A better understanding of the cross-scale structural and mechanical relations in biological tissues such as articular cartilage and subchondral bone may help to elucidate the role of each component in health and disease. Additionally, the results of this research contribute to the fundamental understanding of tissue and cell biomechanics at different length and time scales.

1. INTRODUCTION

Hundreds of millions of people worldwide suffer from various forms of arthritis, of which the most common is osteoarthritis (OA), characterized by joint pain, stiffness and limited range of motion. By the year 2020, based on current trends, osteoarthritis (OA) is predicted to become the fourth leading cause of disability worldwide (Woolf and Pfleger 2003). In OA, all the joint structures are altered so the proper joint functioning is no longer possible. The main pathological OA feature includes loss of articular cartilage eventually leading to exposure of the subchondral bone, but other joint components undergo pathological changes as well. To date, there is no effective treatment to attenuate or cure the degradation of the articular cartilage in progressive OA and many people in severe OA must undergo joint replacement surgery. In addition, little is known about early changes that occur in articular cartilage and subchondral bone before OA becomes clinically detectable. In OA, changes occurring at the nanoscale spread to the higher levels of the architecture of the tissue, causing progressive and irreversible functional and structural damage. Understanding the mechanical properties of single chondrocytes and even of the whole tissues in health and disease continues to pose significant challenges.

Both, articular cartilage and subchondral bone are complex biomaterials which exhibit superior mechanical properties, a feature that can be related to their functional adaptations and structural interactions at multiple hierarchical levels, from nano- to macroscale. This has motivated an increasing interest in combining engineering, material science and physics approaches with the biological and medical sciences, leading to interdisciplinary investigations of biomechanical and structural properties of biological tissues across different length scales. In this thesis, nano- and microscale experimental techniques and computational modeling were used to investigate the structure-function relationships of cartilage and underlying bone at cellular and tissue levels in health and disease.

At cellular level, articular chondrocytes possess a high degree of structural hierarchy and heterogeneity coupled with active biochemical processes that constantly remodel their internal structure. The chondrocyte cytoskeleton is suggested to have a fundamental role in the biomechanical nature and structure of the cell and acts as a physical interface between the cell and extracellular matrix in "sensing" mechanical stimuli (Grodzinsky et al. 2000; Guilak 1995; Wang et al. 1993). Moreover, chondrocytes produce and organize the molecular building blocks and maintain the collagen-preoteoglycan extracellular cartilage solid matrix through a balanced metabolic process. At the tissue-scale, articular cartilage possesses a set of unique nonlinear, anisotropic and inhomogeneous material properties that seem to have been specifically designed to provide excellent tribological functions at extremely high loads. Cartilage material properties depend primarily on the properties of the extracellular matrix, which mainly consists of collagen fibrils and negatively charged proteoglycans. At macrolevel, articular cartilage is the bearing tissue that provides the smooth, near frictionless function required in synovial joints.

In OA, the complex metabolic balance of cartilage is disrupted, marked by increased catabolism and decrease in matrix protein synthesis. This has a profound

effect on both collagen and PG quality and quantity in the extracellular matrix, which in turn will lead to altered mechanical properties of the cartilage matrix. The resulting high stress level can lead to cell death or abnormal cell metabolism, both evident will influence on the matrix maintenance. Alterations in the structural integrity, composition and mechanical properties of articular cartilage can be observed not only at the tissue level but also at the cellular level. Significant changes in elastic and viscoelastic properties were observed in OA chondrocytes from end-stage pathology (Trickey et al. 2000).

Atomic force microscopy (AFM) is a nanoscale technique with high sensitivity first developed in imaging hard engineering materials. For the past two decades, AFM has been widely used to examine the mechanical properties of various cell types (Kuznetsova et al. 2007). However, there is a large variation in the reported values for the mechanical properties of various single cells. By taking into account the main uncertainty sources inherent to AFM measurements (e.g. calibration of the cantilever spring constants and tip radii) and developing a reliable methodology, the local elastic and viscoelastic properties of single cells can be determined more accurately. Although, the contribution of cytoskeleton to the cellular mechanical properties has been previously studied in AFM nanoindentation (Chahine et al. 2013), less is known about its contribution to the local elastic and viscoelastic properties of the single chondrocytes. In particular, the strain-dependent local elastic and viscoelastic behaviour of chondrocytes still remain unknown. Understanding the local changes in cell cytoskeletal components is an important step in understanding the mechanobiology of single chondrocytes and the pathogenesis of OA.

To extract the local mechanical properties of cells, experimental AFM nanoindentation data must be mathematically modeled using an appropriate model for the cell material. Both elastic and viscoelastic models have been used extensively in AFM studies for determining chondrocyte mechanical properties (Chahine et al. 2013; Darling et al. 2006; Darling et al. 2008; Ng et al. 2007). Finite element (FE) modeling, however, takes into account challenging aspects of the AFM nanoindentation problems such as, tip geometry, cell thickness and more complex cell mechanical properties including nonlinearity, viscoelasticity and even multiphasic material composition. This thesis investigated the time-dependent viscoelastic responses of single chondrocytes using a combined approach of AFM experimental measurements and finite element analysis.

As previously mentioned, OA changes occur in both articular cartilage and underlying subchondral bone. At tissue level, the subchondral bone consists of subchondral bone plate, underlying trabecular bone and bone marrow space (Burr et al. 2004; Henrotin et al. 2009). The layer adjacent to the cartilage is the subchondral bone plate, similar in structure and composition to the cortical layer in long bones. This layer provides supporting structure for the cartilage and transmits loads from the cartilage to the trabecular bone beneath. The pathological OA changes in bone include progressive increase in the subchondral bone plate thickness, alterations in the architecture of the trabecular bone, formation of osteophytes at the joint margins, development of subchondral bone cysts and advancement of the tidemark associated with vascular invasion of the calcified cartilage (Burr and Schaffler 1997; Radin et al. 1970b). The use of animal models of OA allows researchers to study the earliest changes in both articular and subchondral bone, which is often difficult or even impossible in humans. Surgically induced OA models through anterior cruciate ligament transection (ACLT) have been developed in various animal species due to rapid disease progression, which

resembles secondary OA after trauma. Although cartilage structural and compositional changes have been previously studied in a rabbit model of early OA, it is still not known whether these changes in cartilage occur concurrently with structural changes in the underlying bone.

High-resolution micro-computed tomography (micro-CT) is a powerful and reliable technique to assess the three-dimensional microstructure of the subchondral bone in animal models. In this thesis, micro-CT imaging was used to determine changes in the subchondral bone plate thickness and trabecular bone microstructure in a rabbit ACLT model of OA. Additionally, depth-wise changes in the proteoglycan content, collagen orientation angle and collagen content as well as biomechanical properties of cartilage were quantified using digital densitometry, polarized light microscopy, Fourier transform infrared microspectroscopy and indentation testing, respectively.

This research combines the recent developments of nanoscale engineering with different microscale techniques in order to evaluate the structure-function relationships of articular cartilage and subchondral bone at cellular and tissue levels.

2. BACKGROUND ON CHARACTERIZATION OF ARTICULAR CARTILAGE, CHONDROCYTES AND BONE

This chapter concentrates on the knee joint which is a highly weight bearing joint. An understanding of normal structure-function relationships in tissues within the synovial joint, such as knee joint is essential for understanding the pathogenesis and consequences of joint disease, such as osteoarthritis.

2.1. Knee joint

The knee joint is one of the largest and perhaps the most complex synovial joints in the human body. Basically, it is described as a modified hinge-type joint which connects the proximal tibia, the distal femur and the patella and is lubricated by synovial fluid. It allows flexion and extension and a small amount of axial rotation when the knee is flexed. The knee joint is composed of two distinct articulations within a single joint capsule, namely the tibiofemoral and the patellofemoral joint (Figure 2.1).

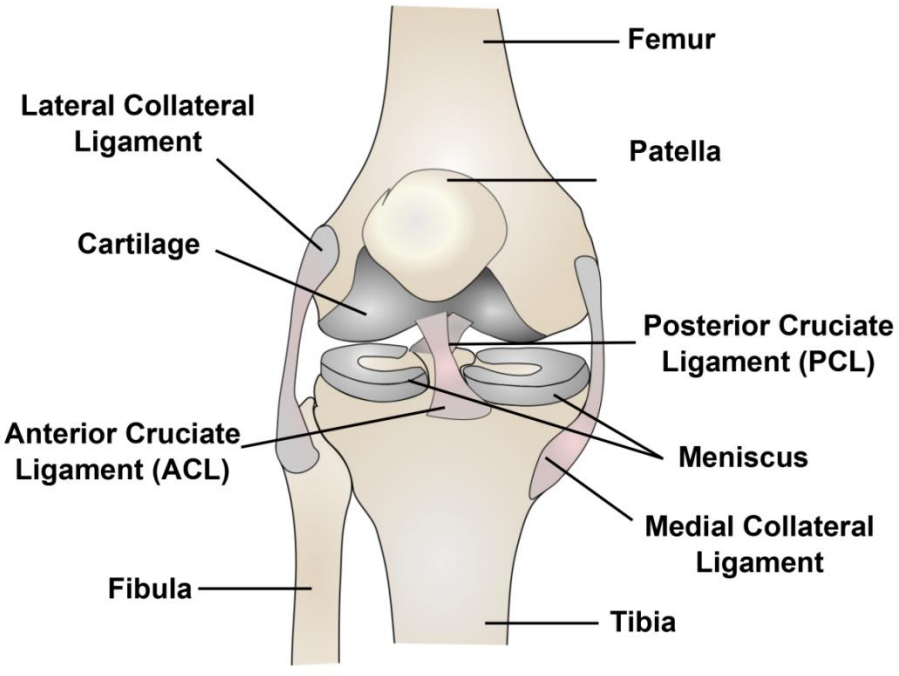

Figure 0.1 Schematic presentation of a knee joint anatomy.

The tibiofemoral joint connects the medial and lateral condyles of the femur with the corresponding tibial plateaus, whereas the patellofemoral joint is a gliding joint between the patella and the patellar surface of the femur. These three bones that form the knee joint are covered by articular cartilage and supported by several ligaments including the anterior and posterior cruciate ligaments (ACL, PCL) and the medial and lateral collateral ligaments (MCL and LCL). These ligaments together with the large muscles serve to stabilize and control the motion of the knee joint. Inside the joint, two fibrocartilaginous menisci provide cushioning and improve joint congruity. Knee joint includes a cavity between the bones, containing synovial fluid, which acts as a lubricant to decrease friction between the articulating surfaces.

There are several tissues with different material properties, including cartilage, subchondral bone plate and trabecular bone that act together as a functional unit to fulfill properly the functions of the knee joint, i.e. weight-bearing, articulation and dissipating the forces generated by locomotion. For this reason, the present thesis focuses on the simultaneous analysis of the three major tissues at different length scales, including articular cartilage and chondrocytes, subchondral bone plate and trabecular bone. However, the main focus of the thesis is the study of the biomechanics of single articular cartilage cells.

2.2. Articular cartilage

A description of structure and function relationships of articular cartilage is given. This section discusses the structure and the composition of articular cartilage, as well how it is organized at the micro- and nano- structural levels. The composition and structure of the tissue have a direct role in its function as a mechanical surface through regulation of its tensile, shear and compressive properties.

2.2.1. Composition and structure of articular cartilage

Articular cartilage is a highly specialized type of hyaline cartilage that lines the ends of long bones in synovial joints. In the knee joint, articular cartilage covers the ends of the femur, the top of the tibia and the back of the patella. Even though it is only a few millimeters thick, the major functions of articular cartilage are biomechanical in nature and include transmitting and distributing loads attenuating dynamic stresses in bone during joint loading and providing extremely low-friction surface for joint movement (Mow et al. 2005). Articular cartilage can withstand high levels of repeated loading at magnitudes several times body weight experienced in the joint throughout a person's lifetime with minimal tissue wear (Guilak et al. 1997). These functional characteristics rely on the multiphasic structural and compositional nature of articular cartilage that provide the tissue with exceptional tribological and mechanical properties.

2.2.1.1. Articular cartilage composition

In engineering terms, articular cartilage may be regarded as a fiber-reinforced hydrogel composite material. It contains highly specialized cells, called chondrocytes surrounded by a dense extracellular matrix (ECM), which is predominantly composed of a three-dimensional collagen network embedded in a gel-like matrix of proteoglycans (PGs) and water. Due to its fiber-reinforced nature

cartilage will exhibit different mechanical properties in tension and compression. According to the biphasic cartilage model, cartilage consists of two mechanically interacting phases: a solid phase saturated with a fluid phase.

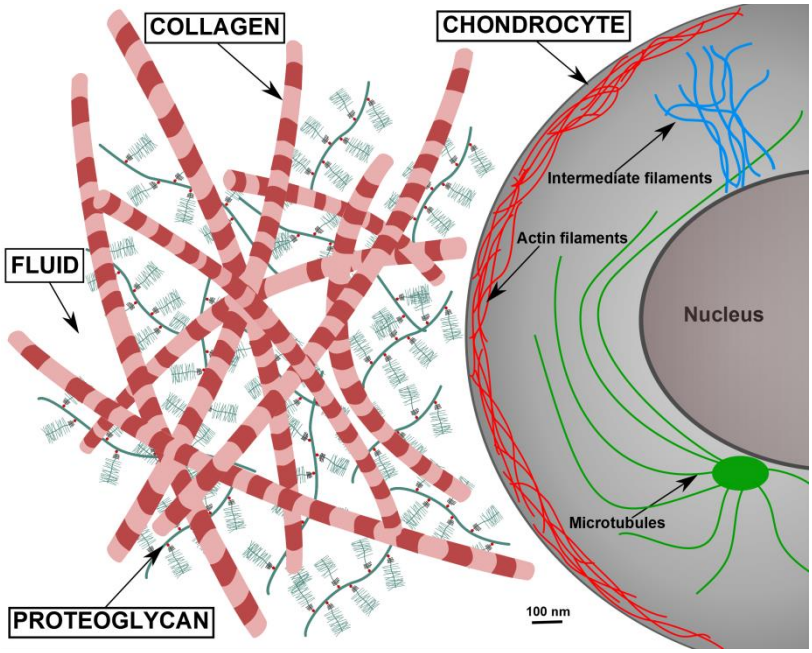

Figure 0.2 Extracellular matrix of articular cartilage.

The mixture of solid matrix and tissue fluid provides articular cartilage with its remarkable mechanical properties i.e. stiffness and resilience. The solid phase consists predominately of a framework of cross-linked collagens, mostly type II (10%-20% by wet weight), proteoglycans (PGs) (4-10% by wet weight) and non-collagenous proteins that give the tissue its form and stability (Buckwalter and Mankin 1998; Buckwalter et al. 2005; Lu and Mow 2008; Mow et al. 1999; Poole 1997). The fluid phase accounts for 65%-80% by wet weight of the cartilage and consists of water, nutrients and dissolved ions, such as sodium, calcium, chloride and potassium (Lai et al. 1991a, Maroudas et al. 1979). The flow of water through the cartilage and across the articular surface helps to transport and distribute nutrients for the articular cells, in addition to providing lubrication (Buckwalter et al. 2005).

Collagens are the major matrix proteins in the ECM. Four types of collagen participate in the formation of three-dimensional meshwork of the relatively thin and short matrix fibrils. Collagen type II is the most abundant collagen in ECM (90-95% of the total collagen content) (Alford and Cole 2005; Cremer et al. 1998), although other types are also present to lesser extent such as type V, VI, IX, X, XI, XII, XIV (Buckwalter and Mankin 1998). Collagen type IX facilitates fibril interaction with the matrix PG molecules. Collagen type XI regulates the fibril size whereas collagen type X organizes the collagen fibrils into a three-dimensional hexagonal lattice. In addition, type VI collagen is also found in the matrix, mainly at the

periphery of the chondrocytes where it helps to attach these cells to the matrix framework. Like all collagens, collagen type II consists of three repeating amino acid sequences that form a triple helix and is assembled in a staggered fashion into fibrils. Although very strong in tension, collagen fibrils have no resistance to compression due to their slenderness ratio (i.e. ratio between the length and the diameter) (Roth and Mow 1980). Collagen fibrils ranging from 30 nm to over 80 nm in diameter covalently cross-link to each other into a three-dimensional network in order to increase collagen rigidity (Eyre and Oguchi 1980; Han et al. 2011). Hence, the collagen network provides the shear and tensile properties to the cartilage. The orientation and alignment of collagen network vary throughout the cartilage depth e.g. depending on the species, anatomical site and the age of the subject (Saarakkala et al. 2010) and as well as across the joint. Benninghoff introduced the classical model for the architecture of the collagen network, consisting of arcades that are formed by fibers that run perpendicular to the subchondral bone in the deep zone, curve over in the transitional zone and run parallel to the articular surface in the superficial zone (Benninghoff 1925). This exquisite architectural layout of the collagen fibrils in cartilage is believed to be partly responsible for the anisotropic material properties of articular cartilage (Kempson et al. 1968; Mow and Ratcliffe 1997). Furthermore, collagen arrangement varies across the joint, as demonstrated by split-lines patterns shown when the cartilage surface is pricked with a pin (Bisson et al. 2005; Leo et al. 2004). Collagen type II provides a tensile force opposing the tendency of the PGs to cause swelling of the cartilage and also immobilize the PGs (Mow and Ratcliffe 1997).

In addition to collagen, *proteoglycan* (PG) is another structural component of the cartilage extracellular matrix (30% of the dry weight of the cartilage) (Buschmann and Grodzinsky 1995; Maroudas A 1979). Articular cartilage contains two major classes of PGs: large aggregating molecules or aggrecans and non-aggregating proteoglycans (decorin, byglican and fibromodulin). Aggrecans are so large that they are trapped within the three-dimensional collagen network and occupy most of the interfibrillar space of the cartilage matrix. They are characterized by a "bottle-brush" architecture and consists of glycosaminoglycan (GAG) chains, predominately chodroitin sulfate and keratin sulfate attached to a hyaluronic acid backbone by link proteins (Mow and Ratcliffe 1997).

All the components of the PG aggregates are synthesized by the articular chondrocytes. One distinct property of the PG aggrecans is the high fixed negative charge density which originates from numerous sulphate and carboxyl groups across GAG side chains. The high fixed negative charge in ECM is electrically neutralized by mobile cations and anions contained in the synovial fluid. The difference in ion concentration between the ECM and synovial fluid introduces a fluid pressure difference between them, the so-called Donnan osmotic pressure. In addition, the fixed negative charges are placed close together in the dense ECM creating a strong electrostatic repulsive force between the PGs and matrix expansion. These two mechanisms define the total swelling pressure in articular cartilage (Lai et al. 1991b). In the absence of any applied load the swelling tendency of the PGs is restrained by the collagen network. The amount of PGs increases progressively from superficial to the deep zone of articular cartilage.

Water is the main component of the articular cartilage, as well as in the synovial fluid that is present in the joint capsule. The water content is at its highest percentage at the articular surface (~80%) and decreasing with depth to about 65% in the deep zone (Buckwalter and Mankin 1998). This also includes intracellular water (in chondrocytes), although the majority of water in articular cartilage is in

the molecular pores of the ECM. Inorganic salts, sodium, calcium, potassium and chloride are dissolved in water (Mow and Ratcliffe 1997). There are two types of water that exist in the cartilage matrix, i.e. free water and bound water. The former is mobile and can slowly flow through the dense cartilage matrix upon application of a pressure gradient across the tissue or deformation of the solid matrix phase. This movement through the ECM generates high frictional resistance, thus resulting in low permeability. The later is mainly related to the hydrophilic characteristics of the PG molecules and the organization and mechanical strength of the collagen-PG network, thus a large amount of water is entrapped in the intramolecular and intermolecular space within the cartilage matrix (Maroudas 1975; Mow et al. 1984). Therefore, the amount and the spatial distribution of the water through the articular cartilage are mainly related to the PG and collagen concentrations and the orientation of collagen network (Maroudas et al. 1975). Water flow plays an important role in chondrocyte metabolism by transporting both nutrients and metabolic waste to and from the cells and thus, it has a function in maintaining the integrity of the articular cartilage (Maroudas et al. 1985).

2.2.1.2. Articular cartilage structure

Articular cartilage has two different structural characteristics when describing matrix organization. The first is with respect to depth within the tissue, while the second is with respect to distance from the chondrocyte membrane.

The structure of articular cartilage varies from the joint surface to the subchondral bone. Depending on the matrix structure and composition as well as cellular appearance (Meachim and Stockwell 1973), cartilage can be subdivided into four zones (Meachim and Stockwell 1973). These are termed the superficial, middle (or translational), deep and calcified cartilage zones (Figure 2.3). The superficial zone is rich in collagen fibers with a few elongated chondrocytes. PG content of the matrix increases progressively with the tissue depth, with an inverse proportion of matrix hydration. Each of these zones exhibit great variations in their mechanical characteristics.

The superficial zone is the uppermost and the thinnest zone (Mow et al. 1989). This zone is characterized by small-diameter collagen fibrils (25-50nm), which are tightly packed and oriented tangential to the cartilage surface (Hwang et al. 1992; Muir et al. 1970). Similarly, a relatively small number of elongated chondrocytes in the superficial zone are oriented parallel to the surface and to the direction of shear stress. This particular orientation of collagen type II and chondrocytes in the superficial zone provides a great deal of strength and stiffness to the articular cartilage, which is crucial for resisting shear and tensile forces from the articulating surfaces in normal motion. Additionally, the chondrocytes in the superficial zone produce a specialized molecule, called lubricin, which coats cartilage surfaces and lowers surface friction. Hydration is high in this zone, while the PG content is lower compared to other zones. In fact, this zone has the lowest compressive modulus most likely due to the low PG content and thus it is subjected to a large compressive strain during joint articulation.

The middle zone lies in between the superficial and deep zone (Mow et al. 1989). This is more commonly referred to as the transitional zone due to the change in direction of the collagen fibrils from a direction parallel to the surface to a vertical orientation toward the underlying subchondral bone (Benninghoff 1925). In this zone slightly larger fibrils are packed loosely and aligned obliquely to the surface (Hwang et al. 1992). As the fibers extend deeper, they become thicker and

fewer in number (Buckwalter et al. 2005). Unlike the superficial zone, the chondrocytes in the middle zone exhibit a lower cell density, however larger and more spherical in shape, and start to appear in chains aligned vertically with the collagen fibrils. There is less hydration and higher content of PGs providing the tissue with greater compressive strength compared to the superficial zone.

In the deep zone, large-diameter collagen fibrils (up to 160 nm) are oriented perpendicular to the underlying subchondral bone (Clark 1991; Minns and Steven 1977). This zone is characterized by column-like chondrocytes also oriented perpendicular to the articulating surfaces. This zone exhibits lowest hydration and highest PG content, translating into the highest compressive modulus of any zone.

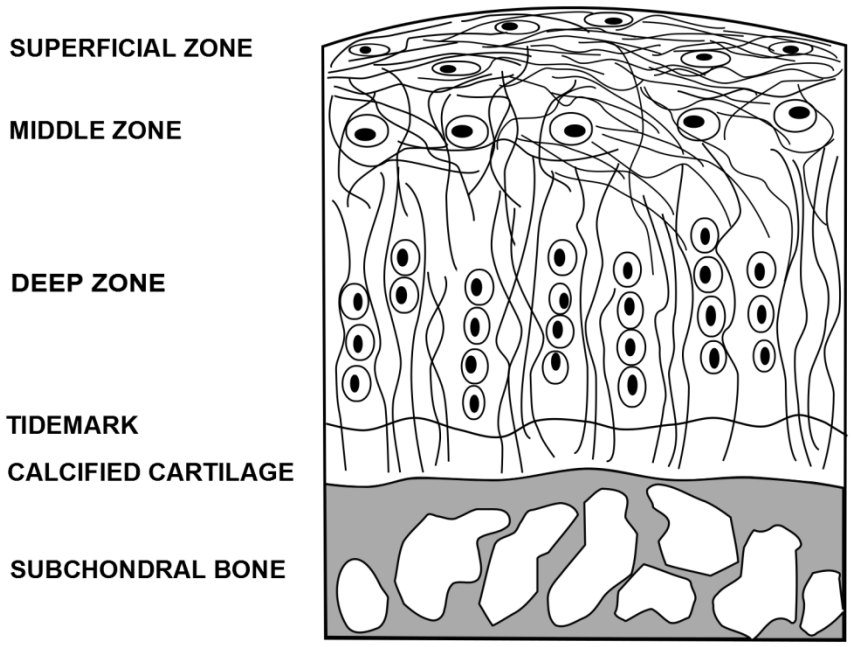

Figure 0.3 Schematic representation of various zones of articular cartilage.

Immediately beneath this zone is the deepest zone, a thin zone of calcified cartilage that contains a relatively small number of radially oriented fibers which help to securely anchor the cartilage to the underlying bone (Bullough and Jagannath 1983). This zone contains few inert chondrocytes embedded in a calcified ECM. The tidemark or basophilic line which is partially mineralized represents the border between the deep zone and calcified cartilage, thought to prevent collagen fatigue (Minns and Steven 1977). Unlike the growth plate, this region resists vascular invasion restricting nutritional flow into the cartilage from this surface. Finally, the subchondral bone, which is much like cortical bone in structure, separates the articular cartilage from the underlying trabecular bone.

In addition to the four distinct zones, the ECM can also be classified into three regions known as pericellular, territorial and interterritorial matrices based on the proximity to the chondrocytes, composition and collagen fiber diameter and organization.

The pericellular matrix (PCM) surrounds the chondrocytes and together forms the "chondron" (Poole 1997). The smallest matrix region, the pericellular matrix consists of a narrow rim of a filamentous matrix network containing high levels of PGs, thinner collagens such as type VI collagen and glycoproteins, but contains less type II collagen fibers found in the interterritorial matrix. Most unique to this region is type VI collagen, which presumably plays some role in cell anchoring and cell-matrix interaction and signaling together with other molecules present in the pericellular cartilage matrix (Figure 2.4). The PCM is also mechanically distinct from the ECM by its lower Young's modulus (Alexopoulos et al. 2003; Alexopoulos et al. 2005). In consequence, the PCM is thought to possess the capacity to transduce the mechanical stimuli of the ECM during joint loading into electrochemical signals and to modulate the biochemical environment of the cells (Guilak et al. 2006).

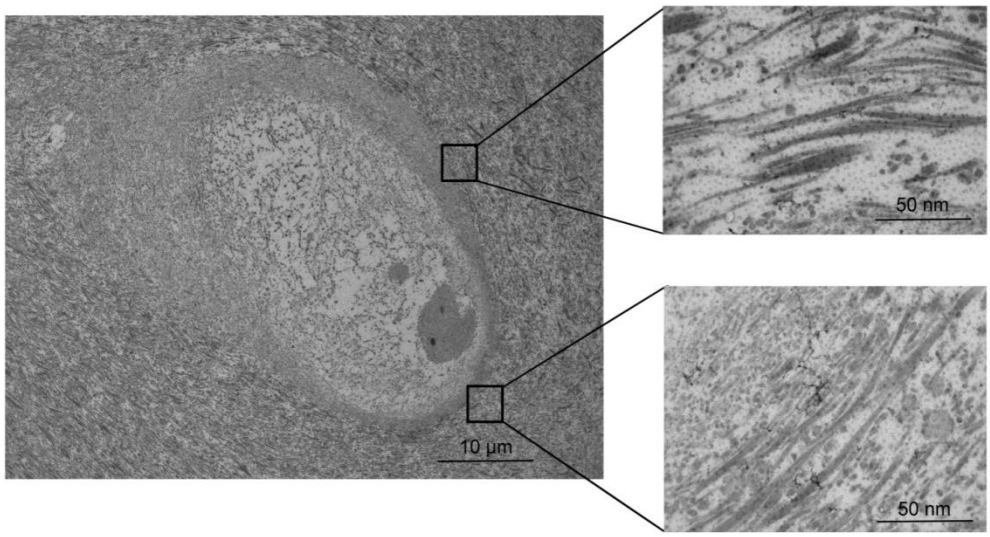

Figure 0.4 The chondrocyte surrounded by its pericellular matrix. Collagen type VI fibril meshwork can be seen (transmission electron microscopy).

The territorial matrix immediately adjacent to the pericellular matrix contains primarily collagen, forming a basket-like meshwork around the cells. This region is thicker than the pericellular matrix and densely organized and provides mechanical protection for the chondrocytes during loading and deformation of the tissue. An abrupt increase in the diameter of the collagen fibers and a transition from the basket-like orientation of the fibers to a more parallel arrangement marks the boundary between the territorial and interterritorial regions.

The largest of the three matrix regions, the interterritorial matrix, contains large type II cross linked collagen fibers as well as varying concentrations of PGs, dependent on depth from the cartilage surface. This extracellular matrix composition provides the cartilage with its functional characteristic to absorb mechanical load.

2.2.2. Biomechanical properties of articular cartilage

Articular cartilage is subjected to a wide range of static and dynamic loads during normal joint movement, such as low-level constant loading during weight bearing, intermittent loading during locomotion and high-impact loading during training and performance. The static compressive stress applied to human knee joints during standing can be ~2-4 MPa (Herberhold et al. 1999), while the dynamic compressive stress in the knee and hip during high stress activities can be 10-20 MPa or even more (Grodzinsky et al. 2000). Thus, articular cartilage endures a high biomechanical demand, in both compression and shear. The mechanical functions of articular cartilage and its ability to withstand loading without damage over several decades of constant use depend heavily on the structural integrity of its extracellular matrix components. In general, the collagen network (predominantly composed of type II collagen) imparts the tensile strength and the negatively charged PGs resist compression (Stockwell et al. 1991).

Articular cartilage is also a highly complex material, fluid-saturated, fiber-reinforced, porous, permeable composite matrix (Mow et al. 1984). The material properties of cartilage can be described as viscoelastic (time or rate dependent), anisotropic (dependent on orientation) and non-linear (dependent on the magnitude of strain) (Guilak et al. 2000). Biomechanical and low friction properties of articular cartilage arise from the biphasic nature of the tissue, in which a solid phase (collagen-PG matrix) and a fluid phase (water and ions) have a unique interplay with one another.

The biphasic nature of cartilage allows the tissue to behave as compressible material, while having incompressible components. The solid phase is composed primarily of a network of collagen fibrils maintained in a specific spatial arrangement by PG aggregates. Cartilage has low permeability due to a high frictional resistance of solid to fluid flow. This causes a high interstitial fluid pressurization in the tissue. The low permeability and the resultant high fluid pressurization contribute both to the viscoelastic properties and stiffness of cartilage.

Cartilage viscoelasticity is defined as the time-dependent response of the tissue subjected to a constant load or deformation. This behavior is exhibited as stress relaxation and creep (Figure 2.5).

When cartilage is deformed and held at a constant strain, it responds with high initial stress which progressively diminishes with time until equilibrium is reached. The time-dependent stress response is known as stress-relaxation. Creep occurs when a material undergoes constant force. Similarly, articular cartilage responds by initially deforming rapidly and then deforming slowly over time. This time-dependent deformation continues until equilibrium is reached. Articular cartilage has been shown to exhibit both stress-relaxation and creep behaviors which are due to fluid-flow dependent and fluid-flow independent mechanisms.

Flow-dependent viscoelasticity originates from fluid flow through the cartilage solid matrix and contributes strongly on articular cartilage response under compressive forces. With an applied external load there is deformation of the matrix macromolecules, which causes a pressure gradient in the tissue and results in the flow of interstitial fluid through the pores within the ECM. This fluid flow is resisted by the low permeability of the cartilage matrix, thus generating a significant frictional resistance within the tissue. Moreover, the interaction between the negatively charged GAGs and the water molecules further limits fluid flow through the ECM pores. This interaction combined with the hydraulic pressure gradient withstands as much as 95% of the mechanical impact or dynamic load applied to

the cartilage; the remaining 5% is achieved by ECM deformation. Over time, the load applied is transferred from the fluid phase (hydrostatic pressure) to the solid phase (collagen-PG matrix). At the equilibrium, fluid flow or fluid pressure gradients vanishes and the entire load is completely supported by the compressed collagen-PG solid matrix (Mow et al. 1980; Wilson et al. 2005). Upon removal of load or deformation, cartilage recovers its initial dimensions, due to the elasticity of the solid phase and the fluid flow back into the tissue.

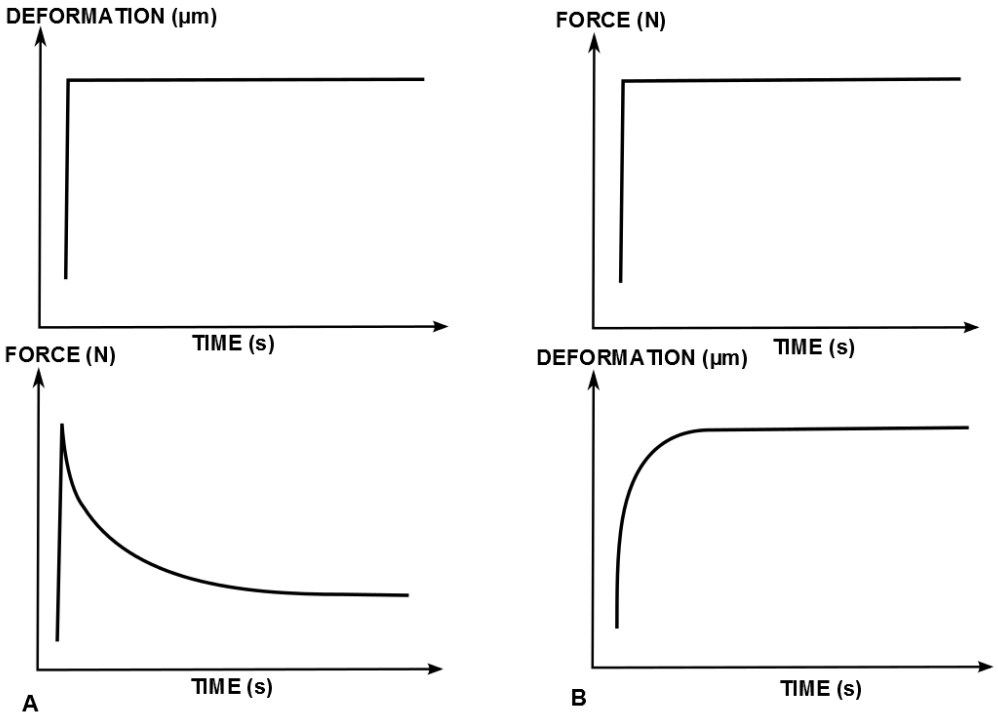

Figure 0.5 (A) Stress-relaxation (B) Creep.

Fluid flow in a loaded cartilage is governed by the permeability (k'). Permeability is a measure of the ability of fluid to flow through a porous-permeable material such as ECM and is inversely proportional to the frictional drag exerted by the fluid. The permeability is also highly dependent on the pore size of the ECM. When the tissue is deformed pore sizes change, making the permeability strain-dependent.

Flow-independent viscoelasticity of cartilage has been suggested to originate from the intrinsic viscoelastic properties of the macromolecular network. Under this condition, no fluid flow or tissue volume change occurs and viscoelasticity is due to the properties of the tissue microstructure.

The time-dependent compressive properties of cartilage are primarily the result of the flow-dependent viscoelastic mechanisms (Mow et al. 1980; Mow and Ateshian 1997). The compressive modulus, a measure of intrinsic compressive stiffness, is low in the superficial layer and increase with depth from the articular surface (Mow et al. 2001). The PGs play a major role in providing cartilage with a weight-bearing capability under compression at a quasi-static loading rate. Two

mechanisms (Donnan osmotic pressure and electrostatic repulsive forces) are involved in the ability of PGs to provide articular cartilage with weight-bearing capabilities as previously described.

The time-dependent tensile properties of cartilage are the result of both flow-dependent and flow-independent (mainly collagen viscoelasticity) viscoelastic mechanisms. When articular cartilage is stretched or loaded in tension the collagen fibers and PG molecules stretch along the axis of loading. The stress/strain curve follows a sigmoid curve. With minor deformation of the cartilage there is a nonlinear increase in stress as the matrix molecules disentangle and realign. With greater deformation, the fibers stretch and generate a greater linear increase in tensile stress (following Young's modulus). The tensile stiffness decreases with depth and as the axis of extension deviates from the split-line direction. The tensile modulus has been shown to be dependent on the concentration of the collagen fibrils and cross-links, the type of collagen cross-links and the strength of the ionic bonds and interactions between the collagen-PG matrix (Bae et al. 2008; Broom 1984). In fact, the tensile modulus is the highest at the surface and decreases with depth, due to the high concentration and high degree of orientation of collagen fibrils in the superficial zone (Bae et al. 2008).

2.3. Chondrocytes

In this section a description of structure and function on articular chondrocytes is given, followed by a review of the experimental techniques and mechanical models used for quantifying the biomechanical characteristics of cells.

2.3.1. Chondrocyte structure and function

Articular cartilage possesses only one cell type, chondrocytes, which are embedded within the extracellular matrix. Whilst chondrocytes exist at low densities in the tissue (varying between 1-10% of the total tissue volume in articular cartilage) they are extremely active cells and are capable of responding to a range of mechanical and biochemical stimuli (Ratcliffe and Mow 1991). Mechanical properties of the chondrocytes itself barely contributes to the overall mechanical properties of articular cartilage, however these cells are responsible for maintaining and repair of the cartilage ECM through the synthesis and secretion of PGs, collagens, non-collagenous proteins and as well as of various enzymes.

Chodrocytes are essential in regulating the composition and organization of the structures contained in the ECM that determine the tissue's elasticity and strength through the cellular response to stress. These cells produce enzymes not only for matrix synthesis but also for its degradation. This is important during the slow metabolic turnover that occurs in the articular cartilage during the daily motion of the joints in order to remove and restore articular cartilage from minor damage and wear. Because articular cartilage is not vascularized, delivery of nutrients to chondrocytes and removal of metabolic waste products from the cartilage are believed to occur through synovial fluid and as well through subchondral bone.

Typical chondrocytes embedded in cartilage matrix exhibit rounded or polygonal morphology, except at specific zones, where they may be flattened or discoid (Figure 2.3). Chondrocyte size varies considerably, with the diameter ranging from 10 to 15 μm. The morphology, density and synthetic activity of a

chondrocyte vary depending on its position within different zones of articular cartilage, age and pathological state (Poole 1997).

Chondrocytes are composed of approximately 60% water, yet also exhibit significant degrees of structural order and mechanical integrity (Oswald et al. 2008). Although a lot of research has been done in the field of cell biology focusing on structural and biochemical aspects of the chondrocytes, there is little information about the mechanical properties of chondrocytes and how they sense and respond to mechanical stimuli both structurally and biochemically. Like many other cell types, the chondrocytes are very complex organized systems. The mechanical properties of the chondrocytes are determined in part by the properties of the cell membrane, in part by the properties of the cytoplasm and in part by the structure of the cytoskeleton. Furthermore, as a large percentage of the chondrocyte is fluid, compressive loads can also be supported by hydrostatic pressures.

Chondrocytes are separated from the external environment by a thin lipid bilayer semi permeable membrane consisting of a rich mix of phospholipids, glycolipids, cholesterol, and a vast array of transmembrane proteins. Cell membrane resists the internal fluid pressure built inside the cell. The membrane enables the chondrocyte to interact chemically (through receptors) and mechanically (through integrins) with the extracellular matrix. The internal cell homeostatis is maintained by exchanging various ions and water molecules through the pores and channels located on the cell membrane. Beside its role as a selectively permeable barrier encapsulating the cytoplasm, the cell membrane is also involved in cell adhesion, cell signaling, anchoring the cytoskeleton, attaching the extracellular matrix, maintaining cell volume and the electric membrane potential (Janmey et al. 2007; Wilkins et al. 2000; Wright et al. 1996). Due to the close binding of the cell membrane with the actin cortex and other attached molecules, it is difficult to isolate the purely elastic behavior of the cell membrane. It has been shown that cell membranes form long tethers of several microns that oppose a force to pulling independent of extension (Benoit et al. 2000; Hochmuth 2000). The cytoplasm contains cytosol which is a water solution of enzymes, organic molecules, cellular organelles and the nucleus. The mechanical behavior of the nucleus has been shown to contribute to chondrocyte mechanical properties also, with studies (Guilak et al. 2000) reporting that it can be between 3-4 times stiffer than the surrounding cytoplasm and almost twice as viscous.

The cytoskeleton is the cellular "skeleton" contained within the cytoplasm which controls the shape and the mechanics of cells. Chondrocytes respond to high compressive loads by changing the cytoskeleton architecture that realigns its major compressive component in the direction of compression loading (Durrant et al. 1999). On the other hand, when deregulated, alterations in the cytoskeleton organization of chondrocytes may predispose the tissue to pathological conditions, such as osteoarthritis (Trickey et al. 2004).

Moreover, the cytoskeleton network exhibits highly nonlinear behavior at medium strain levels. That includes a dramatic increase in rigidity as the networks are increasingly deformed, a property termed "strain-stiffening" (Storm et al. 2005). At large strain levels, cytoskeleton network can also show "strain softening" (Lee et al. 2010; Lieleg et al. 2009). The structure of the chondrocyte cytoskeleton varies with cartilage depth and between weight-bearing and non-weight-bearing regions of the joint (Durrant et al. 1999; Lieleg et al. 2009).

The cytoskeleton is composed of three main types of filamentous structures: actin filaments, tubulin microtubules and vimentin intermediate filaments (Benjamin et al. 1994). Each of the three types of cytoskeletal filaments is a polymer built

from protein subunits, held together by weak non-covalent bonds. These polymers together with a large variety of additional proteins which act as cross-linking agents form a highly organized composite network, extending throughout the cytoplasm from the cell nucleus to the cell membrane and attaching to the membrane and organelles. These filamentous structures differ from each other in their structure and function and they have distinct mechanical roles in the cells. With the exception of intermediate filaments, actin filaments and microtubules are highly "dynamic" in nature as these structures constantly undergo assembly and disassembly in response to intracellular and extracellular cues, a phenomenon referred to as polymerization and depolymerization.

The actin filaments (F-actins) or microfilaments, the thinnest in the cytoskeleton at only 7 nm in diameter seems to be of particular importance for the mechanical properties of the cell (Blain 2009). A single actin filament has a Young's modulus (E) of ~2 GPa (Kojima et al. 1994). It is noteworthy that single actin filaments are ~ 10^6 times stiffer than typical animal cells E ~0.1-1 kPa (Kuznetsova et al. 2007). Their relatively short persistence length (~18 μm) reflects their capability to support tension stresses. The cable-like actin filaments are long and flexible helical polymers (F-actin) formed by polymerization of the monomeric globular form of the protein (G-actin). The actin filaments can grow and break down at their two ends by polymerization and depolymerization. The fast-polymerizing end is called the barbed end (plus end), while the slow-polymerizing end the pointed end (minus end). The polymerization and depolymerization of the actin cytoskeleton is regulated by a large number of actin-binding proteins. This "dynamic" morphological change enables the actin filament network to remodel itself in response to mechanical stimuli.

The actin filaments cross-linked into a three-dimensional network can be found either underneath the cell membrane as so-called actin cortex or at the periphery of the chondrocyte as rigid bundles cross-linked with the molecular motor myosin called stress fibers (Blain 2009; Langelier et al. 2000; Trickey et al. 2004). Stress fibers presumably reinforce the cortical layer and are also important for the transport of organelles and cellular locomotion. Moreover, the actin fibers can be coupled directly to extracellular matrix proteins at specialized sites termed focal adhesions. These structures include transmembrane proteins called integrins and are thought to be involved in chondrocyte mechanotransduction as they connect the ECM to the cytoskeleton and other intracellular signaling molecules (Shakibaei et al. 2008). This connection might allow chondrocytes to detect and respond to both chemical and mechanical signals from the extracellular matrix.

The tubulin microtubules are hollow tubes with outer diameter on the order of 25 nm and are thought to be much stiffer than both actin and intermediate filaments, due to their cylindrical structure (Fletcher et al. 2000). Tubulin is a highly "dynamic" polymer formed from the globular proteins α and β-tubulin dimers. Although they are the stiffest of all filamentous structures, the microtubule network appears not to dominate the mechanics of the chondrocyte cytoskeleton during micropippete aspiration (Trickey et al. 2004).

Vimentin intermediate filaments form rope-like structures that are flexible, but difficult to break (Fletcher et al. 2000). Intermediate in size between the microfilaments and microtubules (diameter between 10-12 nm), intermediate filaments are highly organized polymers, which appear to connect the cell periphery with the nucleus. There is some evidence that vimentin intermediate filaments are more abundant in chondrocytes than in other cells. In addition, vimentin expression is increased in chondrocytes of weight-bearing regions of cartilage (Eggli et al.

1988) and in regions that undergo greater levels of cellular deformation (Langelier et al. 2000). Therefore, recent studies (Chahine et al. 2013; Trickey et al. 2004) investigating the contribution of the vimentin filaments to the mechanical properties of chondrocytes suggests that, in conjunction with the actin filaments, these structures also contribute to some extent to the mechanical integrity to the cell.

Although all three cytoskeletal biopolymers are important for mechanical function of the chondrocytes, experimental studies in which these elements were disrupted have shown that the actin filaments and intermediate filaments have a major contribution to the overall cell mechanical response (Chahine et al. 2013; Durrant et al. 1999; Trickey et al. 2004). Specifically, actin filaments emerged as the greatest contributor to compressive stiffness as actin disruption decreased the chondrocyte stiffness by nearly 90% and viscosity by 80% (Trickey et al. 2004).

The biomechanics of intermediate filaments are not as well understood as those of actin microfilaments and microtubules. Is it thought that the contribution of microtubules to the mechanical properties of the chondrocytes is minor compared to the other two cytoskeletal components.

2.3.2. Biomechanical behavior of articular chondrocytes

Under physiological conditions, chondrocytes are exposed to changes in mechanical and physico-chemical environment of the ECM, including compression, shear stress, hydrostatic pressure, osmotic stress, and tensile stretch. The ability of the chondrocytes to detect and respond appropriately to these mechanical signals (i.e. mechanotransduction) is critical in maintaining structural integrity of cartilage arising from the mechanical interactions between cells and the surrounding cartilage matrix. This is also valid on the opposite direction as well: mechanical stimulation exerted on cartilage is transmitted to chondrocytes and can influence many physiological functions (Guilak 1995).

Due to the complex nature of chondrocytes, characterization of their mechanical properties is very challenging. While studies of cartilage mechanobiology can quantify stress and strain at the bulk cartilage level, relatively few studies have attempted to quantify the local mechanical properties of the chondrocytes.

To understand the mechanical characteristics of single chondrocytes and how these properties change in response to stress, various mechanical testing systems for single cells have been developed. These systems rely on the use of different methods to apply mechanical forces to characterize cellular biomechanics and require theoretical models to calculate these material properties.

2.3.2.1. Mechanical testing of single chondrocytes

Testing mechanical properties of materials such as metal, ceramics or polymers is a straightforward and well established procedure. Chondrocytes on the other hand as previously mentioned are highly "dynamic" so that their cytoskeletal structures are constantly changing in response to various external stimuli. Therefore, one must keep in mind when measuring mechanical properties of chondrocytes that they are not traditional engineering materials.

Over the past several decades, various techniques have been employed to quantify the mechanical properties of cells. However, the focus of this thesis will be restricted to the techniques used to determine the unique mechanical characteristics of single chondrocytes. Because the articular chondrocytes are typically around 10-15 μm, mechanical testing devices must be especially sensitive to small changes in

force and displacement. To test the tensile properties of chondrocytes, micropipette aspiration is the most common method and relies on pressure differentials to deform the cell. For compressive and shear testing, this is often achieved by the use of a cantilever to probe the cell and some mechanism to detect the position of the cantilever over time. Typically, single chondrocytes are mechanically tested using one of the following four techniques:

- micropipette aspiration (Haider and Guilak 2000; Jones et al. 1999; Trickey et al. 2000; Trickey et al. 2006)
- unconfined compression (Leipzig and Athanasiou 2005; Ofek et al. 2009a; Shieh and Athanasiou 2006)
- cytoindentation (Koay et al. 2003; Shin and Athanasiou 1999)
- atomic force microscopy (AFM) (Chahine et al. 2013; Darling et al. 2006; Darling et al. 2008; Ng et al. 2007)

Both adherent (i.e. spread) cells and cells in suspension can be tested using the above mentioned techniques.

In the following section the above-mentioned techniques are presented in more detail and a summary of the values for elastic properties of single chondrocytes are presented (Table 2.1).

Micropipette aspiration

One of the earlier methods to measure the mechanical characteristics of individual cells is through micropipette aspiration (Hochmuth 2000; Sato et al. 1990; Theret et al. 1988). In this technique, a small pipette applies a negative suction pressure on the surface of the cell, thereby deforming its membrane into the micropipette. By recording this deformation-induced change using video microscopy, the mechanical properties of the cell can be determined. This deformation-induced change is highly dependent on the required suction pressure levels and on the geometric relations pertaining to the shape of the pipette. This technique can be used to quantify the mechanical adhesiveness of a cell attached to a particular substrate.

Micropipette aspiration has frequently been used to determine the mechanical properties of chondrocytes harvested from both normal and osteoarthritic articular cartilage. Jones et al. (1999) first used this approach to compare cellular mechanical characteristics, such as Young's modulus and volumetric properties, from both healthy and diseased tissue. They applied maximum pressures between 0.05 and 1 kPa through a micropipette with an inner diameter of approximately 5 μm. By modeling the cell as homogeneous elastic half-space (Equation (2.6)), they determined that no differences existed between the Young's modulus of normal and osteoarthritic chondrocytes (0.65 kPa versus 0.67 kPa). However, significant differences were observed in cell volume changes immediately and 600 seconds after complete aspiration of the cells into the micropipette. Normal chondrocytes only exhibited an 11% volume change, while osteoarthritic cells lost 20% of their volume. A similar study by Trickey et al. (2000) applied the standard linear solid model to micropipette experiments on normal and osteoarthritic chondrocytes. Their results showed that cells from diseased cartilage tissue were stiffer and more viscous than healthy cells, with regards to instantaneous modulus (0.63 kPa versus 0.41 kPa), relaxation modulus (0.33 kPa versus 0.24 kPa) and apparent viscosity (5.8 kPas versus 3.0 kPas).

Recently, Trickey et al. (2006) combined experimental tests with a finite element analysis of the cell either as biphasic or viscoelastic material to compare the recovery behavior of normal and osteoarthritic chondrocytes. While there were

no significant differences between the Poisson's ratio of normal and osteoarthritic cells (0.38 versus 0.36), osteoarthritic chondrocytes did exhibit a greater characteristic recovery time upon release of the suction pressure. While many cells are assumed to be incompressible with a Poisson's ratio of 0.5, these studies (Bidhendi and Korhonen 2012; Trickey et al. 2006), demonstrated that the chondrocytes exhibit a certain level of compressibility possibly due to the intracellular fluid outflow rather than to the true compressibility of the cellular components and cytoplasm.

Along with many advantages to this method, there are some important considerations that must be made when analyzing its resulting data. Due to the nature of the experiment, measures of viscosity and stiffness are influenced by the mechanical properties of the cell membrane, and thus may not reflect the bulk properties of the cell. Given the microenvironment of the chondrocyte and that its deformation occurs mostly in compression, testing a portion of the cell in tension will provide to some extent an indication of cell mechanical properties.

Unconfined compression

This testing modality has been extensively utilized to study both the material properties and mechanical behavior of chondrocytes (Leipzig and Athanasiou 2005). In order to adapt the mechanical models to extract the mechanical properties with this experimental technique, a suitable geometry for the chondrocyte was identified to accurately depict the anchorage-dependent properties and structure of the cell. Leipzig et al. (2005) developed unconfined creep compression solutions for elastic, standard linear solid and linear biphasic mechanical models. Using the cytoindenter device, the original 5 μm diameter indenter was replaced with a wider 50.8 μm diameter tungsten probe to apply constant loads of 75 nN for 45 seconds on the chondrocyte. It was observed that viscoelastic model best fit the creep behavior of the individual cell, most notably in the early response phase to the applied force.

Leipzig et al. (2005) also determined the elastic modulus for chondrocyte to be 2.55 kPa. Curve fitting the data to the viscoelastic model resulted in an instantaneous modulus of 2.47 kPa, relaxation modulus of 1.48 kPa, and apparent viscosity of 1.92 kPas. Finally the biphasic fit yielded an aggregate modulus of 2.58 kPa and Poisson's ratio of 0.069. Similar to later findings (Darling et al. 2006) in AFM nanoindentation, it was determined that superficial zone cells were significantly stiffer than those from the middle/deep region in terms of instantaneous modulus (1.59 kPa versus 0.69 kPa), relaxation modulus (1.20 kPa versus 0.49 kPa), and apparent viscosity (6.32 kPas versus 0.18 kPas).

Cytoindentation

One increasingly popular technique to study the mechanical properties of single cells is cytoindentation. This recently developed procedure investigates a cell's ability to withstand controlled indentations by a flat-ended miniature borosilicate glass probe of 5μm in diameter, which is attached to a much larger cantilever beam. Cytoindentation utilizes similar cantilever principles as atomic force microscopy (AFM) to determine the applied force based upon the deflection of the beam.

The cytoindentation device possesses several advantages that allow it to characterize the mechanical behavior of individual chondrocytes. Most importantly, it is capable of performing creep indentation on single cells, a test that is able to elucidate the viscoelastic properties of single cells. Due to the simplicity of sample

preparation in this setup, any type of anchorage dependent cell type may be tested. The system may also be adapted to use different shaped probes to apply different types of load to the cell.

Recently, Koay et al. (2003) modified the cytoindenter setup to enable a laser micrometer to record the displacement at the end of the cantilever. Using a closed loop algorithm, the authors applied creep tests on single chondrocytes at a test load of 50 nN for either 15 or 20 seconds. Both punch and viscoelastic continuum models were used to determine the mechanical properties of the chondrocytes. The punch model (Equation (2.5)) yielded an average Young's modulus of 1.10 kPa. The viscoelastic model resulted in an instantaneous modulus of 8 kPa, relaxation modulus of 1.01 kPa and apparent viscosity of 1.5 kPas for the chondrocyte.

Atomic force microscopy

Darling et al. (2006) examined the viscoelastic nature of porcine articular chondrocytes from both superficial and middle/deep zones using AFM. The authors derived a viscoelastic solution for the punch problem with a spherical indenter (Equation (2.4)). Applying a ramp velocity of 6.25μm/s to reach a target force of 2.5 nN, held for 60 seconds at the center of the cell, the stress-relaxation experiments yielded relevant mechanical properties. It was found that superficial zone chondrocytes were stiffer than middle/deep cells in terms of instantaneous modulus (0.55 kPa versus 0.29 kPa) and relaxation modulus (0.31 kPa versus 0.09 kPa) and had a greater apparent viscosity (1.15 kPas versus 0.61 kPas).

Ng et al. (2007) recently utilized AFM to investigate chondrocyte elastic properties with its developing PCM. Individual chondrocytes, with and without their associated matrix, were placed in custom-made pyramidal wells in preparation for testing. This provides the significant advantage of testing individual cells or chondrons without requiring them to be adherent on a substrate. Accurate spatial maps were obtained and finite element and Hertzian modeling was used to obtain biomechanical properties. In addition, a hysteresis upon unloading the probe was also observed, confirming previous findings regarding the time-dependent behavior of chondrocyte cells. Another AFM study (Bader et al. 2002) examined the nonlinear force–displacement response of single chondrocytes at various positions on the cell surface. Their results showed that the center of the cell was most resistant to an applied indentation.

The development of a mathematical model to describe single cell testing with the AFM can be a challenging task. Assumptions about the cell's geometry, homogeneity and compressibility must be made in order to solve the constitutive equations involved. Because the cell contains organelles and cytoskeleton, and may have different shapes when attached to a surface, these assumptions may introduce uncertainties in calculating the mechanical properties. Therefore, careful consideration must be made to ensure the applicability of various models to single cell AFM nanoindentation data.

A summary of published values for single chondrocyte mechanical properties is shown in Table 2.1.

Table 0.1 Summary of published values for single chondrocytes elastic properties using various mechanical testing techniques

Mechanical testing technique	Mechanical properties	Model	Cell type
Micropippette aspiration			
Jones et al. (1999)	E=0.65 kPa	Elastic half space	Human chondrocytes
Trickey et al. (2000)	E_0=0.41 kPA E_∞=0.24 kPa	Viscoelastic half space	Human chondrocytes
Trickey et al. (2000)	E_0=0.63 kPA E_∞=0.33 kPa	Viscoelastic half space	OA human chondrocytes
Bader et al. (2002)	E=0.81 kPa	Elastic half space	Adult bovine chondrocytes
Darling et al. (2006)	E_0=2.47 kPa E_∞=1.48 kPa	Viscoelastic model	Adult porcine chondrocytes
Unconfined compression (cytocompression)			
Leipzig et al. (2005)	E=2.55 kPa E_0=2.47 kPa E_∞=1.48 kPa	Elastic model Viscoelastic model	Adult bovine chondrocytes
Shieh et al. (2006)	E_0=1.06 kPa E_∞=0.78 kPa	Viscoelastic half space	Adult bovine chondrocytes
Cytoindentation			
Koay et al. (2003)	E=1.10 kPa E_0=8.00 kPa E_∞=1.09 kPa	Elastic half space Viscoelastic half space	Adult bovine chondrocytes
Atomic force microscopy			
Bader et al. (2002)	k=0.02 N/m	No model used	Adult bovine chondrocytes
Darling et al. (2006)	E=0.6-1.27 kPa E_0=0.29-0.55 kPa E_∞=0.17-0.31 kPa	Elastic model Modified viscoelastic model	Adult porcine chondrocytes (superficial and deep zone cells)
Ng et al. (2007)	E=1 kPa	Elastic model	Young bovine chondrocytes
Chahine et al. (2013)	E=0.75-2.32 kPa E_0=0.70-0.90 kPa E_∞=0.63-0.87 kPa	Elastic half space Viscoelastic model	1 day, 5 and 19 year old bovine chondrocytes,

E Young's modulus; E_0 instantaneous modulus; E_∞ relaxation (equilibrium) modulus; OA-osteoarthritic

2.3.2.2. Chondrocyte theoretical models

Three models, of increasing complexity, have been used in recent literature to determine mechanical properties of individual chondrocytes: elastic half-space model, viscoelastic model (fluid-flow independent) and biphasic model (fluid-flow dependent). Additionally, hyperelastic nonlinear model is also described. While all of the models arrive at different constitutive relations between stress and strain within the continuum mechanics, all have been developed using basic physical principles and can predict the deformation of a cell due to an applied force.

Elastic half-space model

This model is one of the simplest ones in cell mechanics, treating the cell as a linearly elastic, homogeneous, isotropic, and incompressible half-space. Although the elastic half-space model does not account for strain- or time-dependent responses by the cell, it is useful in determining the elastic modulus of anchorage-dependent chondrocytes. It has been applied in both the testing modalities of cell indentation and micropipette aspiration to determine the mechanical properties of single cells (Harding and Sneddon 1945). The solution to indentation experiments can be obtained by solving Cauchy's equations of motion under conditions of axial symmetry. Neglecting inertial forces, the equations governing stress distributions reduce to:

$$\frac{d\sigma_{rr}}{dr} + \frac{d\sigma_{rz}}{dr} + \frac{1}{r}(\sigma_{rr} - \sigma_{\theta\theta}) = 0, \tag{0.1}$$

$$\frac{d\sigma_{rz}}{dr} + \frac{d\sigma_{zz}}{dz} + \frac{\sigma_{rz}}{r} = 0, \tag{0.2}$$

where (r, θ, z) are the cylindrical coordinates related to the half-space, σ_{rr}, $\sigma_{\theta\theta}$, σ_{zz} and σ_{rz} are the radial, hoop (circumferential), axial and shear components of the Cauchy stress tensor, respectively.

Then by representing the stress components by a single function and applying the method of Hankel transforms, a relationship between applied force and Young's modulus can be derived for a given indenter displacement (Harding and Sneddon 1945). There are three common indenter shapes that can be used to probe the cell: conical, spherical, and flat-ended cylindrical. For the rigid conical probe, the solution for the Young's modulus (E) is:

$$E = \frac{2F(1-\nu^2)}{\pi \cdot \varepsilon' \cdot a_c}, \tag{0.3}$$

where F is the applied force, ν is the Poisson's ratio of the cell, ε' is the indentation depth, and a_c is the indenter radius at the cell's surface (contact radius) (Harding and Sneddon 1945). For a rigid spherical indenter, the Young's modulus is:

$$E = \frac{3F(1-\nu^2)}{4R^{1/2} \cdot \varepsilon'^{3/2}}, \tag{0.4}$$

where R is the radius of the indenting sphere (Harding and Sneddon 1945). The last case of a cylindrical end is the most common among indentation experiments. In this situation, the cell's Young's modulus is:

$$E = \frac{F(1-\nu^2)}{2 \cdot \varepsilon' \cdot a_c}. \tag{0.5}$$

The punch model solution under the experimental modality of micropipette aspiration has been previously described by Theret et al. (1988) (Theret et al. 1988) and later compared to more complex continuum mechanics models. This model describes the Young's modulus of the cell as:

$$E = \frac{3a'\Delta F}{2 \cdot \pi \cdot L'}\phi_P(\eta), \tag{0.6}$$

where ΔF is the applied external suction pressure, a' is the inner radius of the micropipette, L' is the distance the cell is aspirated in the micropipette and $\phi_P(\eta)$ is a function of the inner and outer radii of the micropipette.

Hyperelastic model

The simplest form of hyperelastic non-linear material model is the Neo-Hookean model (Rivlin 1949). This model is an extension of the linear elastic Hooke's law to include large deformations. In the hyperelastic model, the stress $\sigma_{hyperelastic}$ can be calculated through differentiation of a strain energy density function U with respect to strain ε:

$$\sigma_{hyperelastic} = \frac{\partial U}{\partial \varepsilon}, \tag{0.7}$$

The strain energy density function is defined by:

$$U(\bar{I}_1, J) = C_{10}\,(\bar{I}_1 - 3) + \frac{1}{D_1}\,(J-1)^2, \tag{0.8}$$

where $U(\bar{I}_1, J)$ is the strain energy per unit of undeformed volume, $\bar{I}_1 = \bar{\lambda}_1^2 + \bar{\lambda}_2^2 + \bar{\lambda}_3^2$ is the first deviatoric strain invariant defined through the deviatoric stretches $\bar{\lambda}_i = J^{-1/3}\lambda_i$ where λ_i are the principal stretches and J is the elastic volume ratio, C_{10} and D_1 are temperature dependent material parameters related to the shear modulus G and Poisson's ratio ν by:

$$C_{10} = \frac{G}{2}, \qquad D_1 = \frac{3(1-2\nu)}{G\,(1+\nu)}, \tag{0.9}$$

The shear modulus G and bulk modulus K_0 can be expressed as:

$$G = \frac{E}{2(1+\nu)}, \qquad K_0 = \frac{2}{D_1}. \tag{0.10}$$

The constitutive equation for Neo-Hookean material is:

$$\sigma_s = \frac{2}{J}C_{10}\left(\bar{B} - \frac{1}{3}tr(\bar{B})I\right) + \frac{2}{D_1}\,(J-1), \tag{0.10}$$

where σ_s is the Cauchy stress tensor, $\bar{B}$ is the Cauchy-Green deformation tensor defined as $\bar{B} = \bar{F} \cdot \bar{F}^T$, $\bar{F}$ is the deformation gradient tensor and the superscript T denotes the transpose, I unit tensor.

Viscoelastic model

The viscoelastic model depicts the mechanical response of chondrocytes to an applied stress or strain, by describing the cell as containing both fluid-like and solid-like structural elements, but not separating these elements. The most common viscoelastic model for the chondrocyte is the standard linear solid (SLS), where the cell is represented using a circuit analog of springs and dashpots. The springs are strain-dependent elements, whereas the dashpots are varying according to strain rate. This model does not take into account any heterogeneous structure of the cell, including the membrane. Using this one-dimensional analog, the constitutive equation describing the stress and stress relationship is written:

$$(E_1 + E_2)\sigma + \eta \frac{d\sigma}{dt} = E_1 E_2 \varepsilon + E_1 \eta \frac{d\varepsilon}{dt}, \tag{0.11}$$

where E_1 and E_2 are the elastic constants for the two springs, η is the coefficient of viscosity, and σ and ε represent the stress and strain within the system, respectively (Özkaya and Nordin 1999). This model can predict the cellular creep response to an applied constant stress and stress-relaxation response to a step strain. The SLS model has been used to describe chondrocyte behavior in many testing modalities, including cell indentation, unconfined compression and micropipette aspiration. The indentation solution was first developed by Ting et al. (1966) to describe the behavior of a viscoelastic half-space. The SLS model has also been applied to micropipette aspiration experiments using a solution originally developed by Sato et al. (1990) and to unconfined compression creep tests on single cells using a relationship described by Leipzig et al. (2006). This model allows determining three mechanical parameters describing the single chondrocyte mechanical properties: instantaneous modulus (E_0), relaxation modulus (E_∞) and apparent viscosity (μ).

The stress-strain relationship of a viscoelastic material can also be defined with a Prony series. The Prony expansion of the time-dependent behavior can be written:

$$g_t(t) = 1 - \sum_{i=1}^{N} \bar{g}_i^p \left(1 - e^{-t/\tau_i^G}\right), \tag{0.12}$$

where $\bar{g}_i^p$ is the shear relaxation modulus, τ_i^G is the relaxation characteristic time, *N* is the number of terms in the Prony series and t is time.

Biphasic model

Developed by Mow et al. (1980), the biphasic model describes a material as having both a fluid and a solid phase. The solid matrix is assumed to be non-dissipative and incompressible, and the fluid phase is inviscid and also incompressible. Additionally, the fluid is assumed to flow through the porous solid medium, creating a frictional drag force which accounts for the time-dependent behavior and compressibility for the continuum. These assumptions enable the

following constitutive relationships to be made for the solid matrix and fluid components:

$$T^s = -\phi^s pI + \lambda_s eI + 2\mu_s \varepsilon_s \quad (0.13)$$

$$T^f = -\phi^f pI, \quad (2.15)$$

where T^s and T^f are the stress tensors for the solid and fluid phases respectively, ϕ^s, ϕ^f denote the volume fractions for solid and fluid phase, respectively and p is the hydrostatic pressure within the medium. Further for the solid matrix, ε_s is the infinitesimal strain tensor and e is its volumetric change, and λ_s and μ_s are the first and second Lamé constants for the solid phase, functions of the Young's modulus E and Poisson's ratio ν.

Applied to single cells, this model correctly depicts the interaction of both fluid and solid behavioral components inside the cell membrane. Solid elements, such as cytoskeletal proteins, the nucleus, and organelles create a porous continuum for the free flowing intracellular fluid. Through cell indentation, unconfined compression and micropipette aspiration experimental techniques, the biphasic model has been used to extract the following three intrinsic mechanical properties of the material's solid phase: the aggregate or elastic modulus (H_A, E), permeability (k) and Poisson's ratio (ν).

2.4. Bone composition and structure

In general, the subchondral bone refers to the bone directly beneath the articular cartilage. Although, subchondral bone at the tissue level is similar to bone in other sites, the organization of subchondral bone is specific. Subchondral bone consists of a layer of cortical bone plate and an underlying system of cancellous bone organized into a trabecular network.

The subchondral bone is separated from the overlying articular cartilage by a thin zone of calcified cartilage. The so-called tidemark defines the transition zone between articular and calcified cartilage. This complex biocomposite of bone and calcified cartilage provides an optimal system for distributing loads that are transmitted from the weight-bearing surfaces lined by articular cartilage. The subchondral bone also plays an important role in articular cartilage metabolism. Canals exist in the subchondral bone, which allow blood vessels to reach the cartilage to provide nutrients. Under physiologic conditions, the composition and structural organization of subchondral bone and calcified cartilage are optimally adapted to transfer loads.

Cortical bone or compact bone covers the outer surface of the bones and has a dense structure with the porosity less than 5% (Clarke 2008). The subchondral bone plate is thinner than cortical bone in most sites and contains Haversian canals which run in parallel to the joint rather than in parallel to the long axis of the bone.

Unlike the cortical bone, trabecular bone also known as cancellous or spongy bone is a more porous structure (porosity ~75%-95%) having large pores distributed throughout the bone. The pores are interconnected and filled with marrow, while the bone matrix is characterized by small plate-like and rod-like connecting elements (trabeculae) arranged as three-dimensional lattice. Trabecular bone is present near the ends of long bones, inside the small bones as well as between the surfaces of flat bones. Trabecular bone and cortical bone show

anisotropic mechanical behavior due to their structure (Yaszemski et al. 1996). The major plates in the supporting cancellous bone are arranged at right angles to the predominating stresses. These unique structural features make the subchondral bone approximately 10 times more deformable than the cortical bone shaft (Radin et al. 1970a).

Similarly to articular cartilage, subchondral bone is a natural composite whose mechanical functionality comes from its hierarchical structure. It is composed of organic and inorganic components. Minerals, principally hydroxyapatite, comprise 50–70% of the bone, collagen type I rich organic matrix 20–40%, water 5–10%, and lipids less than 3% (Clarke 2008). Hydroxyapatite contributes to the rigidity and load-bearing strength of bone, whose mechanical properties are continually adapted in response to load. The organic matrix, composed mainly of large diameter collagen fibers (type I) aligned in staggered layers along the length of the bone provides flexibility and elasticity of the bone.

Bone contains several specializes types of cells (osteoblasts, osteocytes, osteoclasts), which continually "monitor" the forces acting upon bone and can alter its composition and structure to accommodate different loads. Osteoblasts are lined along most bone surfaces and are responsible for the synthesis of collagen molecules which are then secreted into the extracellular areas where they cross-link (Ducy et al. 2000). As new layers of osteoid surround and eventually encase the osteoblasts, the cells differentiate into osteocytes, which are the most abundant cell in bone (Buckwalter et al. 1996). Once embedded, the osteocytes form dendritic extensions throughout the canniculi network within the inorganic bone regions in order to access the blood supply and communicate amongst other osteocytes (Buckwalter et al. 1996). The final cell type is the osteoclast that in response to growth factors or regional signaling from the osteocytes forms a large, multicellular unit responsible for the resorption (i.e. breakdown) of bone matrix (Boyce et al. 2009).

Subchondral bone is a "dynamic" tissue that adapts both its architecture and its mass in response to its mechanical loading environment. This attribute is known as functional adaptation and subchondral bone properties are modified through the cell-mediated process of remodeling and modeling. Remodeling or bone resorption is mediated by osteoclasts, which are responsible for degrading the bone microenvironment. Remodeling occurs continually within bones in response to external forces as described by Wolff's law, which essentially states that bone will model itself along the direction of the applied loads in proportion to their magnitude. Following this is the modeling or bone formation phase in which osteoblasts build up a new extracellular matrix. In ideal physiological conditions, the amount of bone removed during the resorption phase is balanced during the formation phase. This cellular process provides a mechanism for repairing damage that occurs to the bone during mechanical loading and stress. Reduced loading leads to bone loss (Amblard et al. 2003; Rantakokko et al. 1999), whereas increased loading can lead to increased bone mass (Biewener and Bertram 1994; Fritton et al. 2005).

2.5. Osteoarthritis: articular cartilage or bone disease?

Osteoarthritis (OA) is a widespread and degenerative chronic disease that affects up to 80% of the population over 65 years of age (Blumenkrantz et al. 2004). A recent report indicates that knee OA is likely to become fourth most

common cause of disability in women and the eight most common causes in men (Murray and Lopez 1996). With the aging population and the rise in obesity rates, the social and economic burden associated with OA is increasing. Despite its large disease burden, there are no proven preventative strategies and no treatments which stop or delay the progression of the disease. Therefore, conventional treatments of OA are mostly palliative and expensive. Clinical evaluation of cartilage deterioration is commonly assessed through X-ray, MRI and arthroscopic examination. However, these methods are sensitive only to later stages of OA including joint space narrowing, osteophytes and extensive fibrillation.

OA can be separated according to its initiation into a primary and secondary form with risk factors or causes. In general, secondary osteoarthritis arises from normal stress on abnormal cartilage or abnormal stress on normal cartilage. The risk factors for abnormal cartilage are heredity, age, gender, and nutrition, whereas abnormal loads on the cartilage may result from previous meniscal or ligamentous injuries, malalignment of the joint, muscle weakness, obesity or occupational physical activities.

Joint degeneration involves all of the tissues that form the synovial joint, including articular cartilage, subchondral bone, synovium, ligaments, joint capsule and the muscles that act across the joint. However, the primary changes consist of loss of articular cartilage, remodeling of subchondral bone and formation of osteophytes. OA is a result of both mechanical and biological events that destabilize the cartilage ECM equilibrium. The morphological, structural, biomechanical and biochemical changes of the ECM and the chondrocytes lead to the irreversible degeneration of the articular cartilage with softening, fibrillation, ulceration, and finally to cartilage loss. Progression of osteoarthritis can be divided into several stages, with each stage exhibiting increasing joint degradation.

Macroscopically, at the early stage of OA degeneration process, minimal changes are detected in the cartilage surface, which is no longer smooth. The first stage of OA is characterized by cartilage swelling, increased water content and loss of PGs from the articular surface layers shown by reduced Safranin-O staining (Guilak et al. 1994; Maroudas and Venn 1977; Sah et al. 1997; Setton et al. 1994). The PGs loss occurs preferentially from the pericellular matrix of chondrocytes (Plaas et al. 2007) and gradually extends into the ECM. Another feature of early OA includes loosening of the collagen network integrity in the superficial zone associated with increase in cartilage thickness (Buckwalter et al. 2005; Pritzker et al. 2006; Vignon et al. 1987). Diminished capability of disorganized collagen network to prevent constrain on the hydrated PGs allows the tissue to swell. As the tissue swells there is an increase in water content associated with increase in tissue permeability and loss of the normal tissue swelling pressure. Increased tissue permeability will decrease the fluid pressurization mechanism of load support in cartilage and thus results in greater stress levels of collagen-proteoglycan solid matrix (Setton et al. 1994).

During the second stage, there is an increase in synthesis of cartilage matrix and the chondrocytes proliferate and form clones and clusters in the superficial zone (McGlashan et al. 2008; Radin et al. 1991). Subsequently, fibrillation of the matrix occurs as the superficial layers of the cartilage and becomes more degraded. Thereby, cartilage loses its stiffness making it more susceptible to further mechanical disruption. Despite the attempt at early repair, there is a mismatch between the matrix synthesis and increased activity of matrix degrading enzymes. With time, this imbalance results in visible cartilage damage. As cartilage destruction progresses, the loss of PGs content reaches the deep zones, until the

complete lack of PG, indicated by the inability of the matrix to stain for Safranin-O. The loss of PG content causes reduction in the thickness of the joint cartilage (Urban 1994).

In advanced stages of OA the cartilage shows signs of complete rupture. The cartilage surface develops fissures and cracks and eventually gross ulcerations, which can reach down to the calcified zone. Cells are arranged in clusters especially around fissures or disappear completely as the disease progresses. At the end cartilage is completely disordered and replaced by fibrocartilage, scar-like tissue with fibroblast like cells. However, fibrocartilage is less able to withstand mechanical loading (Odenbring et al. 1992). In other cases full-thickness defects develop, where the bone ends lack the cartilage completely. The tidemark becomes unclear and finally is invaded by blood vessels from the subchondral bone, which penetrate into the calcified zone. Changes occur also in the underlying subchondral bone, which thickens with the formation of bony outgrowths (i.e. osteophytes) around the joint margins (Buckland-Wright 2004; Goldring and Goldring 2010). Finally, the synovium becomes inflamed as a result of cartilage breakdown.

There has been speculation for many years that bone may be one of the joint tissues triggering OA, microtrabecular fractures and their subsequent healing could increase the stiffness of the subchondral bone. This process could transmit increased load to overlying cartilage, leading to secondary cartilage damage. Radin et al. (1986) were the first to suggest the potential role for subchondral bone in the initiation and progression of OA. They stated that alterations in the subchondral bone stiffness increases stresses in the overlying articular cartilage and eventually leads to its degenerative changes and OA. However, the very early osteoarthritic changes and the relationship between cartilage and subchondral bone in OA remain poorly known.

When considering the contribution of bone in OA, it is important to distinguish between two structures, particularly the subchondral bone plate and the trabecular bone, as they are different in morphology and mechanical properties. They also respond differently during OA progression (Burr and Gallant 2012; Dedrick et al. 1993). Subchondral bone plate thickening (Grynpas et al. 1991; Shimizu et al. 1993) and an increase in the trabecular bone volume fraction (Grynpas et al. 1991; Matsui et al. 1997) have been reported in patients with late stage of OA. Additionally, it has been suggested that these changes in the subchondral bone are associated with the severity of cartilage lesions (Bobinac et al. 2003; Grynpas et al. 1991; Reimann et al. 1977). Nevertheless, whether changes in the subchondral bone plate and/or trabecular bone accompany, precede or follow cartilage degeneration at the onset and very early stages of the disease remain yet to be clarified. These limitations in the knowledge of OA are partly due to the absence of valuable means to detect early changes or to follow the natural history of the disease in humans. These limitations in the knowledge of OA are partly due to the absence of valuable means to detect early changes or to follow the natural history of the disease in humans.

Surgically-induced animal models have become valuable tools to study the early and later stages of OA and represent a good substitute for studies of OA in humans. Anterior cruciate ligament transection (ACLT) is a well-established method used in various animal models (Brandt 1994; Herzog et al. 1998; Vignon et al. 1987) to resemble early degenerative changes observed in post-traumatic human OA. ACLT is associated with immediate and severe joint instability that results in altered loading and joint kinematics, eventually leading to the initiation and

progression of osteoarthritis (Andriacchi et al. 2004; Herzog et al. 1998; Wu et al. 2000).

In the ACLT animal models, structural and compositional changes especially in the superficial cartilage have been shown to occur, such as proteoglycan loss (Marijnissen et al. 2002; McDevitt and Muir 1976; Muller et al. 1994) and alterations in the collagen network (Stoop et al. 2001). Minor collagen degradation has also been shown to take place in ACLT models (Eyre et al. 1980; Marijnissen et al. 2002; McDevitt and Muir 1976), while the collagen content has also been suggested to remain unaltered (Turunen et al. 2013). The above mentioned changes are typically associated with decreases in the mechanical properties of articular cartilage (Sah et al. 1997; Setton et al. 1994).

Subchondral plate thinning in the early OA animal hindlimb (Boyd et al. 2005; Kuroki et al. 2011; Sniekers et al. 2008), at later stages followed by an increase in the plate thickness (Dedrick et al. 1993; Hayami et al. 2006) has been reported in various surgically-induced OA models. In the ACLT feline model, however, a long-term thinning of the subchondral plate was observed (Boyd et al. 2005). The discrepancy between these surgically-induced OA models can not only be explained by the use of different animals, but also by the different post-surgical time points over which the research was conducted. Anyhow, the above-mentioned studies suggest that bone remodelling in surgically-induced OA models may be a two-stage phenomenon, where there is an initial decrease followed by an increase in the subchondral bone volume.

3. ATOMIC FORCE MICROSCOPY – CELL IMAGING AND NANOINDENTATION

3.1. Introduction

Since its introduction in 1982, scanning tunneling microscopy (STM) has shown its huge potential for the investigation of the matter at the micro- and nanoscale. This instrument, based on electron tunneling between a small tip and a surface, was limited to the study of electrically conductive samples. Few years later, Binning and Rohrer received the Nobel Prize in Physics for their discovery. In 1985, Binnig and Rohrer developed an atomic force microscope (AFM) based on the same design as their STM (Binnig et al. 1986). The AFM is a versatile system because it can directly measure biophysical properties of the surfaces due to its sensitivity at a piconewton force scale. Unlike STM, the AFM allows mapping of the surface down to sub-nanometer range and works on all types of surfaces, regardless of whether they are conductive or not (conductor, semiconductor, inorganic and organic). It can scan surfaces with up to nanometer (molecular) resolution and up to 0.01 nm vertical resolution, providing true three-dimensional (3D) surface topographical information.

In the past decade, AFM has been a major breakthrough for the material sciences. Recently, it has been widely employed in life sciences and bioengineering as well, due to its ability to generate high resolution images of biological tissues and living cells. The main advantage for using AFM in life sciences and bioengineering is that it enables investigation of biological samples and cells in near-physiological conditions (physiological hydration, temperature, salt concentration) particularly in water, saline solution or in cell culture medium with a minimal sample preparation involved. Imaging in liquids eliminates the capillary forces that are present at the tip–sample interface when imaging aqueous samples in ambient air. Beyond imaging surface topography, AFM allows measurements of various properties of biological samples and cells, such as elasticity, adhesion, hardness and friction. Finally, another advantage of the method is that it is easily accessible and commercially available to most researchers.

This chapter highlights the central features of the AFM system, with particular focus on single cell measurements and describes in more detail the advanced techniques employed for experiments described in subsequent chapters. By introducing AFM based nanoindentation, AFM as a nanotool can reveal information on the elastic and viscoelastic properties of soft materials, such as agarose gels and chondrocytes.

3.2. Theoretical principle of Atomic Force Microscopy

Basically, the AFM consists of three systems: a force-sensing system, a detection system and a positioning system, all managed by electronic controller and feedback system (Figure 3.1).

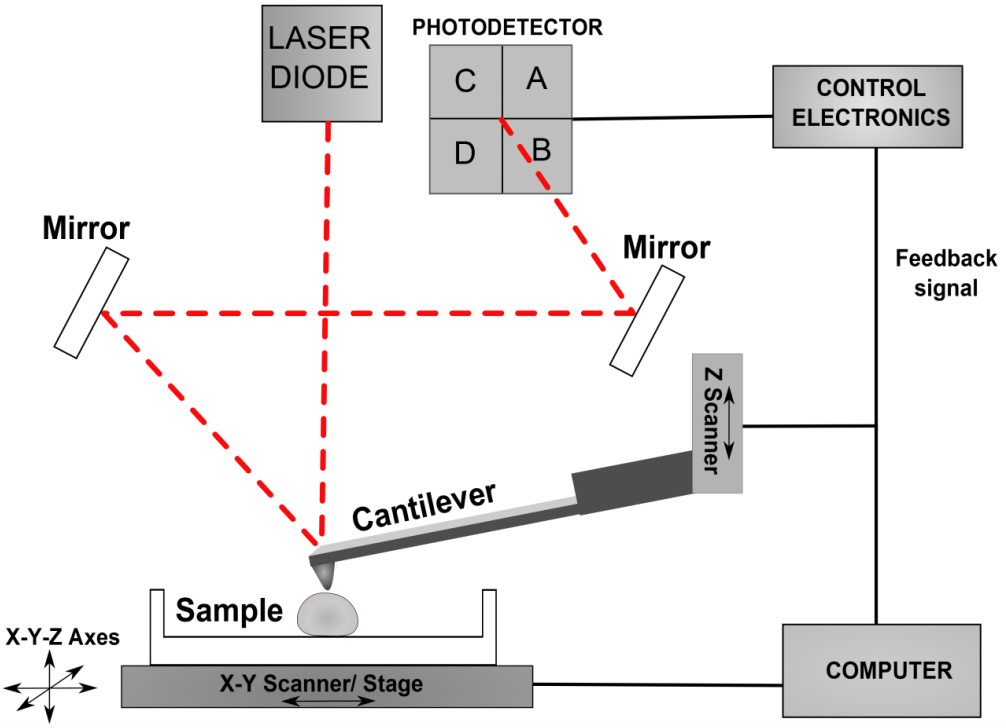

Figure 0.1 Schematic of the working principle of a typical AFM.

The key component in an AFM is the "force sensor", a nanometer tip mounted at the end of a flexible cantilever that physically "feels" the surface of the sample. The AFM probe is deflected through interatomic force interactions with the surface of the sample. Several forces typically contribute to the deflection of an AFM cantilever, such as: van der Waals interactions, electrostatic forces and capillary effects. The cantilever bends up and down when the sample is scanned under the tip due to this interaction forces between the tip and the sample, providing information on the sample height and generating a three-dimensional topography. Depending on the sample roughness, the movement of the cantilever can be very small, less than 1 nm.

A detection system that is able to detect and record such tiny variations in the cantilever bending is required. The system is also known as optical lever and it is composed of a laser diode and a position-sensitive photodetector (PSPD) consisting of four segments photodiode. The laser diode is equipped with a lens that provides a spot size in the order of a few microns. The laser is fixed at the top of the head through a plate that can be adjusted across two micrometric screws, in order to focus the spot on the cantilever. The laser beam reflected off from backside of the cantilever is directed towards the center of a four quadrants photodetector, which can record simultaneously the vertical and horizontal displacement of the laser spot. The deflection in either the vertical or horizontal direction is determined by suitably combining the four quadrants output (i.e. (A + B):(C + D) or (A + C):(B + D)), where A, B, C, and D are the respective output voltages proportional to the

beam intensity on each quadrant. When the surface of the sample attracts or repels the tip, the cantilever bends causing a shift in the reflected beam which will change the position of the beam on the photodetector. Small variations in the position of the cantilever result in large displacements of the laser spot. The actual deflection signal is calculated from the voltage that is produced in each segment of the photodetector. Subsequently, this signal is sent to the computer for data collection and to the electronic control unit, which adjusts the height of the AFM tip through a fast feedback loop. The sensitivity level or gain of the feedback system can be adjusted during AFM operation. Vertical and horizontal displacement of the laser beam on the photodetector is registered as topography and tip-sample interactions, respectively.

The coarse positioning is accomplished by step motors that are driven by the control electronics system, allowing the automatic approach of the tip to the sample. The same software allows for the acquisition of multiple images of the sample area at high resolution, particularly useful for imaging living tissues. The positioning and the fine displacement of the AFM tip relatively to the surface are done by piezoelectric scanners. Piezoelectric materials are ceramics that change dimensions in response to an applied voltage. Conversely, a mechanical strain of the piezoelectric material causes an electrical potential. Depending on how electrical current is applied, the piezoelectric scanner may extend in z-direction or flex in either the x or y direction. In this manner, the piezoelectric scanner controls the z-movement of the cantilever and the x-y scanning stage which holds the sample.

3.3. AFM imaging modes

AFM imaging can be operated in three different modes: contact mode, non-contact mode and tapping (intermittent contact) mode. These different imaging modes depend on the input signal used in the feedback circuit to control the vertical position.

In *contact mode* the tip remains in continuous soft "contact" with the sample surface (Binnig et al. 1986; Cappella et al. 1997). In this mode, the tip is less than a few ångströms away from the sample surface (10^{-10} m) and therefore the interatomic force between the tip and the sample surface is predominantly repulsive. This is mainly due to the overlap of electron clouds associated with atoms in the tip with those at the sample surface. During scanning, the AFM feedback system keeps the cantilever vertical deflection and hence the normal force between the tip and sample constant. As the topography of the sample changes, the Z-scanner moves the relative position of the tip or the sample to maintain the constant deflection. The motion of the Z-scanner is directly proportional to the sample topography. Using this feedback system, the topography of the sample is mapped during scanning by assuming that the motion of the cantilever directly corresponds to the sample topography. Even though reasonably easy to operate, there are certain drawbacks associated with this mode of operation such as damaging and deformation of the sample surface. Thus, soft cantilevers should be used for cell imaging at low forces. Moreover, combination of normal force and lateral force created by dragging motion of the probe tip across the sample and small contact areas involved result in high contact stresses that can damage or move the relatively loosely attached cells. Therefore, the contact mode imaging is more suitable for hard samples. In this mode, topographic images with vertical and

lateral resolution as small as 0.2 nm depending on the sample rigidity can be acquired (Kuznetsova et al. 2007).

In *non-contact* mode, the separation between the tip and sample is of the order of tens to hundreds of ångströms, thus the probe is subjected to weak attractive forces, van der Waals. The advantage of this mode is that the probe does not touch the surface, therefore removes any possibility of contamination or deformation of the surface by the tip as it occurs during the contact AFM scanning. The cantilever is forced to oscillate at its resonant frequency by a small piezoelectric crystal (bimorph) embedded in the probe holder and then scanned across the surface. Forces acting on the tip cause a change in frequency of the oscillating cantilever. If the frequency of the oscillating tip is kept constant, then this can be used as a feedback signal and thus image the surface. Furthermore, the total force between the tip and the sample in the non-contact regime is very low which is suitable for studying soft samples. However, the presence of a layer of liquid on the surface of a sample will result in non-contact mode imaging the surface of the liquid layer, while operating in contact mode will penetrate the liquid layer to image the underlying surface.

Intermittent or *tapping* mode is similar to non-contact mode, except the vibrating cantilever tip is brought closer to the sample such that it almost touches for a very short duration the sample surface at the bottom of its swing. The oscillation in tapping mode is as well driven by a bimorph embedded in the probe holder. When the tip contacts the sample surface, the interaction forces between the tip and sample are both attractive and repulsive causing a decrease in oscillation amplitude. The amplitude of the cantilever is such that the probe maintains enough energy for the tip to tap through and back out of the surface contamination layer. In contrast to contact mode, tapping mode is less likely to damage the sample, because it eliminates lateral forces (friction or drag) between the tip and the sample. Although it is suitable for acquiring images of cells without damaging them, the tapping mode images have low lateral resolution and it is difficult to resolve cellular structural components, for instance cytoskeleton.

3.4. AFM nanoindentation

Introduced in the early 1970s, conventional nanoindentation is actually an adaptation of the classic indentation technique for measuring the mechanical properties of materials at a scale well beyond optical capabilities. Two types of nanoindentation are commonly used to obtain the nanomechanical properties of various biological tissues. One is based on the instrumented nanoindentation (Bhushan 2008) and the other one is AFM based nanoindentation (Li et al. 2003).

The instrumented nanoindentation (also known as depth-sensing instrumentation) is using a micrometer-size indenter and the load-indentation depth is continuously monitored during the loading and unloading processes. A typical indenter tip size is of the order of some micrometers, but several years the term nanoindentation was used to distinguish it from the traditional indentation. The probe tip has a very well defined area function based on penetration depth, enabling calculation of the area of the contact based on displacement. The recorded curve is then used to calculate the material mechanical properties such as elasticity, plasticity or viscoelasticity. This technique involves larger forces than AFM nanoindenation.

The development of the AFM takes the indentation technique to a whole new level. By this technique, typical forces range from one piconewton to several micronewtons and depths can be as small as fractions of a nanometer. In comparison to the instrumented nanoindentation described above, AFM based nanoindentation uses a nanoscale AFM tip as an indentation probe. A typical AFM based nanoindentation measurement usually starts with imaging the surface of interest. The tip is then moved to a point of interest (1, Figure 3.2) and brought into contact with the sample by vertical movement. As the AFM tip approaches the sample surface, a negative deflection of the cantilever (cantilever bends downwards) may arise before the tip actually contacts the sample surface. This bending of the cantilever is mainly due to the attractive van der Waals interactions between the material surface of the probing tip and the outermost layer of the sample surface. However, in the cell nanoindenation, immersion of the AFM tip in liquid reduces the van der Waals interactions and eliminates the capillary forces (Weisenhorn et al. 1992). Upon contact between the tip and the sample (2), a larger deformation of the cantilever is observed. The tip and sample are pushed further towards each other, until a predefined force is reached (3). When the tip is withdrawn from the sample the curve often shows a hysteresis referred to as the adhesion force (4). This test cycle is referred to as "approach-retract curve", "force-displacement curve" or simply "force-indentation curve".

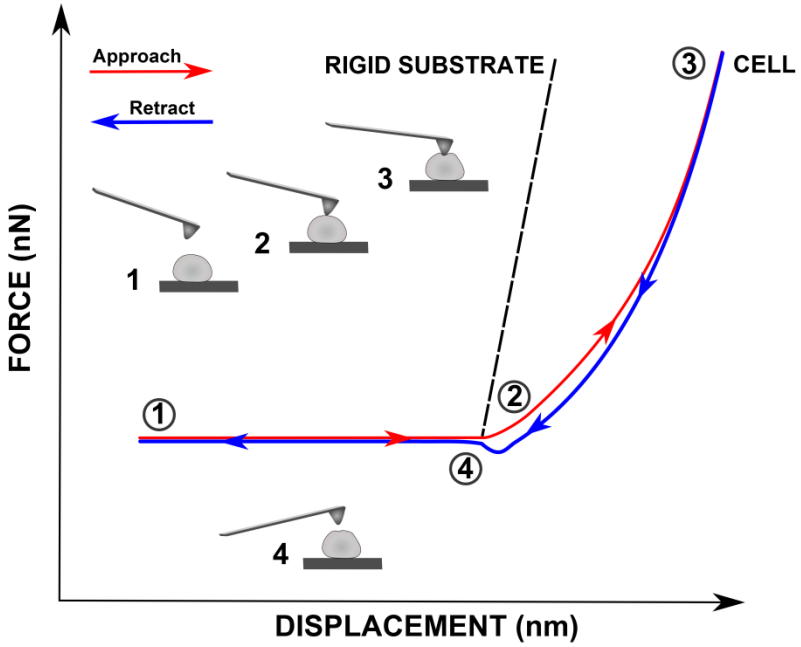

Figure 0.2 Schematic force-displacement curve obtained in AFM cell nanoindentation experiment. The approach curve is shown in red, while the retract curve is shown in blue. There is a mismatch between these two curves reflecting the viscoelastic nature of the cell in the experimental time-scale. Force curve on a rigid substrate (dotted black) is superimposed for reference.

During this approach-retract cycle, the AFM records continuously the deflection of the cantilever (d) (which is defined by the change of reflection angle (θ) of the laser beam) versus the displacement of the piezoelectric scanner (Z_{scan})

(Cappella et al. 1997). In order to convert the deflection vs. displacement curve to force vs. indentation curve, which is a premise for the fitting of the results, several steps have to be taken.

The first step is to transform cantilever deflection into force. Therefore the calibration of the cantilever sensitivity and spring constant is required. Cantilever sensitivity defines the relationship between cantilever deflection and detector voltage change. It can be determined by pressing the AFM tip on a rigid substrate (e.g. plastic culture dish). In this case, the cantilever deflection is the same as the displacement of the piezoelectric scanner (Z_{scan}), thus there is no sample deformation. However, softer materials, such as cells undergo a deformation δ equal to the difference between piezo displacement and the cantilever deflection (Figure 3.3.). According to the Hook's law, the cantilever bending force is proportional to the cantilever deflection and is evaluated by multiplying the cantilever spring constant (k') with its deflection (d). The cantilever deflection is measured directly by the AFM using the optical lever method as described previously. Although the cantilever spring constant is specified by the manufacturer, there can be quite large differences between the actual spring constant and that provided by the manufacturer. Therefore, different calibration methods were developed to accurately determine the spring constant (described in the next paragraph).

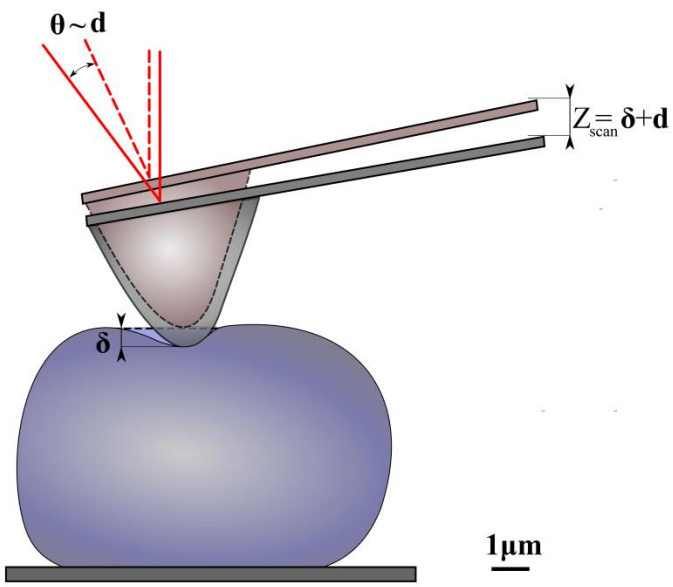

Figure 0.3 Schematic representation of a cell nanoindentation. Nanoindentation parameters used for the quantitative estimation of the cell mechanical properties are presented: d - cantilever deflection, δ – sample deformation, Z_{scan} - piezo displacement.

Another step is to determine the tip-sample contact point before the calculation. The tip-sample contact point is marked by the onset of cantilever deflection, which is small from the beginning. As a result, the tip-sample contact point has to be estimated from the whole force-displacement curve. After

completing these steps, the indentation curves can be fitted using a selected contact mechanics models which are dependent on the type probe used and the depth of indentation. In addition to elastic material properties a variety of other properties including sample deformation and energy dissipation can be extracted from the raw data.

3.5. Hertz model

Once the indentation curves have been obtained, the AFM data must be analyzed, which is typically done using the Hertz model of contact between two elastic bodies i.e. indenter and sample (Lin et al. 2007a). The Hertz model applied to AFM nanoindention relates the total cantilever force and maximum indentation into the sample to the sample elastic modulus according to the Equations (2.3)-(2.5).

The Hertz model relies on a number of simplifying material assumptions:

- the material under study comprises a large system with a flat surface (a half-space)
- the material returns to its original shape when the load is released (elasticity)
- the material is linear (Hooke's law)
- there is no preferred direction or point in the bulk material (isotropy and homogeneity)

The Hertz model as applied to AFM nanoindentation requires knowledge of the tip geometry as presented in the chapter 2.3.2.2. Assuming a spherical geometry of the tip apex, the spherical Hertz model has been applied to nanosized tips to determine mechanical properties of living cells (Radmacher et al. 1993; Radmacher et al. 1995). The same model was applied in this work to determine the Young's modulus of chondrocytes.

3.6. Cantilever and tip probe selection

The cantilevers of commercial probes have a rectangular or triangular shape, usually 100–200 μm long, 20–40 μm wide and 0.5–1 μm thick. Nominal properties specific to each cantilever type, such as resonant frequency f and spring constant k' are typically provided by the manufacturer. Frequently, the back surface of the cantilever is coated with a gold layer to increase reflectivity. The most common probe materials are silicon or silicon nitride. This material, while easier to fabricate with small thickness, is translucent at thicknesses required for low-spring constant levers (~0.5 μm). Adequate reflection of the laser beam requires that these levers should be coated (on the opposite side of the tip) with a metallic layer (typically gold). The metal and silicon component have different thermal expansion coefficients and therefore induce static bending of the lever in response to changes in temperature (0.001ºC shift can produce a 10 nm deflection), known as the thermal bimetallic effect (Marti et al. 1992). The deflection laser itself can heat a cantilever by as much as 10ºC in air. In fluids, however, the heat from the laser is dissipated such that operating temperatures are normally 3ºC above ambient, but thermal equilibrium can take more than 1 h. Also, the fluid readily conducts heat from the microscope stage and surrounding. Thus, thermal isolation and stability of the imaging chamber becomes necessary for accurate force measurement and control.

It is known that the resonance frequency of a cantilever drops dramatically when it is immersed in liquids, mainly due to the added effective mass of the liquid. This added mass results in a decrease of the resonance frequency, typically by a factor of about 3 (Walters et al. 1996). However, due to the difficulties in determining the resonance frequency of the cantilever in liquid, the spring constant calibration in this work was performed in air.

Due to the different stiffness of the tested samples, the spring constant of the cantilever has to be adequately chosen in order to match the stiffness of the sample of interest. This is an important step in order to achieve the correct sensitivity in the nanoindentation measurements. For instance, in the case of probing the mechanical properties of hard substrates such as silicon or graphite, cantilevers with high spring constants (k'~300 N/m) are required, since the applied forces required to test the onset of plastic deformation of such materials is in the order of several hundreds of micronewtons. By contrast, the required force to probe a single cell is in the order of a few micronewtons. In this particular case, soft cantilevers of k'~0.05 N/nm are required.

3.7. Cantilever and tip probe calibration

For quantitative AFM applications, such as nanoindentation the spring constant of the cantilever must be precisely determined since the quoted value provided by the manufacturer is only an approximation based on the dimensions of the cantilevers. In some cases, the spring constant of the cantilever can be over 20% off from the quoted value.

There are several methods to determine the spring constant of the cantilever with similar uncertainties, such as static and dynamic methods (Cook et al. 2006; Gibson et al. 2005; Ohler 2007). Static methods utilise the deflection experienced by a cantilever when a constant known force is applied to the cantilever (Gibson et al.1999, Butt et al. 1992, Neumeister et al.1994). Dynamic methods focus on the dynamic behaviour of a cantilever, which includes measurement of the thermal response of the cantilever and measurement of the change in resonant frequency caused by the addition of known masses to the cantilever (Butt and Jaschke 1995; Gibson et al. 1996; Neumeister and Ducker 1994). Dynamic methods include three of the most widely used cantilever calibration methods: the added mass method, the thermal tune method and Sader's method.

Considering a beamlike cantilever made out of silicon or silicon nitride, the spring constant k' can be determined from the geometry of the cantilever:

$$k' = \frac{Eb^3 w}{4L^3}, \qquad (0.1)$$

where E is the Young's modulus of the material (i.e. for silicon E = 1.69*10^{11} N/m^2) and b, w and L are the thickness, width and length of the cantilever, respectively.

Cleveland et al. (1993) proposed a method for the determination of the spring constant of the cantilever based on the attachment of a known mass to the end of the cantilever and measuring the change in resonant frequency. The resonant frequency of a harmonic oscillator can be combined with the spring constant values of a cantilever as:

$$f = \frac{1}{2\pi}\sqrt{\frac{k'}{m}} = \frac{1}{4\pi}\frac{b}{L^2}\sqrt{\frac{E}{\rho}}, \tag{0.2}$$

where m is the mass of the cantilever, ρ is the density of the material and E the elastic modulus.

This equation can be used to calculate the cantilever spring constant if its mass is known. However, the AFM cantilever beam is not a simple point mass added at the end of a spring, but has its weight distributed along its length so Equation (3.2) is usually modified by considering and effective mass, m_0. Although, measuring the effective mass of a cantilever is complicated, Cleveland et al. (1993) proposed a method based on measuring the changes in resonant frequency f, as small masses, m^*, were added to the cantilever:

$$\omega^2 = \frac{k'}{m^* + m_0}, \qquad f = \frac{\omega}{2\pi}. \tag{0.3}$$

where ω is the first radial resonant frequency.

A plot of added mass, m^* vs. ω^{-2} has a slope equal to k' and an intercept equals to the effective cantilever mass m_0. Cleveland et al. (1993) derived the following Equation (3.3), which allows calculation of k' with reasonable accuracy by just measuring the unloaded resonant frequency of the cantilever, assuming that the information on the length and width of the cantilever are accurate.

$$k' = 2w(\pi L f)^3\sqrt{\frac{\rho^3}{E}}, \tag{0.4}$$

where L is the length of the cantilever, w its width, ρ is the density of the material, E the elastic modulus and f the measured resonant frequency.

A cantilever in thermodynamic equilibrium with a thermal bath at a temperature T has a thermal energy $k_B'T$, k_B' being the Boltzmann's constant. Considering the cantilever as a system with just one degree of freedom (it can move only up and down), the thermal energy increases the elastic energy stored in the cantilever as:

$$\frac{1}{2}k'A^2 = \frac{1}{2}k_B'T, \qquad A = \sqrt{\frac{k_B'T}{k'}}, \tag{0.5}$$

where A is the oscillation amplitude of the cantilever.

The thermal noise method, also referred to as the thermal fluctuation method for determining the cantilever spring constant is widely used, as it eliminates the need for the dimensions and the mechanical properties of the cantilever. Some commercial AFM software can do the cantilever force calibration with high precision automatically using this method.

A more accurate method was proposed by Sader et al. (1995) and it was improved and applied to rectangular cantilevers in 1999. This method require to know the width and length of the cantilever, the experimentally measured resonant frequency and quality factor of the cantilever, and the density and viscosity of the fluid (properties of air: density ρ_{air}=1.18 kgm^{-3} and viscosity η_{air} = 1.86 x10^{-5} kgm^{-}

$^{1}s^{-1}$). This method was used as well for simultaneous calibration of the torsional spring constant of rectangular cantilevers. The advantages of these methods are that the thickness, density and resonant frequency in vacuum of the cantilever are not needed. Moreover, they are rapid to use, noninvasive and nondestructive. Since the shape of all the AFM cantilevers used in this study is rectangular, the method developed by Sader et al. (1999) (Sader et al. 1999) is particularly suitable. This method incorporates theoretical results for the effects hydrodynamic forces from the air on the resonance of a rectangular lever. The spring constant k' is calculated as:

$$k' = 0.1906\rho w^2 L Q \Gamma_i(\omega)\,\omega^2, \qquad (0.6)$$

where ρ is the density of the fluid, w and L are the width and length of the AFM cantilever, ω and Q are the radial resonant frequency and quality factor of the fundamental resonance peak, $\Gamma_i(\omega)$ is the hydrodynamic function of the cantilever (Sader et al. 1999). This method avoids much of the error associated with the thermal method because it does not require the calibration of the optical deflection sensitivity, only the resonance frequency, Q-factor, geometry of the lever, the density and viscosity of the air.

3.8. AFM in liquid environment

Typically, the study of biological tissues with any AFM requires immobilization of the sample of interest onto a solid support that can be held on the sample platform of the AFM. For living cell experiments, the cells must be isolated from the tissue in which they exist naturally and cultured directly on a flat, solid surface. Typically, this involves culturing the cells onto a plastic ware (Petri dish) or glass cover slips, maintained in nutrient containing media at 37ºC and in 5% CO_2. Before loading into an AFM, the cell culture media is replaced by physiological saline solution, in order to remove cell debris and unattached cells. Otherwise, it is likely that debris or unattached cells stick to the cantilever during AFM experiments. During AFM experiments, evaporation of the fluid can occur due to the heating of the solution by the energy dissipated from the laser diode. To maintain the cell viability, the new commercially available biological AFMs are equipped with temperature control unit, CO_2 atmosphere control and perfusion apparatus. Although the exchange of the fluid during AFM experiment is possible, the flow induced can disturb considerably the AFM cantilevers. Furthermore, the high sensitivity of the AFM cantilevers to variations in temperature may lead to cantilever bending or thermal drift. Due to these drawbacks, temperature control of the cell medium and perfusion of fluid was not implemented for AFM experiments described in this thesis.

3.9. AFM stress-relaxation

Chondrocytes manifest varying levels of resistance to deformation (elasticity) and flow (viscosity) in response to an applied force. This mechanical behavior, known as viscoelasticity, is dependent on the composition and organization of subcellular structures, particularly the cytoskeleton. Assuming a cell behaves as an elastic material, its resistance to deformation is proportional to the applied stress, but inversely proportional to the resulting strain. This resistance to deformation is measured experimentally as the elastic modulus. Moreover, elastic

materials subjected to a constant stress exhibit a constant strain and recover their original shape completely after the stress is removed. However, cells are viscoelastic materials and exhibit both elastic and viscous properties. Specifically, when a viscoelastic material is kept at a constant strain, the applied stress in the material relaxes or decreases over time, a phenomenon called stress relaxation (Figure 3.4). As described in chapter 2.3.2.2, various viscoelastic and biphasic/poroelastic properties can be extracted from this experimental stress-relaxation data.

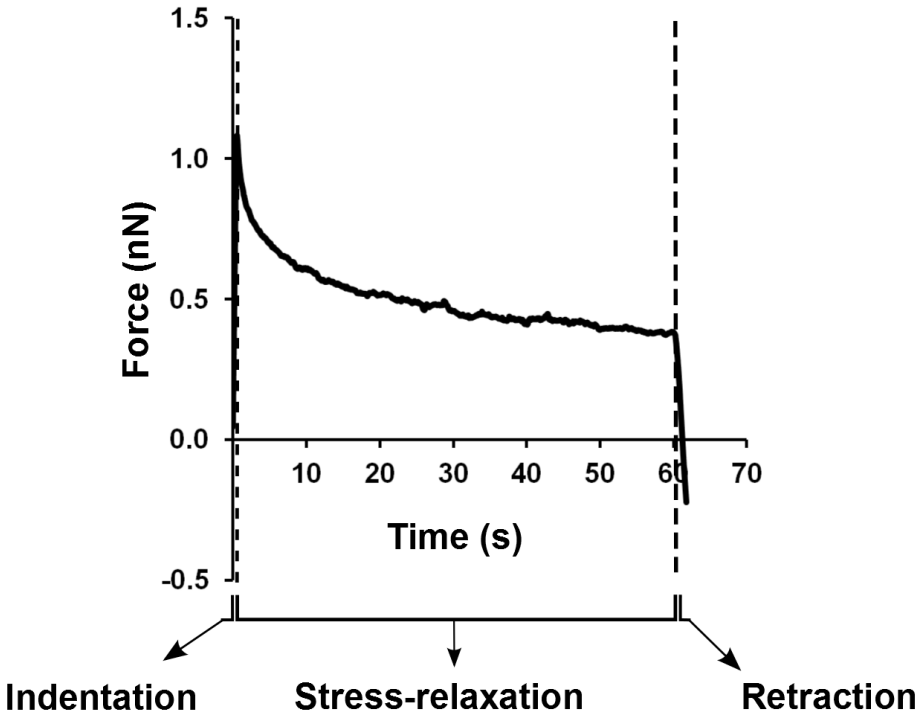

Figure 0.4 Typical stress-relaxation curve for a chondrocyte.

4. MICRO-COMPUTED TOMOGRAPHY AND ANIMAL MODELS OF OA

In medical imaging, computed tomography (CT) is an X-ray based technique that generates cross-sectional images of an object that can be utilized to noninvasively visualize structures in 3D. Lately, there has been an increasing need for preclinical experimentation such as tissue samples or even whole animals that are used as models to evaluate various diseases, such as osteoporosis or osteoarthritis. While the spatial resolution of clinical CT scanners typically reaches 0.5mm, micro-CT is able to provide a spatial resolution of 10 to 100 times higher in the range between 5 and 50 μm (Feldkamp et al. 1989; Kuhn et al. 1990). Therefore, micro-CT has become a powerful 3D imaging technique to evaluate the subchondral bone microarhitecture in animal models at a resolution of several microns. Compared to conventional histology, micro-CT has many advantages including maintenance of the sample integrity, reduced time for image acquisition and the possibility of 3D analysis of the bone.

In general, the micro-CT system consists of a microfocus tube which generates a cone-beam of X-rays, a rotating specimen holder on which the object is mounted and a detector system which acquires the images. One of the main differences to clinical CT scanners is that during micro-CT imaging, the source-detector geometry is fixed, while images are taken from rotating specimen. The basic physical principles of micro-CT, however, are similar to clinical CT. Micro-CT produces cross-sectional images representing the specific linear X-ray attenuation properties of the test specimen. An X-ray beam that travels through a specimen is attenuated by the X-ray attenuation properties of the specimen (density, thickness and mass attenuation coefficient) in its path and the resulting attenuated X-ray beam is measured and converted to an electrical signal. In order to obtain the image of a section of a specimen it is necessary to obtain many projections in constant angular steps and hence the attenuation at each point in the specimen can be reconstructed resulting in a 3D attenuation image of the specimen (Figure 4.1).

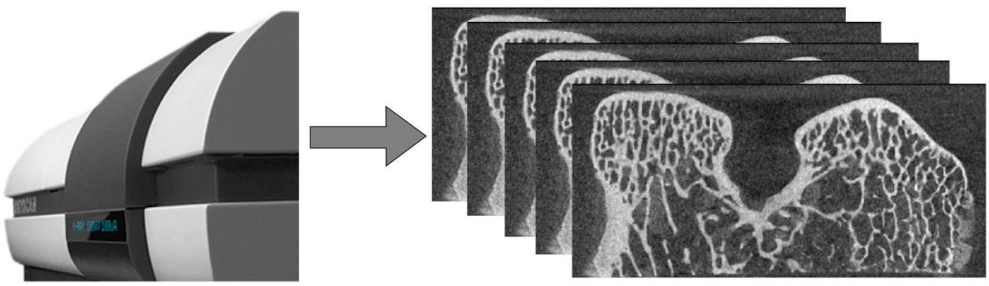

Figure 0.1 Typical cone-beam micro-CT for bone assessment. Cross-sectional images are reconstructed into a 3D structure.

Beam hardening artifacts in gray level, which may appear in the images, are caused due to the preferential attenuation of low energy photons. This process can

be minimized using metallic filters to eliminate low energy photons from the incident radiation. The image reconstruction is typically based on a filtered backprojection algorithm, such as Feldkamp image reconstruction algorithm. Reconstruction times can vary depending on the number of voxels used and number of projections acquired. Typically, voxels from micro-CT images have all three dimensions equal and therefore are described as isotropic voxels. After reconstruction, image data can be used for further processing and structural analysis.

Segmentation of subchondral bone in grayscale images is an important step to separate the mineralized structures from soft tissue for subsequent quantitative analysis. Applying a global threshold is the most widely used technique in subchondral bone segmentation (Martin-Badosa et al. 2003; Parkinson et al. 2008; Ruegsegger et al. 1996). The advantage of using a global threshold is that it is efficient and requires setting only one parameter. Since the X-ray attenuation ratio of bone to marrow is very high, a fixed CT value or a percent of the CT-value range is chosen as a global threshold, above which all voxels are classified as bone. In most studies, using a single global threshold for all scans provide that the differences between study groups are due to experimental effects rather than image-processing effects. However, in case of limited resolution (e.g. partial volume effect) or low signal-to-noise ratio (e.g. in the case of in-vivo imaging), more sophisticated segmentation tools are required, such as local segmentation approaches, where the inclusion of each voxel is based on its local neighborhood (Waarsing et al. 2004). Furthermore, due to the differences in the morphological and mechanical properties between subchondral bone plate and trabecular bone, these two structures need to be assessed separately. Precise contouring for separating the subchondral bone plate and trabecular bone regions can be achieved manually on a slice-by-slice basis or using automated algorithms (Buie et al. 2007; Kohler et al. 2007). The segmented volume of interest is then evaluated to quantify microstructural parameters, after which the 3D images can be viewed. The microstructural parameters of subchondral bone commonly quantified are: subchondral bone plate thickness, bone volume fraction, trabecular spacing, trabecular thickness and mineral density.

Micro-CT imaging is currently applied to study subchondral bone changes in various animal models of OA. The first study (Layton et al. 1988) to quantify bone morphology using micro-CT was a study of subchondral bone changes in a guinea pig model of OA. They observed that initial loss of trabecular bone volume fraction with thinning of subchondral bone trabeculae was followed in the advanced stages of OA by thickening of the trabeculae and increases in trabecular bone volume. There are a number of surgical methods by which an injury may be induced in animal models of OA. Anterior cruciate ligament transection (ACLT), menisectomy or combination of both, are commonly used surgical-induced models of OA. During a 54-month longitudinal micro-CT study in canine ACLT model of OA, Dedrick et al. (1993) demonstrated an increase in subchondral bone plate thickness, accompanied by a decrease in trabecular thickness. Batiste et al. (2004) examined volumetric bone mineral density, joint space and bone volume fraction in a rabbit ACLT model of early OA using micro-CT. Subchondral bone volume fraction and bone mineral density decreased in the OA animals. Likewise, a decrease in subchondral plate thickness and trabecular bone volume fraction was observed in a feline model of OA at 16 weeks post-surgery (Boyd et al. 2005). In a rat ACLT and menisectomy model of OA, decreased subchondral bone thickness was associated with early development of cartilage lesions, which preceded significant cartilage thinning and subchondral bone sclerosis (Hayami et al. 2006). Furthemore, in a dog ACLT model

of OA (Sniekers et al. 2008), micro-CT revealed reduced subchondral bone plate thickness in ACLT knees compared to control knees already at 3 weeks post-surgery. In some of these studies, the early decrease in subchondral plate thickness was followed by late plate thickening. Taken together, these micro-CT studies show that the subchondral bone alterations are not uniform, differing between subchondral bone plate and trabecular bone and are highly dependent on the stage of the disease. However, early features of OA in both articular cartilage and underlying subchondral bone remain largely unknown.

5. AIMS

The present thesis explores the applications of different nano- and micro techniques with the end goal of characterizing the biomechanical properties of single chondrocytes, structural, compositional and biomechanical properties of articular cartilage and underlying bone in order to establish structure-function relationships at different length scales.

The aim of this thesis was to provide answers to the following more specific questions:

- Does the AFM nanoindentation used in this research offer a consistent approach to quantitatively measure the mechanical properties of soft materials and local nonlinear properties of chondrocytes?
- How is the local nonlinear mechanical response of chondrocytes modulated by the actin cytoskeleton in AFM nanoindentation?
- Does chondrocyte viscoelasticity in AFM nanoindentation arise from fluid flow-dependent or flow-independent mechanism? How does cellular viscoelasticity change in altered cells?
- How is the subchondral bone thickness and microstructure altered in a very early stage of experimentally-induced OA?
- Do subchondral bone changes precede articular cartilage changes (or vice versa) in a very early stage of experimentally-induced OA?

Specifically, the main objectives of the thesis were:

- To develop a consistent methodology to characterize mechanical properties of soft materials and local nonlinear elastic properties of bovine cartilage chondrocytes using AFM nanoindentation;
- To quantify the effects of cytoskeleton on local nonlinear elastic properties of bovine chondrocytes using AFM nanoindentation;
- To determine the time-dependent viscoelastic responses of normal and altered chondrocytes using AFM nanoindentation and Finite Element modelling;
- To assess the changes in the subchondral bone plate thickness and trabecular bone microstructure in a rabbit model of early OA by the use of micro-computed tomography;
- To investigate changes in the structure, composition and mechanical properties of articular cartilage in a rabbit model of early OA and compare those changes to bone alterations;

The answers to these questions could give essential information on chondrocyte structure-mechanical function relationships and mechanobiology, as well on subchondral bone and articular cartilage tissue level properties in early stage of experimentally-induced OA. This knowledge should facilitate development of new methods for early diagnosis and treatment of OA.

6. ATOMIC FORCE MICROSCOPY (AFM) NANOINDENTATION OF SOFT MATERIALS AND CHONDROCYTES

6.1. Introduction

Articular cartilage mechanobiology is modulated by the mechanical signals perceived by chondrocytes. Those signals are affected not only by the joint loading and tissue properties, but also by the mechanical properties of articular cells. Chondrocyte stiffness, i.e. the mechanical properties of the cell, is an important indicator for how a cell responds to mechanical perturbations in the surrounding matrix environment. Understanding the biomechanical responses of single chondrocytes and quantifying their mechanical properties is essential for understanding normal physiological behavior as well as elucidating the pathogenesis of OA.

Several experimental devices have been employed to quantify the mechanical properties of single cells. These include micropipette aspiration, unconfined compression, cytoindentation, cytodetachment and AFM as described in the chapter 2.3.2 (Darling et al. 2006; Guilak et al. 2002; Jones et al. 1999; Leipzig and Athanasiou 2005; Ofek et al. 2009a; Shieh and Athanasiou 2006; Trickey et al. 2000; Trickey et al. 2006). These devices and techniques increased the understanding of how mechanical forces influence cell function.

AFM has found wide applicability as a nanoindentation tool to measure the mechanical properties of biomaterials such as soft tissues (Lin et al. 2007a; Park et al. 2004; Stolz et al. 2004), cells (Costa et al. 2006; Darling et al. 2006; Radmacher 2007; Rotsch et al. 1997) and gel constructs (Nitta et al. 2000) at nano- and microscale. The versatility and utility of AFM lies in the capability to measure the mechanical response at precise sample locations and at shallow depths, while monitoring time, depth and force response. The high spatial resolution allows for the determination of local mechanical properties of cells at the nanoscale. However, even though AFM has been successfully used to probe mechanical properties of cells, there are a number of experimental challenges in the mechanical testing of cells with AFM in general, and nanoindentation in particular. These challenges can be divided into two categories: those associated with instrumentation, including tip geometry, spring constant calibration and those associated with cells. In fact, cell responses to AFM nanoindentation are governed by the elastic, viscoelastic and adhesion properties of the cells. Typically, homogeneous materials are used as reference materials since they can be assumed to have continuous mechanical properties throughout the whole structure. In order to establish the ability to measure cellular mechanical properties using the AFM, a reliable methodology for AFM nanoindentation using soft materials (agarose gel) was initially proposed.

Much of the work done in the past on cell mechanics using AFM has focused on trying to determine the elastic properties of cells, in particular determining the elastic modulus (Berdyyeva et al. 2005; Ladjal et al. 2009; Radmacher 2007). For this purpose, large spherical particles (5-10 μm) were glued to the AFM cantilevers. It should be noted, however, that these large AFM tips measure more of the bulk

elastic properties of cells. In contrast, the AFM nanosized probes characterize more of the local cell elastic properties. So far, a few AFM studies (Ng et al. 2007) have examined the local elastic properties of chondrocytes. Traditionally, Hertz model has been extensively used to characterize the contact problem between the cantilever AFM tip and the sample surface to extract the local elastic modulus of the cells. This model includes several assumptions about cell AFM nanoindentation experiments.

In fact, within the chondrocytes the aqueous gel nature of the cytoplasm, heterogeneously distributed cytoskeletal elements, nucleus and other organelles are crucial factors that affect the mechanical properties of the cells. The chondrocyte cytoskeletal elements (actin filaments, intermediate filaments and microtubules) are mechanically coupled and the forces generated in one network can be transferred to another. These constituents are considered continuous bodies with various material characteristics. Aberrations occurring in the organization of cytoskeletal elements in OA influence the mechanical properties of the chondrocytes. Significant increases in elastic and viscoelastic properties were observed in OA chondrocytes from end-stage pathology (Trickey et al. 2000). Interestingly, a recent study reported that the mechanical properties of cartilage chondrocytes changed profoundly also with aging (Chahine et al. 2013; Steklov et al. 2009). Clearly, the biomechanical properties of the chondrocytes are dependent on cytoskeletal element organization irrespective to age or pathology.

Recently, it has been shown that the cells exhibit a non-linear stress-strain relationship in AFM nanoindentation (Chahine et al. 2013; Costa et al. 2006). However, this non-linear cell mechanical behavior is subjected to controversy for various reasons. First, it has not been systematically found in different types of cells. Second, there is a debate concerning the origin of this stress-strain dependent cell behavior. It could be related to the cytoskeleton structural properties, material properties of its elements or even to the size and geometry of the AFM indenter used. To examine the role of actin cytoskeleton in determining the mechanical properties of cells, investigators commonly use fungal agents that interfere with polymerization of the actin cytoskeleton, such as Cytochalasin D.

A recent study (Moeendarbary et al. 2013) showed that for very small time scales, the cells behaved as a poroelastic material. The authors suggested that the water redistribution through the solid phase of the cytoplasm play a fundamental role in setting cell viscoelasticity. In chondrocytes, this time-dependent, viscoelastic behavior has been attributed to flow-dependent (fluid-solid interactions and fluid viscosity) (Koay et al. 2003; Shin and Athanasiou 1999) as well as flow-independent mechanisms (inherent viscoelasticity of the cytoskeleton) or combination of those two. However, there is no direct evidence of which one of these mechanisms is responsible for the viscoelastic behavior of chondrocytes under AFM nanoindentation.

Taken together, the goals of this study were: (i) to establish a reliable methodology for AFM nanoindentation using soft materials such as agarose gels, (ii) to characterize local elastic properties of bovine chondrocytes as a function of deformation in normal and Cytochalasin D treated chondrocytes and (iii) to study the local viscoelastic properties of chondrocytes using a combined approach of experimental AFM nanoindentation measurements with finite element (FE) analysis Time-dependent responses of normal and Cytochalasin D treated chondrocytes are measured and material models with different degrees of complexity of a chondrocyte are fitted to the experimental data.

6.2. Materials and methods

6.2.1. Agarose gel preparation

Agarose is a natural polysaccharide polymer extracted from marine red algae, purified and supplied in powder form. It dissolves in water at temperatures between 50°C and 65°C. At temperatures between 26°C and 30°C the sugar polymers crosslink with each other, causing the solution to "gel" into a semi-solid matrix. Additionally, the properties of agarose gel, such as strength and permeability can be adjusted by changing the concentration of the polymer. Typically, by increasing the concentration of the agarose, the mechanical stiffness increases and the porosity or void space between polymer chains decreases (Nayar et al. 2012; Stolz et al. 2004). Lately, the ability for agarose to form into a hydrogel has led to its use for cartilage tissue engineering.

In this study, 2.5% agarose gel was prepared by combining 0.25 grams of agarose powder for molecular biology grade (Electran, BDH Laboratory Supplies) with 10 ml of distilled water. Then, the agarose solution was thoroughly mixed and heated in a microwave oven for 1 min well above its melting point. After cooling down an aliquot of melted agarose was poured into a 60 mm diameter Petri dish and allowed to spread and solidify. Before the nanoindentation measurements, the agarose gel was covered with deionized water to ensure its hydration. Small pieces (~1200 µm thickness) of agarose gel were cutted with a scalpel and fixed with clips in an AFM open liquid cell.

6.2.2. Chondrocyte cultivation

Primary chondrocytes were isolated from full-thickness articular cartilage of bovine (estimated age 13-22 months) femoral condyles by collagenase digestion (Qu et al. 2006). Cartilage pieces were incubated with 0.5 mg/ml of hyaluronidase in serum-free Dulbecco´s Modified Eagle Medium (DMEM), supplemented with 250 µg/ml fungizone and 10 mg/ml gentamycin in an incubator at 37°C with 5% CO_2 for 30 minutes. Digestion was then continued overnight with 0.3 mg/ml of collagenase and 0.2mg/ml of deoxyribonuclease (DNase) in DMEM supplemented with 1% fetal calf serum (FCS), 250 µg/ml fungizone, 0.5µg/ml of ascorbic acid, and 10 mg/ml gentamycin. Next morning, the isolated chondrocytes were washed twice with phosphate-buffered saline (PBS), counted and plated in monolayer cultures at density of $1x10^6$ cells on 60 mm diameter Petri dish. Cell cultures were maintained in DMEM culture medium with low-Glc (glucose) (5.5 mM) supplemented with 10% FCS, penicillin (100 U/ml), streptomycin (100 µg/ml) and 2 mM L-glutamine at 37°C and in 5% CO_2 atmosphere. After 24 hours cultivation, the fresh cell culture medium was changed to the cells after washed with PBS. Before the actual AFM measurements, the cell culture medium was changed to PBS, which was used as liquid environment during the experiments. To ensure the viability of the investigated chondrocytes, all measurements were performed within 2 h after removing the chondrocytes from the incubator. All AFM experiments were conducted in liquid and at room temperature.

6.2.3. Disruption of chondrocyte actin cytoskeleton using Cytochalasin D

Chondrocytes were isolated and cultured as described above. Cytochalasins are a family of cell-permeant fungal toxins that can block actin polymerization and Cytochalasin D is one of the most specific and potent drug among this family of molecules. Functionally, Cytochalasin D inhibits actin polymerization by blocking actin monomer addition at the rapidly growing end of the actin filament (Cooper 1987).

In this study, Cytochalasin D (Sigma-Aldrich, St. Louis, MO, USA) was dissolved in dimethyl sulfoxide (DMSO) and kept as a stock solution at -20^0C. To avoid cytotoxicity, Cytochalasin D in DMSO solution were performed first and then diluted in DMEM cell culture medium. Cytochalasin D treatment was applied to cells at final concentration of 2μM. Several studies clearly demonstrated that this concentration of cytochalasin D causes a major disruption of actin cytoskeleton (Ofek et al. 2009b; Trickey et al. 2004). Before AFM indentation experiments, chondrocytes treated with Cytochalasin D were kept in 5% CO_2, 95% humidified air incubator at 37°C for 30 minutes.

6.2.4. Basic components of XE-100 AFM

All AFM measurements were performed using a XE-100 atomic force microscope (Park Systems, Santa Clara, CA, USA). The XE-100 system consists of four primary components: the XE-100 Stage, the XE-100 Control Electronics, a computer and a video monitor. The measurements are performed on XE-100 Stage, whose movement is controlled by XE-100 Control Electronics and the computer. XE Software consists of two separate programs: XEP, a data acquisition program that communicates with the XE Control Electronics and XEI an image processing program. XEP controls and operates the XE-100 AFM system in order to collect the raw data.

The figure 6.1 shows overall structure of the XE-100 Stage with the acoustic enclosure open. The acoustic enclosure attends the acoustic damping that can interfere with the AFM measurements. The XE-100 is extremely sensitive to external vibrations, thus the whole system is placed on a marble table suspended by thick ropes. A CCD camera mounted on the XE-100 Stage provides through an optical microscope a top-down view of the cantilever and of the region of interest on the sample surface. Moreover, the CCD camera is employed for the laser alignment.

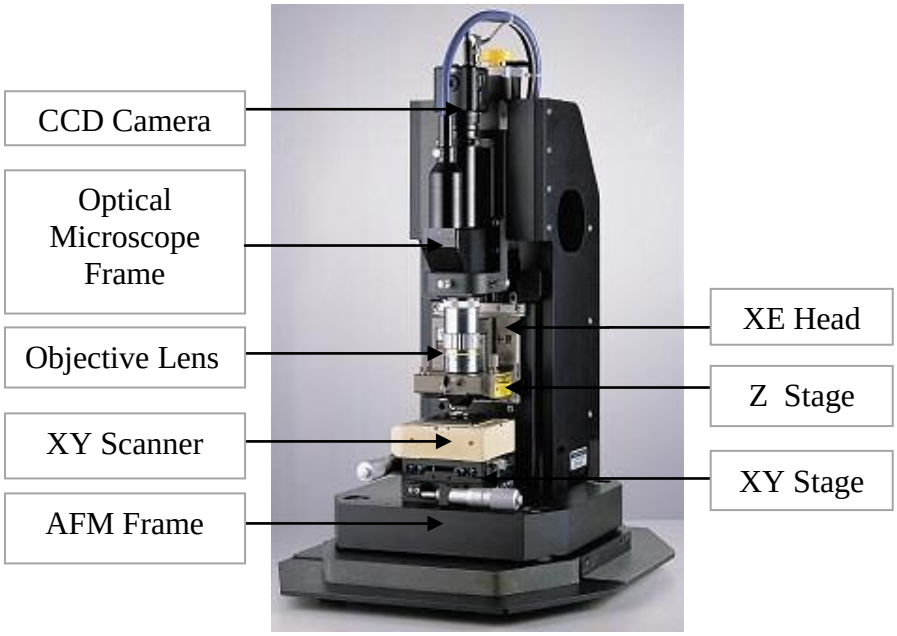

Figure 0.1 Illustration of main XE-100 Stage components.

The XE head, the component which actually interacts with the sample and performs the measurements consists of two completely separated piezoelectric scanners: Z scanner and XY scanner. A unique characteristic of the XE-100 compared to that of conventional AFMs is that the Z scanner is completely separated from the XY scanner. Z scanner allows the AFM tip to maintain constant feedback conditions (force or distance) as it is moved over the sample surface in vertical direction, while the XY scanner moves the sample in horizontal direction. The Z-axis scan range is 12 μm, whereas the X- and Y-axes range of the scan head is 50 μm. The XE-100 head contains the actual probe (the cantilever-tip assembly mounted on a special holder), as well as the optic systems (laser and Position Sensitive Photo Detector (PSPD)) for detecting the cantilever deflection.

The cantilever and the PSPD move together with the Z scanner, while the laser beam, a steering mirror, and a fixed mirror in front of the PSPD are fixed relative to the scanner frame. The laser beam, positioned at the one side of the scanner, is aimed at a prism that is situated above the cantilever. The prism reflects the laser beam downward and onto the back surface of the cantilever. The laser beam will always hit the same spot on the cantilever's surface since the Z scanner only moves vertically. Therefore, once the laser beam is aligned, there is no need to realign the laser beam, even after the Z scanner has been moved up and down to change samples. The steering mirror, located at the front of the Z scanner assembly, adjusts the reflection angle of the laser beam that is reflected off the cantilever's surface. The steering mirror reflects the laser beam to a fixed mirror which, in turn, reflects the beam at once to the PSPD. Another feature of this alignment design is that as a result of placing the second (fixed) mirror next to the PSPD, it allows changing the Z scanner position without having to readjust the position of the PSPD. Therefore, only the deflection of the cantilever will be detected, independent of the Z scanner movement (Figure 6.2).

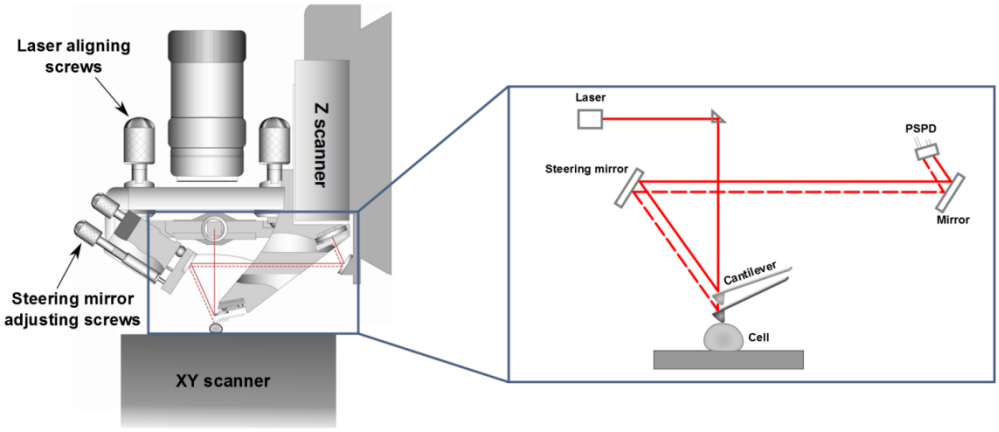

Figure 0.2 AFM cantilever movement detection mechanism.

The AFM imaging under fluid generally requires additional piece of hardware such as a fluid cell. The fluid cell is a small glass assembly that houses the liquid phase. The glass surface provides a flat interface to avoid distortion of the AFM laser beam from fluid movement. The cantilever is mounted on a metal disk that fits magnetically on top of the Z scanner in a similar way to imaging in air. The AFM fluid cell holds the cantilever in a position above the sample. Certain criteria are worth considering when choosing a liquid medium to measure cells with the AFM. For example, the liquid should not be too viscous, in order to avoid potential interferences with tip/sample interactions. The liquid should also be clear of particles that can build up on the sample surface or the tip and affect their proper interaction. Moreover, chemical and physical characteristics of the measurement medium should resemble as close as possible physiologic conditions of the native extracellular fluids. Phosphate saline buffer (PBS) is commonly available and is suitable as testing liquid-medium.

6.2.4.1. AFM Probe

It is crucial to select an appropriate probe for AFM elasticity/viscoelasticity measurements on cells, taking into account cantilever geometry, tip geometry, coating and spring constant. AFM consists of a microscale rectangular cantilever, typically made of silicon, with a sharp tip at its end with a tip radius of curvature on the order of 50-100 nm. This tip is actually in contact with the cell surface, while the cantilever serves as a soft spring to measure the contact force F. Because the spring constant k' of the cantilevers is much smaller than the intermolecular vibration spring constant of the atoms in the specimen, the cantilever can sense extremely small forces exerted by the individual sample atoms, which lead to a deflection of the cantilever d. Force is automatically calculated from the cantilever deflection measured with a laser beam and a photodiode $F = k' \cdot d$, while indentation is obtained from the difference between the displacement of the AFM sample stage and the movement of the cantilever tip caused by cantilever deflection.

All AFM experiments involved three lever contact cantilever CSC38 (Mikromasch, Estonia) made out of single crystal silicon. CSC38 is a chip with three cantilevers, but only the lever C with spring constant k'= 0.05 N/m and Cr-Au

coated probe tip with nominal radius of 35 nm was used for the experiments (Table 6.1.). The cantilever is made out of silicon with a material density of about 2330 kg/m^3 and Young's modulus of 169 GPa.

Table 0.1 Characteristics of the contact silicon cantilever CSC38 (cantilever C) provided by the manufacturer's data sheet.

Description	min	typical	max
Cantilever length, L ± 5 μm	-	300	-
Cantilever width, w ± 3 μm	-	32.5	-
Cantilever thickness, b ± 0.5 μm	-	1	-
Resonant frequency f, kHz	6	14	23
Spring constant, k', N/m	0.005	0.05	0.21

To extract the information about the mechanical properties of the cells from the measured data, one needs to know the cantilever spring constant and exact tip geometry. The optimum spring constant was chosen to be approximately equal to the effective spring constant of the cell. The CSC38 cantilever is coated on both sides with a thin layer of gold to increase reflectivity, because the laser intensity in cell culture medium it is attenuated. Information about the actual geometry of the tips used in this study was obtained through Field Emission Scanning Electron Microscope (FE-SEM) imaging using a Zeiss Sigma HDVP FE-SEM (Carl Zeiss, Cambridge, UK) (Figure 6.3.)

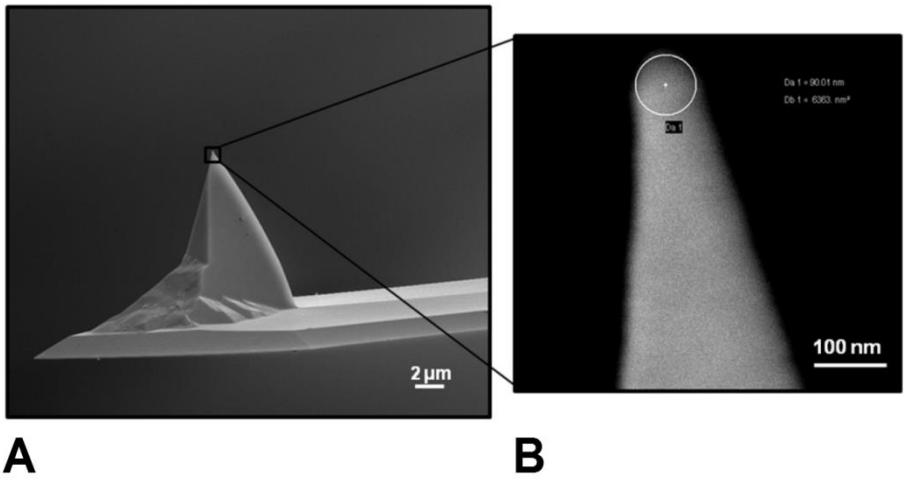

Figure 0.3 FE-SEM images of one of AFM CSC38 cantilevers used in this study: (A) side view image of the AFM tip. (B) Close-up of the region containing the spherical tip apex with a radius of 35 nm.

6.2.4.2. Spring constant calibration

The method used in AFM experiments is the resonant frequency in air method, also known as Sader's method (Sader et al. 1999). Besides that the cantilever should be rectangular, there are other limitations. The aspect ratio (L/w) should be in the range of 3-14 and the Q-factor >>1, but these requirements were fulfilled in this work. The method requires the length, width, resonant frequency and

quality factor (Q) of the cantilever and the density and viscosity of the fluid in which these are measured (typically air) to be known. As suggested by Sader (Sader et al. 1999) a small frequency is used for the determination of the Q-factor and the resonance frequency. Using an optical microscope Zeiss Axioskop 2MAT (Carl Zeiss Inc., Thornwood, NY, USA) with 20x magnification, the cantilevers length and width were determined. The measured cantilever width was 30.4±0.5 μm, while the length was 301.5±0.4 μm.

Before beginning any kind of procedures, the AFM controller, video monitors, computers and other major electronics were turned on and warmed up for at least 60–90 minutes to achieve a stable temperature and to minimize drift of electrical signals during the experiment. Starting from the specified resonant frequency range of the cantilever provided by the manufacturer, resonant frequencies of the CSC38 cantilevers used in this study were measured at different driving forces (30%-100%) in non-contact mode.

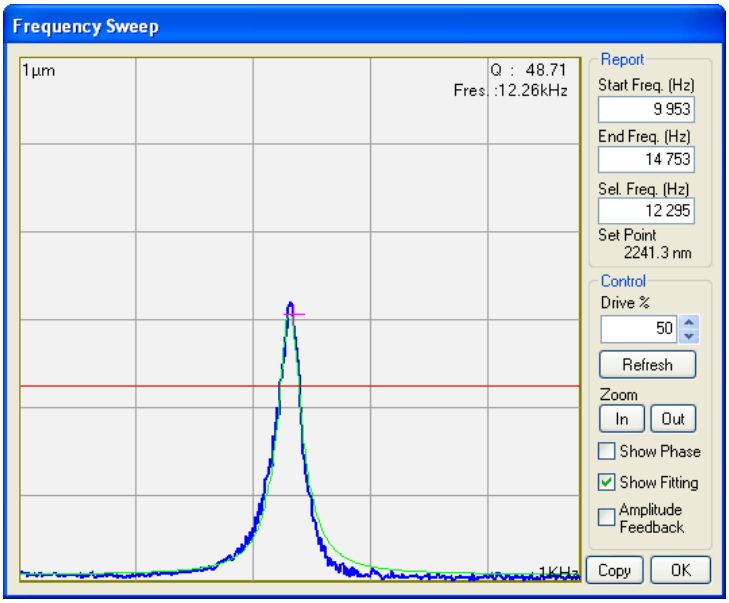

Figure 0.4 Resonant frequency sweep of the CSC38 type (vibration amplitude vs. frequency) at 50% driving amplitude of AC voltage signal.

The actual spring constant of the cantilever of each experiment was calculated from its resonant frequency (Figure 6.4). Using the Mathematica software, Q-factor, resonant frequency, the spring constant of the cantilevers were determined. The cantilevers used for the AFM measurements had a typical resonant frequency in the range of 12 to 16 kHz and a spring constant between 0.05 to 0.23 N/m. The spring constant of the cantilever determined experimentally for each cantilever was used in the input file for calculating the cantilever contact force.

6.2.5. Custom made analysis program

For nanoindentation data analysis, custom made LabVIEW (8.5.1, National Instruments, Austin, Texas) software was used. It collects the raw data, i.e. time,

Z_{scan} and force. This program was prepared to determine Young's modulus from the nanoindentation data by using the Hertz model (see chapter 3.5), including the cantilever spring constant determination and the calibration of the AFM tip radius. The program includes three analysis steps (Figure 6.5.): spring constant calibration, calculation of indenter radius and analysis of the Young's modulus. Each step includes reading the data from file, and selecting the area and the third point varies from selecting the calculated values for cantilever spring constant to calculation of Young's modulus. In AFM nanoindentation studies of hard materials (Florea et al. 2011), the stiff cantilevers were calibrated using reference materials, such as fused silica. However, in the case of cell AFM nanoindentation softer cantilevers are required. Therefore, in this study the spring constant calculation was done using Sader's method and the tip radius was extracted from FE-SEM imaging.

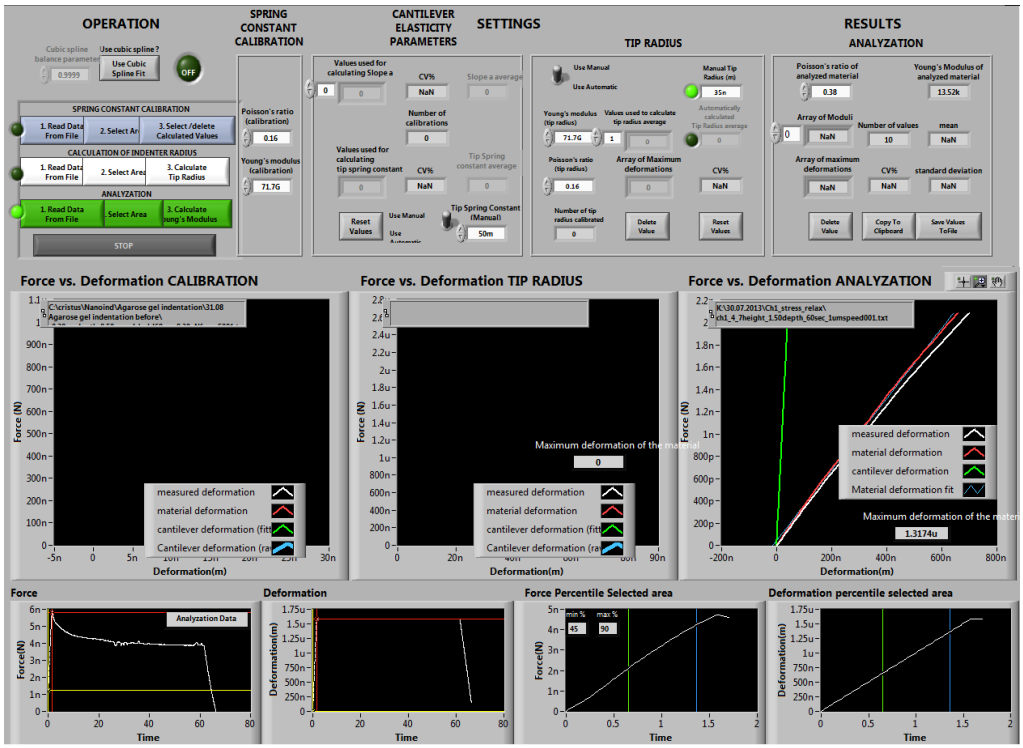

Figure 0.5 Graphical user interface of the LabVIEW based program for nanoindentation.

6.2.5.1. Calculation of Young's modulus of the agarose gels and chondrocytes using Hertz model

The raw deformation data for each measured sample includes both the material deformation under pressure and the cantilever elasticity. Therefore, the spring constant *k'* from the calibration is used to calculate the cantilever deformation *d* in the following manner:

$$d = \frac{F}{k'}, \qquad (0.1)$$

where F is the force value measured by the material indentation. The cantilever deformation can be then subtracted from the displacement of the piezoelectric scanner Z_{scan} :

$$\delta = Z_{scan} - d, \tag{0.2}$$

and the true material deformation δ can be calculated.

The Young's modulus E of the analyzed material is defined as:

$$E = \frac{3F(1-\nu^2)}{4\sqrt{R}\delta^{3/2}}, \tag{0.3}$$

where ν is Poisson's ratio and R the measured AFM tip radius.

The slope of the analyzed force-deformation curve K' is determined and further used to calculate the Young's modulus:

$$E = \frac{3(1-\nu^2)}{4\sqrt{R}K'\sqrt{\delta}}, \tag{0.4}$$

The most accurate method to determine E from a force indentation curve dataset is either by fitting the whole curve or only one portion. In this LabVIEW program, the elastic modulus of cells is calculated from the loading part of the stress-relaxation curve, mainly because the unloading part may be affected by large adhesion processes between the cell and AFM tip (Darling et al. 2006; Shinto et al. 2012). The area selection is performed by using the second derivative to find the local maximum and minimum values that indicates the contact point, maximum force point and the release point (Lin et al. 2007a).

6.2.6. AFM nanoindentation measurements for agarose gel

In order to assess the reproducibility of cell measurements using AFM nanoindentation, first a reference material agarose gel was used. Agarose gels are comparable in stiffness to single cells, however structurally and mechanically they are much simpler (Stolz et al. 2004). Agarose gels are linear copolymers that are commonly used in biochemical protocols such as gel electrophoresis and culture of microorganisms. The agarose gel fixed in the AFM open liquid cell was placed on the AFM stage and stabilized for about 15 minutes with the cantilever immersed in liquid. The agarose gels were imaged to find the location for the nanoindentation based on a previous imaging protocol (Florea et al. 2012) (Figure 6.7).

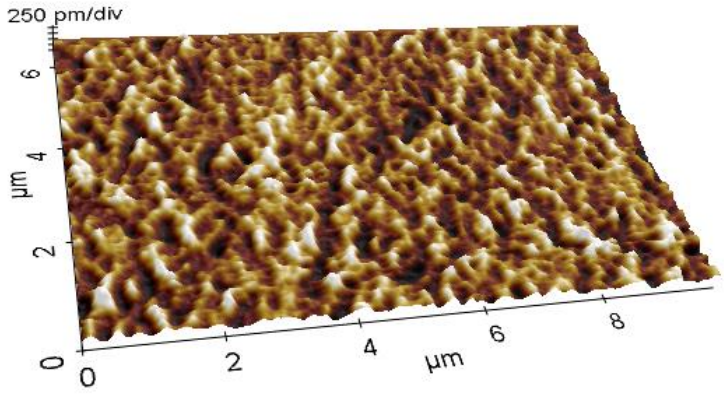

Figure 0.6 3D image of agarose gel acquired in AFM contact-mode.

The stress-relaxation experiments on agarose gels were carried out in deionized water using following nanoindentation parameters: indentation depth 1 µm, which is well below Buckle's indentation depth limit (i.e. 10% of specimen thickness (Bückle 1971)), 0.50 µm/s displacement rate, 60 seconds relaxation time and 0.30 nN setpoint force. Tests were performed at ambient temperature (25^0C) and at atmospheric pressure. Stress-relaxation curves were acquired using a relative low velocity of the Z scanner, which reduces the influence of hydrodynamic drag exerted by the liquid. All stress-relaxation curves were acquired in displacement control mode and the force was recorded in time. The AFM photodiode was calibrated by recording three stress-relaxation curves in the bare region of the Petri dish using a constant indentation of 1 µm (approx. $F \sim 3$ nN). Ten stress-relaxation curves were recorded (2048 data points) from three different regions of each agarose gel (6 samples) and averaged. Agarose gel measurements were performed in order to choose the most suitable measurement parameters to be used for the cell nanoindentation.

In the Hertz model, the Poisson's ratio for agarose gel was assumed to be 0.4. Other authors (Park et al. 2005; Stolz et al. 2004) have used the value 0.5 instead, which is usually applied to soft biomaterials. The reason of choosing a value of 0.4 is based on the assumption that despite the high water content similar to biomaterials, wet agarose gels are not incompressible. In fact, agarose gel forms a porous matrix that can be squeezed by the AFM tip like a sponge, as the filling water is not bonded to the matrix at molecular scale.

6.2.7. AFM nanoindentation measurements for chondrocytes

After removal of chondrocytes from the incubator, the cells were allowed to equilibrate at ambient environment for around 15 minutes before AFM measurements. Prior to moving the cells onto the stage of the AFM, standard cell

culture medium was removed and replaced with a minimal volume of PBS (2–3 mL PBS in a 60 mm Petri dish). Chondrocytes seeded on the Petri dish were visualised using the AFM optical microscope (Figure 6.7). To minimize the possible damage of the chondrocyte membrane and contamination of the AFM probe, the cells were not scanned before the AFM nanoindentation experiments.

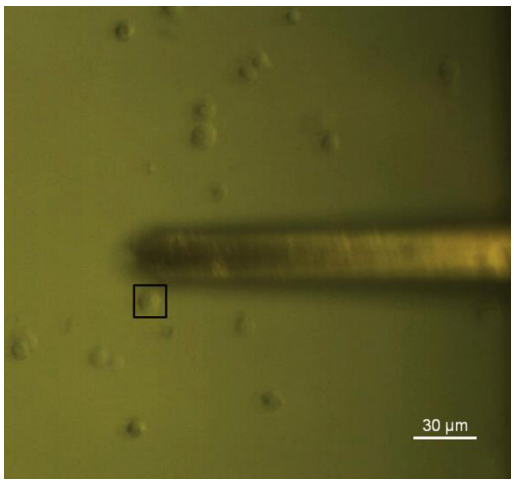

Figure 0.7 Captured optical microscope image of chondrocytes seeded on a Petri dish.

The AFM nanoindentation of the living cells in liquid medium is described as follows. The laser beam needs to be aligned in the air. If the laser spot cannot be seen in the laser reflection window, the laser beam's location is too far from the cantilever. After the laser beam was aligned, the AFM tip was lowered using the stepper motor to make contact with the surface of the cell culture medium. The height of the liquid should be high enough to immerse the cantilever. Furthermore, the laser reflection has to be centered on the photodetector and its position monitored for several minutes, as it will tend to drift until the probe and fluid become thermally equilibrated. Lowering the cantilever into the liquid will cause the laser spot to move towards the end of the cantilever and the laser intensity will drop. Therefore, the laser spot has to be readjusted by turning gently the laser aiming screw to move the laser spot back to free end of the cantilever. Additionally, the laser intensity can be increased turning a small screwdriver into the AFM head eyelet.

Stress-relaxation tests on chondrocytes were carried out over the central region of the single rounded chondrocytes under optical control with a constant approach velocity of 0.50 µm/s and 60 seconds relaxation time. The approach and retraction velocity of the probe is an important parameter for AFM data acquisition since cells appear stiffer at higher velocities. At velocities greater than 10 µm/s, the speed-dependent hydrodynamic force acting on the cantilever increases the apparent forces considerably (Janovjak et al. 2005). Furthermore, chondrocytes behave in a viscoelastic manner, which means that energy is dissipated into the cell when they are indented by the AFM tip (hysteresis in the force–deformation curve). This hysteresis is minimized at probe velocities under 1 µm/s (Ng et al. 2007). The cantilever was held at a constant displacement for the stress-relaxation tests. As a

control experiment, two indentation curves were obtained from the plastic before taking measurements from the cells to make sure of the linear increase in force on a hard substrate as a function of the z-piezo displacement. The tip approaching protocol of the AFM sensed the sample surface by making the tip contact the sample until a small contact force (set point) of about 0.10 nN was reached. To determine the height of cells, the contact points of these two indentations were used to define the reference z-position of the underlying surface. The height of each chondrocyte was calculated by subtracting from this z-reference the cantilever's z-position at the moment of contact with the cell surface. Note that only the round chondrocytes were chosen for the AFM measurements and the average height of the normal chondrocytes (n=12) was 8.2±3.1 μm and for the Cytochalasin D treated ones (n=13) it was 7.4±2 μm. Cellular deformation along the direction of the force is generally defined as a relative reduction in height, that is $\Delta H=H/H_0-1$, where H is the deformed height, H_0 the initial height and the result is expressed in percentage (Caille et al. 2002).

In this study, the normal and treated chondrocytes were probed at three different strain levels (5%, 10% and 15% deformation relative to the cell height) equivalent on average with an indentation depth of 400 nm, 800 nm and 1.2 μm, respectively. The cells were probed five times consecutively with a 30 seconds rest between indentations under three increasing levels of strain for a total of 15 indentations per cell. The Young's modulus analysis (Equation (6.5)) was carried out for a total of 180 and 195 stress-relaxation curves using custom made LabVIEW program on 12 normal and 13 treated chondrocytes, respectively. The Poisson's ratio ν, was assumed to be 0.38, based on the previous studies on chondrocytes (Darling et al. 2006; Trickey et al. 2006).

6.2.8. FE modelling and analysis

When studying AFM nanoindentation of chondrocytes, the application of Hertz model is questionable. In fact, the key assumptions of the Hertz theory are that the cell is homogenous, isotropic, linear elastic half-space subject to infinitesimally small strains. Moreover, in most of the cases, it is assumed that the material of the cell is incompressible. However, most cells are heterogeneous, anisotropic with intracellular components (cytoskeleton, nucleus, cytoplasm and several other organelles) and exhibit non-linear behavior. Conventional biomechanical modeling, as previously described, is based on analytical models that solve the differential equations of boundary value problems. Both elastic and viscoelastic models have been used for quantifying mechanical properties of chondrocytes in AFM nanoindentation (Chahine et al. 2013; Darling et al. 2006; Darling et al. 2008; Ng et al. 2007). These analytical models have the advantage of being easily applicable, but suffer from significant drawbacks such as approximations in modeling geometrical and force boundary conditions and difficulties in applying complex material models. It was also generally assumed in these models that the strain generated during compression is small that the linear elastic and viscoelastic models could be applied. Moreover, if a chondrocyte is compressed to large deformations, large strains (i.e. 5% or more) might be generated. Thus, a non-linear elastic/viscoelastic model should be preferred instead. Finite element (FE) modeling was essentially developed for the field of structural engineering, but was later applied to describe the behavior of solids and fluids.

Recently, FE modeling has been widely adopted in the modeling of biological tissue testing. FE model has the advantage of being able to model accurate geometry and boundary conditions of the tissue and being flexible in applying complex material constitutive models. The Neo-Hookean material model (Rivlin 1949) has been used successfully to describe non-linear elastic behavior of cells in compression experiments. In this study, the AFM experimental stress-relaxation curves in combination with FE analysis and optimization algorithms were used to describe the mechanical behavior of chondrocytes by means of hyperelastic constitutive relationships and consequently the poroelastic, viscoelastic and poroviscoelastic properties of chondrocytes were determined.

Nanoindentation of the chondrocytes with a conical/spherical indenter was modeled using the commercial FE analysis software Abaqus (Dassault Systèmes, Providence, USA). The cell was modeled as a layer bonded to a rigid and impermeable substrate being indented by a rigid and impermeable indenter (Figure 6.6.).

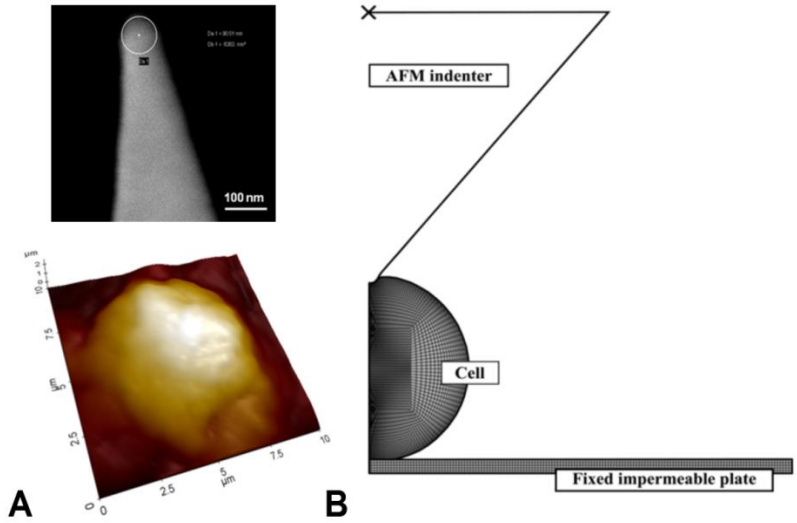

Figure 0.8 (A) The experimental AFM tip and 3D image of chondrocyte acquired in AFM contact-mode. (B) The axisymmetric FE model of a chondrocyte on the rigid substrate.

The cell thickness was set to 8 μm based on the average thickness determined from AFM experiments. The indenter tip radius of 35 nm and full-cone angle of 40° was obtained from the experimentally used tip (FE-SEM images). Symmetric boundary condition was implemented along the axis of symmetry and the base of the cell was fixed. The contact between the indenter and cell was assumed frictionless. The model consisted of 3400 axisymmetric elements. A higher mesh density was used in regions of high stress (near the indenter tip edge). Mesh convergence studies were performed to ensure that the solution was independent of the finite element mesh size used in the models. A compression step of 5% of the cell thickness followed by 60 seconds relaxation period was applied on the cell surface, similarly as done in the experiments.

Non-linear behavior of the chondrocyte was described by Neo-Hookean hyperelastic model (Equation (2.8)), whereas the time-dependent deformation behavior was modeled using fluid flow-dependent viscoelastic (i.e. poroelastic), fluid flow-independent viscoelastic and combination of those two (i.e. poroviscoelastic) material models. This led to three material models for the chondrocyte: hyperporoelastic, hyperviscoelastic and hyperporoviscoelastic. The cell was modeled with 4 node axisymmetric quadrilateral elements of type CAX4 (non-porous elements for viscoelastic model) and CAX4P (porous elements for poroelastic and poroviscoelastic models). In the hyperporoelastic model, the chondrocyte was modeled as a porous solid phase filled with an intracellular fluid. The model was characterized by the equilibrium elastic modulus *E*, Poisson's ratio (ν=0.3) and permeability *k*, describing the fluid flow velocity. In the hyperviscoelastic model, in addition to *E* and ν, the shear relaxation modulus g_1 and relaxation time τ_1 were defined by time-domain Prony series (Equation (2.12)). The hyperporoviscoelastic model included all the aforementioned material parameters. Furthermore, fluid flow through the cell membrane was first allowed and then prevented in the hyperporoviscoelastic model. The pore pressure along the cell surface was set to zero to simulate the free draining of intracellular fluid through the cell membrane. Non-linear permeability was not considered in this study and the initial void ratio e_0 was assumed to be 2.3.

In order to obtain unique material parameters for different material models (hyperporoelastic, hyperviscoelastic, hyperporoviscoelastic), the mean squared error (MSE) between the experimental and simulated stress-relaxation data was minimized using a multidimensional unconstrained nonlinear minimization routine (fminsearch) available in Matlab R2007b (MathWorks Inc., Natick, MA, USA).

MSE is defined as follows:

$$MSE = \frac{1}{n}\sum_{i=1}^{n}\left(F_{model_i} - F_{exp_i}\right)^2, \qquad (0.5)$$

where n corresponds to the number of sampling points, F_{model_i} and F_{exp_i} are values of the reaction forces predicted by the FE model and measured in the AFM experiments, respectively. In the optimization, the material parameters of the material models were iteratively refined in Abaqus until the convergence criterion in Matlab was satisfied ($1x10^{-6}$). This algorithm requires the specification of initial values for the parameters to be optimized. In order to speed up the optimization, the initial values were retrieved by a parametric study. The Poisson's ratio was kept constant in all optimizations (ν =0.3). The optimized material parameters for the hyperporoelastic model were E, k, for the hyperviscoelastic model they were E, g_1, τ_1 and the optimized parameters for the hyperporoviscoelastic models were E, k, g_1, τ_1.

6.2.9. Statistical analysis

The stress-relaxation curves of 12 normal and 13 Cytochalasin D treated chondrocytes were assessed. The elastic modulus of the cells is reported as mean ± standard deviation (SD). Paired Student's t-test was performed to determine whether significant differences existed between the mechanical properties of normal chondrocytes at different levels of deformation and as well in the treated ones. Also,

the unpaired Student's t-test was used to assess the significance of differences between the normal and treated cell groups.

6.3. Results

6.3.1. Agarose gel elastic properties

Using the AFM based nanoindentation and custom made LabVIEW program, mean Young's modulus of the agarose gel was 29.08±2.0 kPa. Young's modulus values were essentially independent of indentation depth (i.e. linear elastic) and time (Figure 6.9.). Reproducibility of the measurements as indicated by the coefficient of variation (i.e ratio of standard deviation and mean) CV (%) was 7.18%.

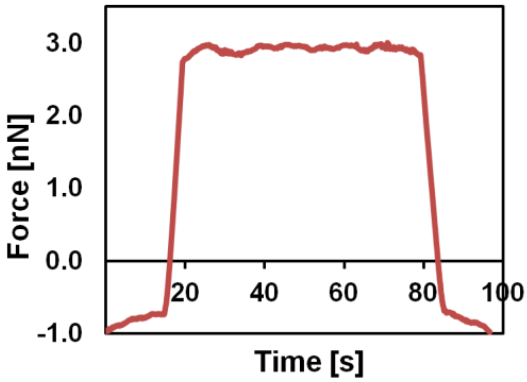

Figure 0.9 Stress-relaxation curve for agarose gel.

Other studies reported a similar elastic modulus of 26.3±4.2 kPa for 3% agarose gel obtained with an AFM pyramid tip (Costa et al. 2003). Moreover, when probed with AFM microsphere tips the agarose gels exhibited a similar elastic modulus of 28.1±6.7 kPa.

6.3.2. Local elastic properties of normal and treated condrocytes

Normal chondrocytes exhibit distinct local mechanical properties at increasing levels of deformation. The cell elastic modulus was statistically significantly higher at 5% deformation compared to the elastic modulus determined at 10% and 15% deformation ($p<0.005$). In fact, the elastic modulus decreased with increasing level of cell deformation. However, no significant differences between cell elastic modulus were found at 10% and 15% deformation ($p>0.005$). The applications of the Hertz model result in decreasing values for the elastic modulus for increasing amounts of cell deformation and are summarized in Table 6.2.

Table 0.2 Elastic modulus for bovine chondrocytes and chondrocytes treated with Cytochalasin D, all determined for 5%, 10% and 15% strain.

Deformation relative to the cell height	5%	10%	15%
Cell groups	$E_{elastic}$ (kPa), mean±SD		
Normal chondrocytes (n=12)	28.1±11.9*,**	23.3±10.6	21.9±10.2
Treated chondrocytes with Cytochalasin D (n=13)	16.9±8.3	15.7±10.3	15.3±7.7

* values are statistically significantly different from the 10% and 15% strain level ($p<0.05$)
** values are statistically significantly different from the Cytochalasin D treated chondrocyte group ($p<0.05$).

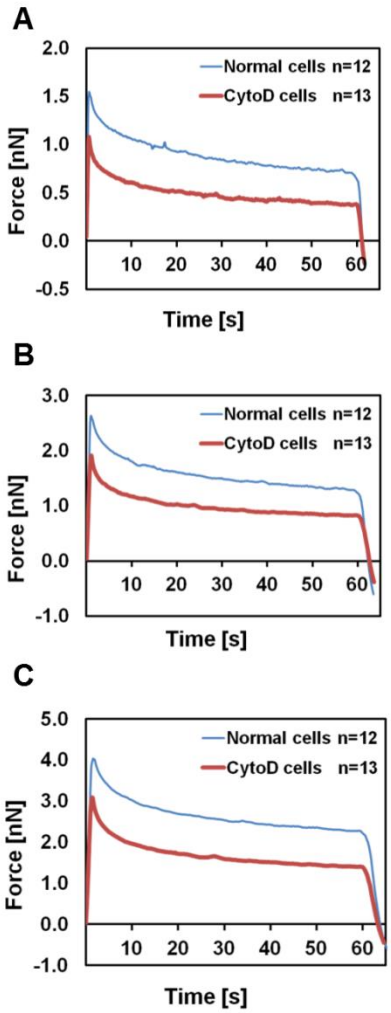

Figure 0.10 Mean stress-relaxation response curves on normal vs. Cytochalasin D (Cyto D) treated chondrocytes at 5% (A), 10% (B) and 15% (C) strain relative to the cell height.

Interestingly, after disrupting the cell actin cytoskeleton using Cytochalasin D, a significant difference (p<0.05) was observed between the elastic modulus of untreated and treated cells at 5% strain (Figure 6.10, Table 6.2). In fact, the elastic modulus in the treated cells yielded relatively constant values across all different strains.

6.3.3. FE analysis and simulation of the stress-relaxation curves on normal and treated chondrocytes

In the experimental AFM stress-relaxation curves obtained from normal chondrocytes, the peak force decreased sharply within several seconds and the nonlinear decay of loading force continued gradually over the remainder of the measurement time. The hyperporoelastic model underestimated the peak force of the AFM nanoindentation experiment, whereas it overestimated the experimental relaxation part (Figure 6.11).

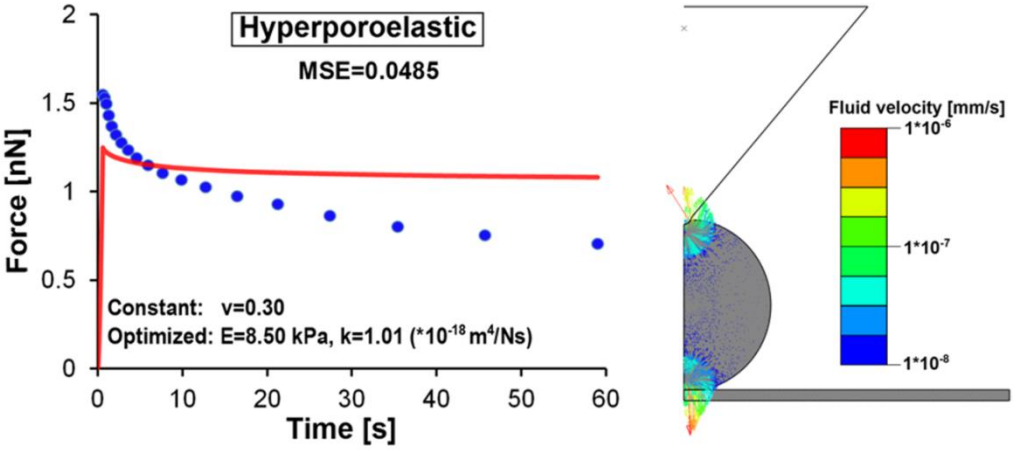

Figure 0.11 Comparison of experimental AFM force-relaxation curve (blue circles, mean, n=12) and optimized model prediction (red line) using a hyperporoelastic FE model on normal cells. Fluid flow through the cell membrane and internal fluid flow is shown on the right subfigure.

The hyperviscoelastic model was able to capture the experimentally observed peak force and it followed also nicely the experimental relaxation behavior of cells (Figure 6.12).

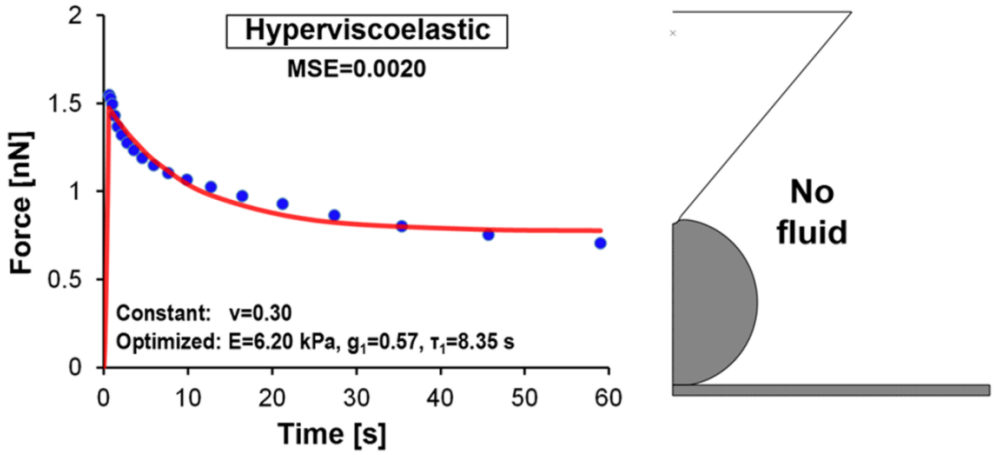

Figure 0.12 Comparison of experimental AFM force-relaxation curve (blue circles, mean, n=12) and optimized model prediction (red line) using a hyperviscoelastic FE model on normal cells. There is no fluid flow in this model.

Both hyperporoviscoelastic models with and without fluid flow through the cell membrane captured best the entire stress-relaxation behavior of chondrocytes observed experimentally (Figure 6.13, 6.14), smallest difference (MSE = 0.0010) between the experimental curve and model prediction being in the model with closed cell membrane to fluid flow. The permeability of chondrocytes was found to range from 1.01×10^{-18}- 0.41×10^{-15} m^4/Ns for different models.

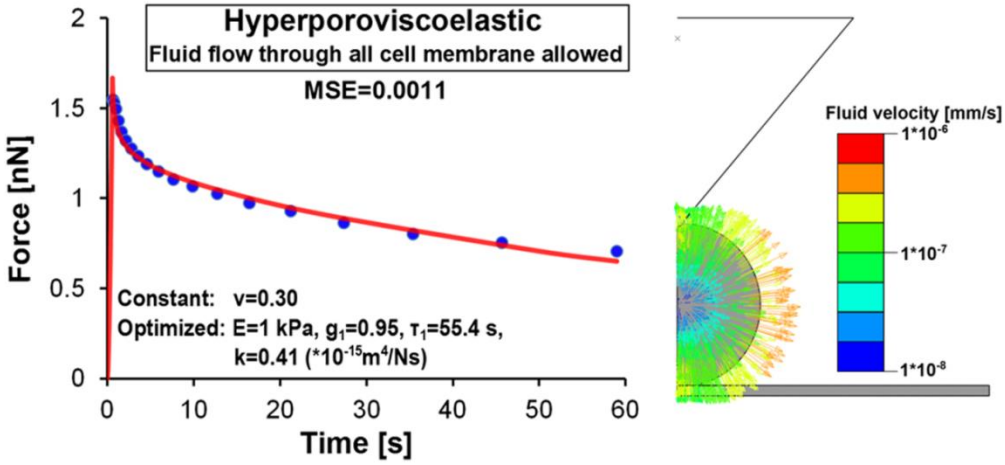

Figure 0.13 Comparison of experimental AFM force-relaxation curve (blue circles, mean, n=12) and optimized model prediction (red line) using a hyperporoviscoelastic FE model on normal cells. Fluid flow through the cell membrane is allowed.

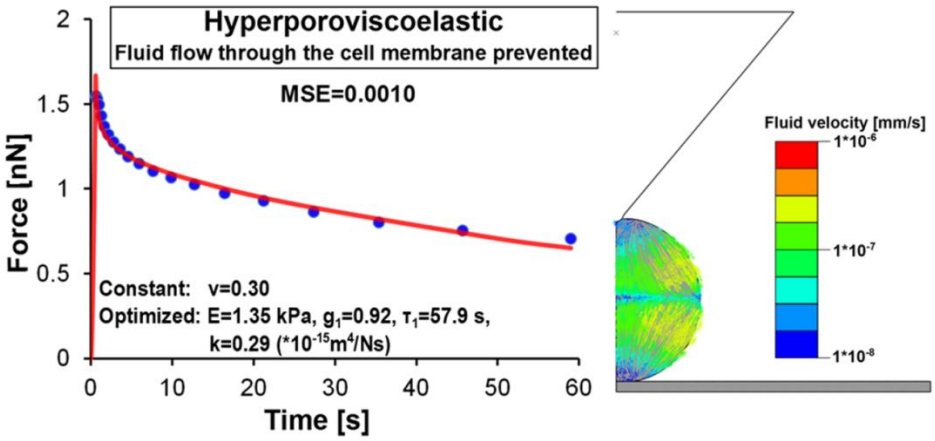

Figure 0.14 Comparison of experimental AFM force-relaxation curve (blue circles, mean, n=12) and optimized model prediction (red line) using a hyperporoviscoelastic FE model on normal cells. Fluid flow through the cell membrane is prevented.

In the experimental AFM stress-relaxation curves obtained from the treated chondrocytes with Cytochalasin D, the peak force decreased sharply within several seconds and the nonlinear decay of loading force continued gradually over the remainder of the measurement. This response is similar to the stress-relaxation of normal chondrocytes, however especially the values for the elastic modulus decreased significantly in all models. The hyperporoelastic model in treated cells underestimated the peak force of the AFM nanoindentation experiment, while it overestimated the experimental relaxation part (Figure 6.15). In treated cells, the elastic modulus considerably decreased from 8.50 kPa to 6.38 kPa, however the permeability remained the same.

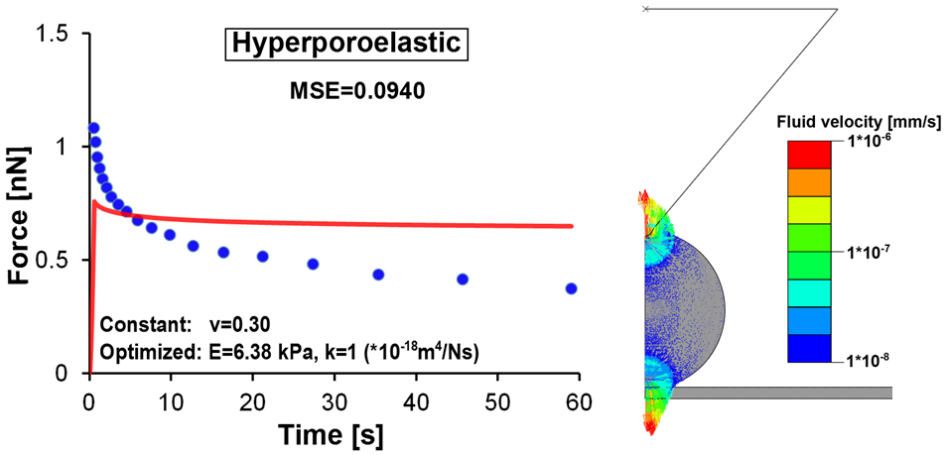

Figure 0.15 Comparison of experimental AFM force-relaxation curve (blue circles, mean, n=13) and optimized model prediction (red line) using a hyperporoelastic FE model on treated cells. Fluid flow through the cell membrane and internal fluid flow is shown on the right subfigure.

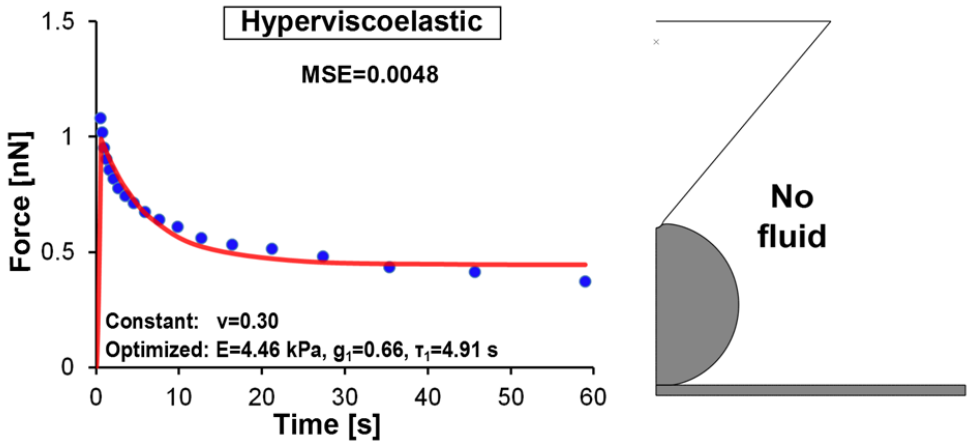

Figure 0.16 Comparison of experimental AFM force-relaxation curve (blue circles, mean, n=13) and optimized model prediction (red line) using a hyperviscoelastic FE model on treated cells. There is no fluid flow in this model.

The hyperviscoelastic model applied for the treated cells underestimated the experimentally observed peak force and followed nicely the experimental relaxation behavior of cells (Figure 6.16). Again, the elastic modulus considerably decreased from 6.20 kPa in the normal cells to 4.86 kPa in the treated ones. Relaxation time was also reduced substantially.

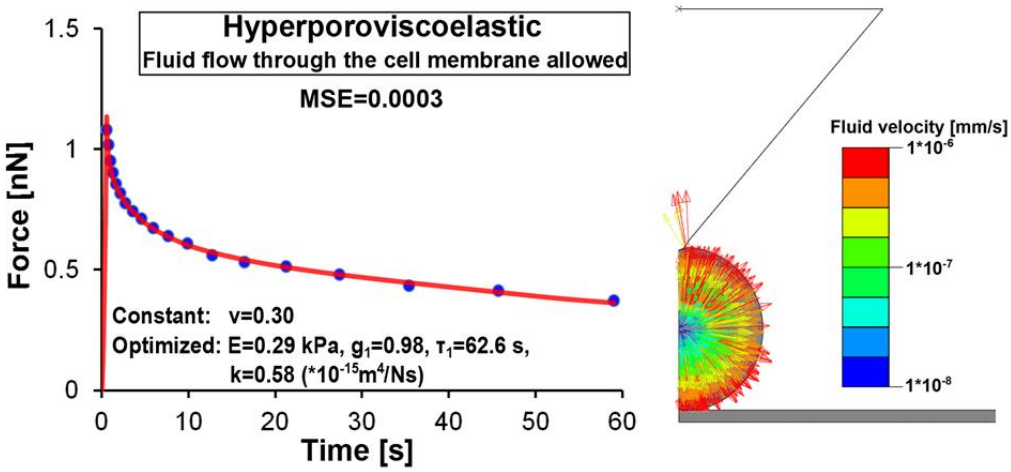

Figure 0.17 Comparison of experimental AFM force-relaxation curve (blue circles, mean, n=13) and optimized model prediction (red line) using a hyperporoviscoelastic FE model on treated cells. Fluid flow through the cell membrane is allowed.

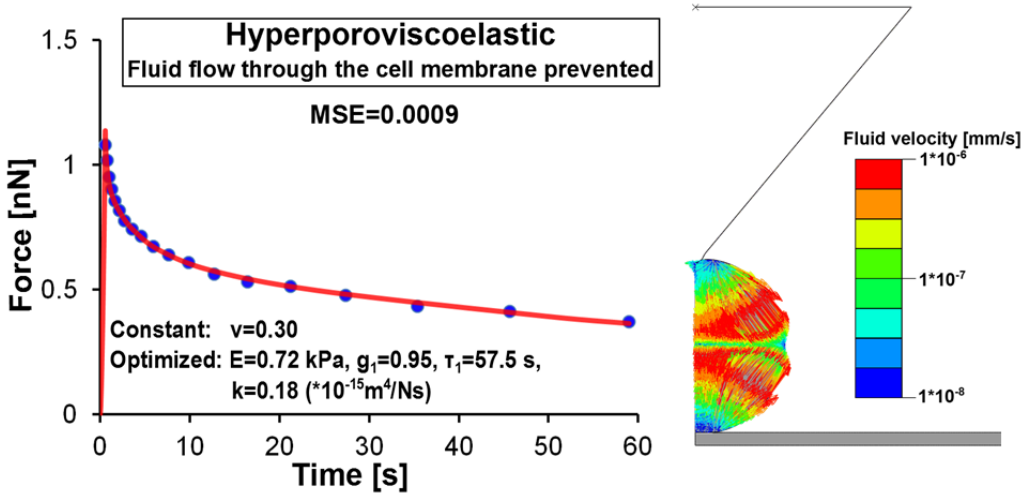

Figure 0.18 Comparison of experimental AFM force-relaxation curve (blue circles, mean, n=13) and optimized model prediction (red line) using a hyperporoviscoelastic FE model on treated cells. Fluid flow through the cell membrane is prevented.

For the treated cells, both hyperporoviscoelastic models with and without fluid flow through the cell membrane captured best the entire stress-relaxation behavior of treated chondrocytes observed experimentally (Figure 6.17, 6.18), smallest difference (MSE = 0.0003) between the experimental curve and model prediction being in this case in the model with fluid flow through the cell membrane allowed. The elastic modulus in the hyperporoviscoelastic model with fluid flow through the cell membrane allowed considerably decreased from 1 kPa in the normal cells to 0.29 kPa in the treated ones, while in the hyperporoviscoelastic model with fluid flow through the cell membrane prevented it decreased from 1.35 kPa to 0.72 kPa. Viscoelastic relaxation parameters and permeability did not change substantially.

6.4. Discussion

First, in this study we evaluated and optimized the operational parameters in AFM nanoindentation measurements using 2.5% agarose gel. The results showed that the mechanical response of agarose gels under AFM nanoindentation using nanosized probe was mainly elastic. There was no time-dependent response observed during the hold portion. The agarose gels give important insight into cell mechanical properties estimation, because of their near similar stiffness and serve as an excellent model system to optimize the AFM experimental protocols. Our findings are consistent with previous AFM nanoindentation studies on agarose gels. The reported elastic modulus for agarose gels falls in the range between 10-50kPa, depending on the concentration of the gel and the size of the AFM probe (Costa et al. 2003; Nitta et al. 2000; Stolz et al. 2004; Tripathy and Berger 2009). The small variation in the elastic properties of agarose gels from our study demonstrates that

AFM is a reliable method for quantifying local mechanical properties of soft materials.

Another aim of the study was to quantify the local elastic and viscoelastic properties of normal chondrocytes under AFM nanoindentation. The local elastic properties of cells were examined at three increasing levels of strain (i.e. 5%, 10% and 15% of the cell thickness). For a quantitative evaluation of the cell elasticity, the loading part of the stress-relaxation curve was analyzed using Hertz model. The main finding was that the Young's modulus calculated for a small cell strain level (5% of the cell thickness) was greater, whereas for larger cell strain levels (10% and 15% of the cell thickness) it decreased nonlinearly. This could be explained by the fact that at small AFM indentations, the elastic behavior of chondrocytes is dominated by the combined effects of mechanical properties of the membrane and the underlying actin filaments of the cytoskeleton (Pogoda et al. 2012). As the deformation is increased, the overall stiffness of the whole cell is obtained and other intracellular components are involved. So far, there is only one AFM study that systematically examined the non-linear elastic and viscoelastic responses in chondrocytes (Chahine et al. 2013). Chahine et al. (2013) used a "pointwise" calculation of the elastic modulus as a function of indentation depth and found that the apparent elastic modulus of chondrocytes decreased (from ~3.5 kPa to ~ 0.55 kPa) with increased indentation depth (15 nm-2 μm). This method in analyzing AFM nanoindentation data (Costa et al. 2006), accounting for the AFM indenter geometry to compute an apparent elastic modulus as a function of indentation depth require no a priori assumptions about the linearity of cell material properties. Although, the trends observed in our study are similar to the abovementioned study, the values of Young's modulus at different levels of strain are higher. Moreover, the Young's modulus of chondrocytes in AFM nanoindentation reported in the previous studies (Darling et al. 2006; Ng et al. 2007) is lower than the Young's modulus of chondrocytes obtained in the present work. However, no direct comparison should be made since the abovementioned studies used AFM microsized spherical probes to measure the bulk elastic properties of the chondrocytes by applying a mechanical stress to the whole cell. The microsized spherical probe can indent several cytoskeletal elements simultaneously because of its large contact area. Thus, the well-organized cytoskeleton network may share and dissipate the force arising from the nanoindentation, diminishing its effect. Various studies (Carl and Schillers 2008; Harris and Charras 2011; Rico et al. 2005; Vargas-Pinto et al. 2013) reported that the AFM nanoindentation measurements on living cells using nanosized probes give higher estimates of cellular Young's modulus than those using microsized spherical probes. For instance, Dimitriadis et al. (2002) (Dimitriadis et al. 2002) found that AFM nanosized probes overestimated Young's modulus when compared to that found with a microsized probe by 60%. Korhonen et al. (2002) showed that the tissue level indentation gives higher values than unconfined (bulk) measurements and smaller indenter probes yield higher values of elastic modulus. It is therefore reasonable that relatively high values of Young's modulus of the chondrocytes were obtained in the present study. However, it should be noted that the modulus values reduced substantially when using the FE model.

It has been reported that the Young's modulus for chondrocyte during compression is in the range of 0.6-27 kPa using different local and global mechanical testing techniques, such as micropipette aspiration (Guilak 2000; Jones et al. 1999; Trickey et al. 2000), AFM (Chahine et al. 2013; Darling et al. 2006; Darling et al. 2008; Ng et al. 2007), cytoindentation (Koay et al. 2003)and unconfined cytocompression (Leipzig and Athanasiou 2005; Ofek et al. 2009a;

Shieh and Athanasiou 2006). It must be also noted that the elasticity data obtained by different local and global testing techniques on the same type of cell will represent the mechanical responses of different aspects of the cell structure (Bader et al. 2002). Thus, our findings are in general in agreement with the previous studies. Several factors could account for this discrepancy in moduli, such as constitutive cell model used, geometric assumptions, biological variability, the source of the tested chondrocytes and degree of cellular attachment. Differences might be also attributed to different loading conditions. For instance, the imposed forces in micropipette aspiration studies reach a maximum of ~75 nN compared to at least 4 nN in the present study.

Unlike traditional engineering materials, chondrocytes within the same population vary greatly in their mechanical properties. Although, chondrocytes within the same population may have similar structural and morphological properties, a single cell is spatially variable due to its inhomogeneous subcellular structure. In order to minimize the data bias due to reorganization of the subcellular structures in response to the indentation stress, five consecutive stress-relaxation curves were obtained from the same area of the cell. Previous study (Darling et al. 2006) demonstrated significant variations in the mechanical properties of chondrocytes from different zones of cartilage. Specifically, chondrocytes from the superficial zone were significantly stiffer than those from middle/deep zone. The fact that the chondrocytes used in this study were isolated from the full thickness articular cartilage may also add a degree of variability. The experimental variability, as evidenced by large standard deviations in the elastic properties of cells was partly due to cellular structural inhomogeneity, but also may resulted from zonal variation in cellular mechanical properties in cartilage.

Another aim of the present study was to examine the contribution of actin cytoskeleton to the mechanical properties of single chondrocytes over a range of applied indentation strains. To specifically address its role to the local elastic response of the chondrocytes, we used Cytochalasin D, a fungal agent as an inhibitor of polymerization of actin cytoskeleton. Indeed, the stress-relaxation curves showed that the forces were smaller after disrupting the actin cytoskeleton in chondrocytes, which led to a noticeable decrease of the Young's modulus. On the other hand, the Young's modulus remained almost constant at all indentation strain levels. These findings suggest that the presence of actin cytoskeleton in the cell cortex is the primary cause to the nonlinear elastic mechanical cell response to indentation. By disrupting actin filaments with Cytochalasin D or intermediate filaments with acrylamide, Chahine et al. (2013) found that the elastic modulus and viscosity of the articular chondrocyte decline dramatically. In contrast to our results, they found that disruption of actin cytoskeleton at small indentation depths did not affect chondrocyte elastic properties. The elastic modulus was significantly reduced only at greater indentation depths. This discrepancy may be explained by the use of a nanosized AFM probe in our study, which is more sensitive to very local properties of the cell. Elucidating the role of the actin cytoskeleton in the mechanical characteristics of single cells may have important implications toward understanding cellular mechanobiology, as well as structure-function relationships of chondrocytes in health and disease. Additionally, disruption of other cytoskeletal components such as microtubules and intermediate filaments using relevant fungal agents would provide a better understanding of the roles of each of these components to the local viscoelastic properties of chondrocytes.

Furthemore, the calculation of the elastic modulus in the previous AFM nanoindentation cell studies was mainly based on the Hertzian model for analyzing

the contact mechanics (Kuznetsova et al. 2007). However, the force-time curves measured in the present study demonstrate that the chondrocytes undergo a time-dependent behavior in response to a constant deformation (i.e. stress-relaxation). Therefore, chondrocytes are more properly described as viscoelastic.
The present study proposes a combined approach of experimental measurements, FE analysis and optimizations algorithms to analyze the AFM stress-relaxation curves. The AFM nanoindentation process was simulated for three different constitutive behaviors of the chondrocytes: hyperporoelasticity, hyperviscoelasticity and hyperporoviscoelasticity.

The hyperporoviscoelastic model was able to capture best the mechanical behavior of the chondrocyte suggesting that the time-dependent behavior of chondrocytes is resulted primarily by the combined effects from fluid-flow-dependent poroelasticity and flow-independent viscoelastic processes. However, fluid flow through the cell membrane caused only a minor change in the stress-relaxation behavior of the cell. In fact, the best match between the experiments and model prediction was obtained when there was no fluid flow allowed through the normal cell membrane. During AFM stress-relaxation experiments, the rapid stress application on the cell causes a sudden increase in the local stress and fluid pressure starts to build up inside the chondrocyte. Over time, the intracellular fluid in the compressed area redistributes inside the cell and the pore pressure dissipates. Cellular deformation resulting from the local application of force propagates through the viscoelastic cytoskeleton network and at equilibrium the applied force is entirely balanced by cellular viscoelasticity. This suggests that intracellular fluid flow, redistributing stresses and fluid pressures during nanoindentation together with fluid-flow independent viscoelasticity, rather than fluid flow out of the cell are major determinants for the viscoelastic, time-dependent behavior of chondrocytes.

Recently, an AFM study (Moeendarbary et al. 2013) testing epithelial and cancerous cells proposed that the cells behave as a poroelastic material and the water redistribution through the solid phase of the cytoplasm is the main source of viscoelastic dissipation at short timescales. Moreover, a theoretical study (Atheshian et al., 2007) demonstrated that under mechanical loading the intracellular fluid from a single chondrocytes may take several days to exude. These studies further support our current findings that over relatively short time scales, which is on the order of seconds in the AFM stress-relaxation experiments in the present study, the intracellular fluid has no time to flow out of the cell. This study demonstrates for the first time intracellular flow-dependent and -independent mechanisms, which primarily control the time-dependent mechanical behavior of chondrocytes under AFM nanoindentation. This provides an important step towards understanding the cellular mechanisms modulating cartilage mechanotransduction.

Although, there are no previous reports on chondrocyte permeability values in AFM nanoindentation, the optimized values of elastic modulus and permeability of the chondrocyte obtained from hyperporoviscoelastic and hyperporoelastic model were generally in good agreement with the literature values. Previous computational studies of chondrocytes (Ateshian et al. 2007; Chahine et al. 2007) used a Young's modulus of 1 kPa and a permeability of 5×10^{-15} m^4/Ns close to that of the cartilage extracellular matrix, consistent to our findings (E = 1-1.35 kPa; k = 0.29×10^{-15} m^4/Ns-0.41×10^{-15} m^4/Ns). Leipzig et al. (2005) used a linear biphasic model (Mow et al. 1980) to analyze the data from unconfined compression, to describe interstitial fluid flow-dependent viscoelastic responses of chondrocytes and obtained an aggregate modulus of 2.6±0.8 kPa. The results also showed that the

chondrocytes had a permeability of $2.57\pm3x10^{-12}$ m^4/Ns much higher than that in the present study. This high variation in the values exist most likely due to different experimental techniques and theoretical models applied in the different studies.

Furthermore, the treatment of chondrocytes with cytochalasin D resulted in a marked decrease of their elastic modulus obtained using FE modeling compared to the normal ones, however no substantial change was seen in the viscoelastic relaxation properties and permeability. These results indicate that the actin filaments have a predominat effect on the local elastic properties of chondrocytes, rather than on viscoelastic properties under small deformation.

In this study, only the experimental stress-relaxation curves at 5% strain were analyzed using the FE analysis and optimization algorithms. In future studies, the stress-relaxation curves at 10% and 15% strain will be modeled using the same approach as previously described. Another limitation of the FE model was that the cell membrane was not modeled as a separate layer, due to its negligible thickness (on the order of 10 nm).

Taken together, the AFM nanoindentation and finite-element modelling with nonlinear poroviscoelastic material models can be used to accurate identify biomechanical properties of single chondrocytes, providing also a framework to future experiments on the chondron level.

7. QUANTIFICATION OF SUBCHONDRAL BONE AND ARTICULAR CARTILAGE CHANGES IN THE ACLT RABBIT MODEL

7.1. Introduction

The rabbit ACLT model is increasingly being used in early OA studies, as it is known to induce rapid and severe changes in articular cartilage (Batiste et al. 2004; Vignon et al. 1987; Yoshioka et al. 1996) and subchondral bone (Batiste et al. 2004; Bouchgua et al. 2009; Wang et al. 2007). However, only a few studies (Batiste et al. 2004) have characterized early changes both in articular cartilage and subchondral bone in the rabbit ACLT model. Using micro-CT and magnetic resonance imaging (MRI) combined with a visual assessment, Batiste et al. (2004) (Batiste et al. 2004) found decreased compartmental bone mineral density (BMD) levels and changes in macroscopic surface integrity of rabbit articular cartilage as early as 4 weeks post-surgery. Recent evidence indicates that early osteoarthritic changes in the structure and composition of rabbit articular cartilage following ACLT occur in a depth-dependent manner (Mäkitalo et al. 2011; Turunen et al. 2013) and are highly site-specific (Mäkelä et al. 2014). Turunen et al. (2013) and Mäkitalo et al. (2011) found that changes first occurred in the superficial layer of patellar cartilage. Moreover, Mäkelä et al. (2014) found severer structural and compositional changes in the femoral condylar cartilages relative to the femoral groove and tibial plateau tissues in the rabbit ACLT model. However, none of the previous studies characterized early osteoarthritic changes concurrently in subchondral bone plate, trabecular bone and depth-wise changes in both cartilage structure and composition in the rabbit ACLT model.

The aim of the present study was to perform a quantitative analysis of the changes in the properties of subchondral bone, trabecular bone and articular cartilage in rabbit femoral condyles as early as 4 weeks post-ACLT. A high resolution micro-CT scanner was used to assess the three-dimensional microarchitecture and volume in the subchondral bone plate and trabecular bone. Additionally, biomechanical properties of cartilage as well as depth-wise changes in the proteoglycan content (PG), collagen orientation angle and collagen content were quantified using indentation testing, digital densitometry (DD), polarized light microscopy (PLM) and Fourier Transform Infrared (FTIR) microspectroscopy, respectively.

7.2. Materials and methods

7.2.1. Animal model

Skeletally mature female New Zealand white rabbits (Oryctolagus cuniculus, n=8, age 14 months, weight 5.4±0.6 kg) underwent unilateral ACLT under general anesthesia. The left knee was operated, while the right knee (contralateral joint-CTRL) was used as a control group. The animals were floor penned on straw

bedding and allowed to freely move within a space of 1.5 m x 1.5 m. This floor penning approach is favored over generic caging since the floor is solid and the animals are less likely to be injured when moving within the penned area. At 4 weeks post-ACLT, the animals were euthanized using an intravenous injection of sodium pentobarbital and the femoral condyles were harvested. All procedures were approved by the Committee on Animal Ethics at the University of Calgary and were carried out according to the guidelines of the Canadian Council on Animal Care. These animals were originally processed for our earlier study (Turunen et al. 2013), in which only the properties of patellar cartilage were analyzed. For the present study, femur bones were imaged and analyzed, while femoral cartilage properties were implemented for comparison.

7.2.2. Micro-computed tomography – imaging and analysis

After biomechanical measurements of cartilage (see chapter 7.2.3 Indentation testing), distal compartments of femoral condyles were taken from formalin-filled tubes and scanned using a high-resolution cone-beam micro-CT scanner (Skyscan 1172, Aarteselaar, Belgium) with isotropic voxel size of 25 μm. The X-ray tube voltage was set at 100 kV and the current was 100 μA. The 16-bit X-ray projections were obtained at 0.7° rotation step with 316 ms exposure time. A 0.5 mm thick aluminum filter was used to reduce beam-hardening artifacts and the ring artifact correction was 20. Average scan duration was 23 minutes. The cross-section images were reconstructed using a modified Feldkamp cone-beam algorithm (softwareNRecon, V1.6.2.0, Skyscan, Aarteselaar, Belgium). The reconstructed micro-CT data were first imported into Mimics software (v.12.3, Materialise, Belgium) for visualizing the 3D geometry of femoral condyles and segmentation (Figure 7.1).

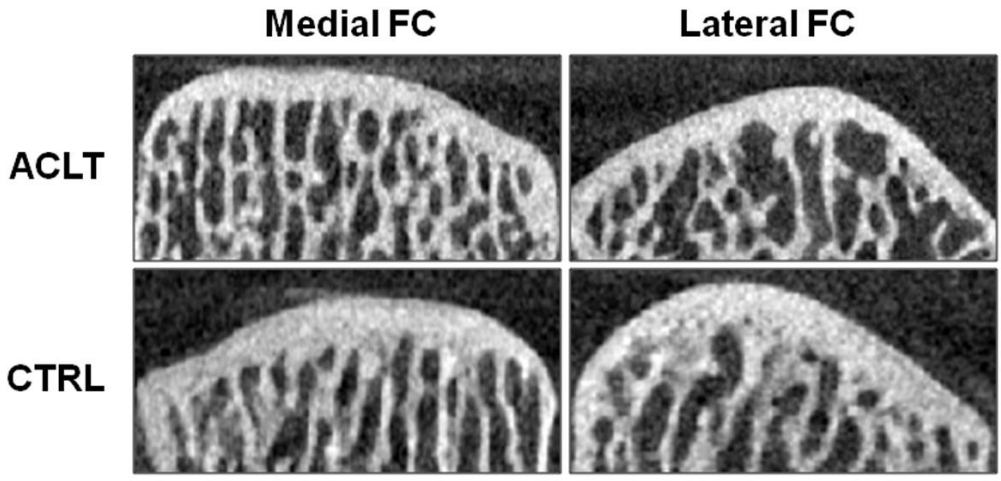

Figure 0.1 Coronal micro-CT slices of rabbit medial and lateral femoral condyles (FCs) in experimental (ACLT) and control (CTRL) groups

In order to distinguish bone tissue from non-bone tissue, all reconstructed grayscale images were segmented, using a fixed global threshold defined by visual inspection of the segmentation result. Subsequently, 2x2x4 mm^3 volumes of interest (VOIs) were placed in weight-bearing regions of medial and lateral femoral condyles (Figure 7.1). Cartilage properties were obtained from the same regions (more details later). Using Mimics software, the VOIs containing both subchondral bone plate and trabecular bone were further manually segmented using a contour-based tool in order to delineate the two components (Figure 7.2). The subchondral bone plate and trabecular bone was segmented manually a few voxels away from the endocortical boundary using previously described criteria based on the size of intracortical pores (Malo et al. 2013). According to this criteria, the endocortical boundary split the pore in the case of large pores, whereas the pore was included in the subchondral plate region if the size of a pore was less than twice the average size of pores in that region or if the size of pore was smaller than the distance from the pore to the endosteal region (i.e. the border between the bone and the bone marrow).

After separation, the segmented masks containing subchondral plate and trabecular bone were independently processed and further imported into CTAn software (Skyscan, v.1.13, Aarteselaar, Belgium), using a custom made Matlab script (The MathWorks, Inc., MA, v. 7.14.0). Image processing included Gaussian and despeckle filtering (3D, white speckles of < 8 voxels were removed). Subchondral bone plate and trabecular bone structural parameters were calculated with CTAn software according to American Society for Bone and Mineral Research (ASBMR) guidelines and computed in a direct 3D fashion based on the marching cubes algorithm without any model assumptions for 2D analysis (Hildebrand and Ruegsegger 1997; Parfitt et al. 1987).

The following 3D morphometric parameters were obtained:

- subchondral bone plate thickness (Pt.Th, μm)
- bone volume fraction (BV/TV, %), describing the ratio of bone volume over tissue volume
- trabecular thickness (Tb.Th, μm), describing the mean thickness of trabeculae, assessed using direct 3D methods
- structural model index (SMI), a quantification of the trabecular bone structure with a rod-like structure providing a SMI value of 3 (subchondral plate has an SMI value of 0 and a structure with closed holes has a negative value)
- trabecular separation (Tb.Sp, μm), size of the marrow cavities reflecting trabecular spacing.

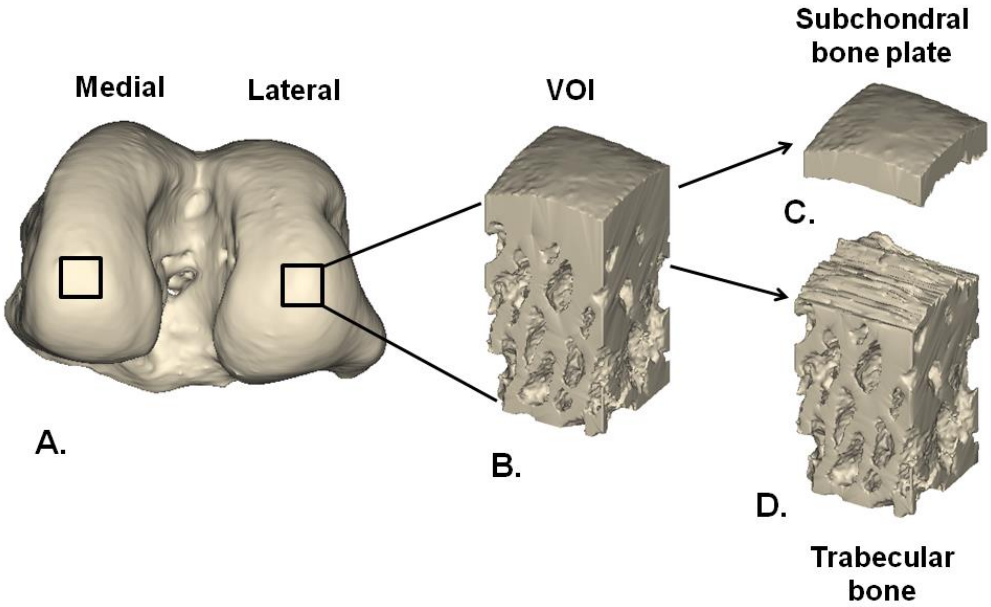

Figure 0.2 (A) 3D reconstruction of femoral condyles with volumes of interest (VOIs) indicated. (B) 3D reconstruction of medial VOI. (C) Subchondral plate VOI. (D) Trabecular bone VOI.

7.2.3. Indentation testing

The biomechanical properties of the articular cartilage samples were determined using indentation testing with a 1 mm diameter plane-ended indenter. This was done before micro-CT of bone. Measurements were done in the center of weight-bearing regions in knee flexion (apex of the posterior curvature) of medial and lateral femoral condyle cartilage (Figure 7.3). Samples were preconditioned first using a cyclic 2 % strain (4 full cycles), after which the samples were allowed to relax for ~15 min. After this, stepwise stress-relaxation test was performed on the weight-bearing regions of medial and lateral femoral condyle cartilage (100%/s ramp rate, 3x5% step, 15 min relaxation time after each step).

Sinusoidal loading was then applied (amplitude 4% of cartilage thickness, 1Hz, 4 cycles). The equilibrium modulus was calculated from the slope of the equilibrium stress-relaxation curve, and the dynamic modulus was derived from the sinusoidal test. The Poisson's ratios for cartilage were assumed to be 0.1 (Korhonen et al. 2002) and 0.5 (fast loading rate, incompressible material) in the determination of the equilibrium and dynamic modulus, respectively (Hayes et al. 1972).

7.2.4. Microscopy and spectroscopy

7.2.4.1. Sample processing

After indentation tests, femoral condyles were fixed in 10% formalin, decalcified in 10% EDTA, dehydrated in graded alcohols and treated with xylene prior embeddeding in paraffin. Coronal microscopic sections were taken from the middle region of each femoral condyle and further processed for depth-dependent microscopic and spectroscopic analysis of articular cartilage composition and structure (Figure 7.3).

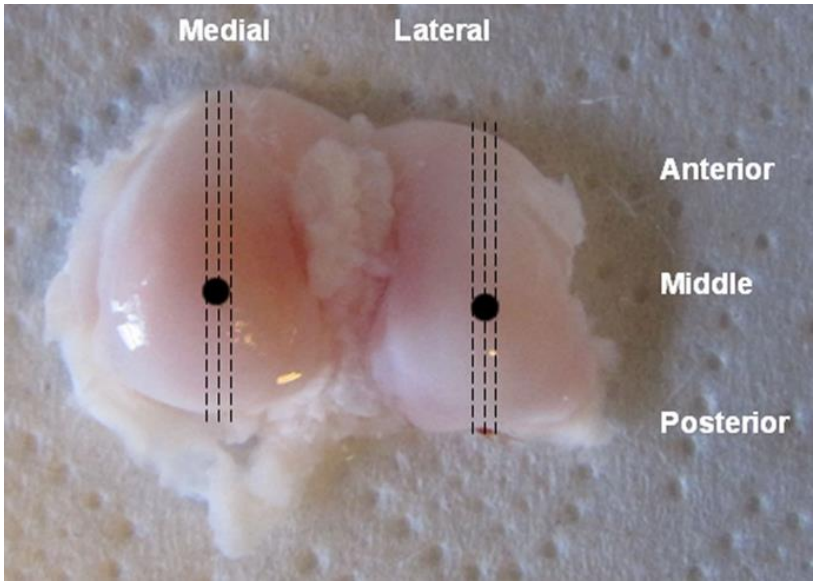

Figure 0.3 Medial and lateral rabbit femoral condyles. Dashed vertical lines represent the cutting direction lines taken for DD, PLM and FTIR measurements. The biomechanical testing was conducted on the weight-bearing regions of femoral condyles (superimposed solid circles).

For digital densitometry (DD), 3 μm thick paraffin sections were stained with Safranin-O dye, whereas for polarized light microscopy (PLM) and Fourier transform infrared imaging microscopy (FTIR), 5 μm thick microscopic sections were deparaffinized and PGs were removed with hyalurodinase digestion (1000U/ml hyalurodinase, Sigma-Aldrich, St. Louis, MO, USA).

7.2.4.2. Digital densitometry

In order to estimate the PG distribution of the cartilage samples as a function of depth from the cartilage surface to the subchondral bone, the digital densitometry method was employed. PGs in articular cartilage contain negative groups, in which the cationic dye (Safranin-O) binds to. Studies have shown that there is a linear relationship between the optical density (OD) and the amount of

PGs in the cartilage (Bisson et al. 2005; Leo et al. 2004). Therefore, the distribution of PGs can be revealed and quantified using this method.

OD is based on the Beer-Lambert law (Equation 7.1). The transmittance is obtained according to:

$$T = \frac{I'}{I_0}, \tag{0.1}$$

where I' is the power of light after passing through the sample and I_0 is the initial power of light. Thus, the measured absorbance A_b from the Beer-Lambert law is:

$$A_b = -log_{10}T = -log_{10}\frac{I'}{I_0}. \tag{0.2}$$

The spatial distribution of PGs was determined using this method for Safranin-O stained histological sections (Bisson et al. 2005; Leo et al. 2004). Three μm thick paraffin sections were cut and stained with Safranin-O dye (Figure 7.4).

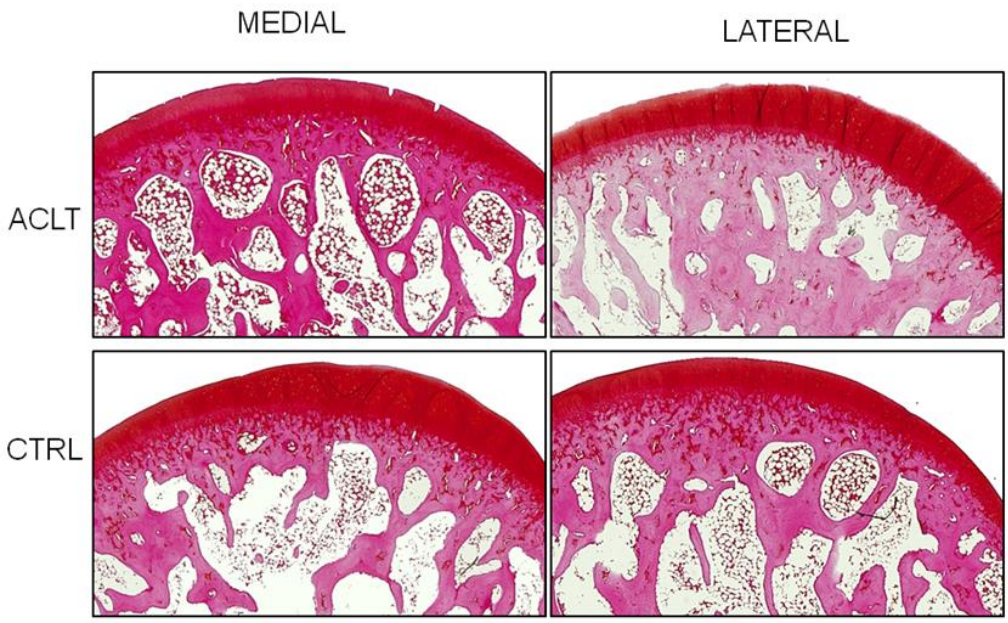

Figure 0.4 Representative histological rabbit cartilage sections of medial and lateral femoral condyles labeled with Safranin-O in experimental (ACLT) and control (CTRL) groups.

The PG content was determined from Safranin-O stained sections using a light microscope (Leitz Ortholux-II, Leitz, Wetzlar, Germany) with magnification of 4x with a computer-controlled Perkin Elmer UltraPix FSI 12-bit CCD camera (CH250, Photometrics, Tucson, AZ, USA). Grayscale images were captured and the optical density was used to estimate the distribution of tissue fixed charge density. The pixel values were averaged in the transverse direction and the average depth-wise profiles were created from the sections of each sample.

7.2.4.3. Mankin scoring

After DD, histological scoring on both medial and lateral femoral condyles of the ACLT and CTRL knee joints was performed by three independent observers using a Mankin histological score (Mankin et al. 1971). Histological analysis was performed also on a separate non-operated control (CL) group from three non-operated rabbits to validate that CTRL knee joint can serve as an appropriate control group. The Mankin grading system is a score of cartilage degeneration based on a combination of structural changes in cartilage matrix (0-6 points), cellular changes (0-3 points), biochemical changes reflected in the intensity of Safranin-O staining (0-4 points) and alterations in tidemark integrity (0-1 point) with the maximum score of 14 points (Table 7.1). The final score of each sample site was the average of three independent scores.

Table 0.1 Histological grading according to Mankin (Mankin et al. 1971)

Feature	Grade	Feature	Grade
I. Structure		III. Safranin-O staining	
Normal	0	Normal	0
Surface irregularities	1	Slight reduction	1
Pannus and surface irregularities	2	Moderate reduction	2
Clefts to transitional zone	3	Severe reduction	3
Clefts to radial zone	4	No dye noted	4
Clefts to calcified zone	5		
Complete disorganization	6		
II. Cells		IV. Tidemark integrity	
Normal	0	Intact	0
Diffuse hypercellularity	1	Crossed by blood vessels	1
Cloning	2		
Hypocellularity	3		

7.2.4.4. Polarized light microscopy

Polarized light microscopy (PLM) is a powerful tool for studying the orientation of anisotropic materials, such as biological tissues containing fibrillar collagen. PLM is done using a light microscope, two filters, a polarizer and analyzer. The polarizer is placed after the light source and ensures transmission of light only in a single plane that is perpendicular to the direction of light propagation. Optically anisotropic materials change the direction of polarized light, an effect called birefringence.

Thus, the fibrillar structure of collagen-containing tissues splits the incident polarized light into two orthogonal rays, in a way that depends on the direction of collagen at each point in the section. The observed image is created using the analyzer filter, positioned after the specimen at a right angle to the polarizer. The analyzer recombines these rays and creates the image. The orientation of the

analyzer ensures that only light with a polarization that is altered by the tissue is transmitted. The intensity of the resulting signal indicates regions of the tissue that are optically active with a capacity to alter polarization; birefringent, anisotropic, or oriented tissue.

The intensity of the emerging light can be determined with Fresnel equation:

$$I = a + b \cdot I_0 \cdot sin^2\alpha, \qquad 0 \leq \alpha \leq \pi/2, \tag{0.3}$$

where I_0 is the intensity of the light illuminating the sample, α is the rotation angle of the polarization plane, and a and b are constants dependent on the optical system.

To characterize the polarization phenomenon of a material, Stokes parameters (Rieppo et al. 2008) for each image pixel can be used as follows:

$$S_0 = I_0 + I_{90}, \tag{0.4}$$

$$S_1 = I_0 - I_{90}, \tag{0.5}$$

$$S_2 = 2I_{45} - S_0, \tag{0.6}$$

$$S_3 = S_0 + I_{(90+\lambda/4)}, \tag{0.7}$$

where $I_{(0-90^0)}$ is the intensity of the light with the polarizer at position 0-90°, S_0 the total intensity of the light, S_1 the amount linear polarization, S_2 the amount of ±45° polarization and S_3 the amount of right or left circular polarization. Subscript $\lambda/4$ refers to the image taken with a phase shifter.

The orientation angle of the collagen fibrils can then be calculated as follows:

$$\psi = \frac{arctan(S_2/S_1)}{2}, \qquad 0^0 \leq \psi \leq 90^0, \tag{0.8}$$

where ψ is the orientation angle of a polarization ellipse. ψ can be used to estimate the average orientation of collagen fibrils in each pixel as the fibrils in articular cartilage split the light passing through it into two components (one parallel and one perpendicular to the long axis of the fibril).

Using the PLM method, collagen orientation angles were analyzed (Muir et al. 1970; Yoneda 1993) on a Leitz Ortholux II POL-polarized microscope (Leitz, Wetzlar, Germany) equipped with a CCD camera (Photometrics CH 250/A, Photometrics Inc., Tucson, AZ, USA). Four sections were measured from each sample. Images were obtained using a magnification of 6.3x and the measured pixel values were averaged in the transverse direction. Mean profiles for every sample were calculated from the section profiles. In the profiles, collagen fibers parallel to the cartilage surface were assigned an angle of 0° (superficial zone) and fibers perpendicular to the cartilage surface were given an angle of 90° (deep zone).

7.2.4.5. Fourier transform infrared imaging and spectroscopy

The use of infrared (IR) spectroscopy for the analysis of biological samples was first suggested in 1910. IR spectroscopy has become an accepted tool for the characterization of biomolecules (Quinteiro Rodríguez 2000). The technique consists of irradiation of the sample with infrared radiation from an IR source in order to stimulate vibrational motions when the radiation is absorbed by the sample (Sacksteder and Barry 2001). A molecule will absorb radiation only at frequencies corresponding to its molecular modes of vibration (Quinteiro Rodríguez 2000) determining changes in their vibrational motion, changes that give rise to bands in the vibrational spectrum. Each spectral band is characterized by its frequency and amplitude (Sacksteder and Barry 2001).

Infrared absorption is directly proportional to the amount of absorbing material in the cartilage, as stated by the Beer-Lambert law (Rieppo et al. 2004):

$$A_b = a_1 b c_a \,, \tag{0.9}$$

where A_b is the measured absorbance, a_1 is the wavelength-dependent absorptivity coefficient, b is the cartilage section thickness and c_a is the cartilage concentration. All molecules present characteristic absorbance peaks. This physical property is considered as a molecular fingerprint. The infrared spectra of complex biological materials do not only describe the composition, but also provide a number of specific bands that are sensitive to structural or conformational changes. The physical state of the sample (hydration or aggregation state etc.) has also a great influence on FTIR results (Naumann et al. 1991). A great improvement was the use of an interferometer and the application of a mathematical transformation, the Fast Fourier Transform algorithm, which allow for the simultaneous detection of all the transmitted energy. Thus, the highly sensitive FTIR method was born. A great advantage of FTIR spectroscopy is that the FTIR spectrometer can be modified in order to make to study very small samples, such as tissue sections (Sacksteder and Barry 2001). When coupling a microscope to the spectrometer new interesting applications arise. In FTIR microspectroscopy it is possible to study the absorbance spectra at discrete points and create a 2D spectral map of the compounds of interest in cartilage sections (Buschmann and Grodzinsky 1995; Lai et al. 1991a; Nigg and Herzog 2007; Roth and Mow 1980). Using this method, the relative amount of the molecules of interest can be quantified, in addition to their spatial distribution, orientation, and molecular nature.

In this thesis spatial distribution of the collagen content in the cartilage was imaged and determined using a PerkinElmer Spotlight 300 (PerkinElmer, Shelton, CO, USA) with CO2-free dry air purge system (FTIR purge gas generator, Parker Hannifin corporation, Haverhill, MA, USA). Microscopic sections were installed on BaF2 windows and two sections were measured from each sample. 4 cm^{-1} spectral resolution and 6.25 µm pixel resolution with 2 repeated scans was used. The collagen content was estimated by integration of the amide I region (1585 – 1720 cm^{-1}). Amide I maps were averaged in the transverse direction, and a mean profile of two sections was calculated to create depth-wise collagen profiles for each sample. A custom made Matlab script was used for IR spectra analysis.

7.2.5. Statistical analysis

All results are expressed as mean ± standard deviation (SD). Due to the small sample size and non normal distribution of data, Wilcoxon signed-rank test for bone parameters was used to analyze the differences between the experimental (ACLT) and contralateral (CTRL) groups. Mixed linear model with Bonferroni correction (Brown and Prescott 2006) was used to analyze the differences between the experimental (ACLT) and contralateral (CTRL) cartilage sample groups. In the mixed linear model, the type of the sample was set as a fixed variable, while the PG content, collagen orientation, collagen content and biomechanical properties (equilibrium and dynamic elastic modulus) were defined as random variables. Restricted maximum likelihood (REML) estimation was used. More details concerning this mixed model are given in previous studies (Mäkelä et al. 2014; Saarakkala et al. 2010). The Mankin scores between ACLT, CTRL and CL groups were compared with the nonparametric Kruskal-Wallis test. *P*-values less than 0.05 were considered significant. All statistical analyses were carried out using SPSS software (SPSS Inc., Chicago, IL, U.S.A.).

7.3. Results

7.3.1. Subchondral bone plate thickness and trabecular bone parameters

The subchondral bone plate thickness (Pt.Th) was significantly decreased in the medial compartment of the ACLT group (-14%) compared to the control group (Table 7.2). Interestingly, the statistical analysis showed no significant change in the subchondral bone thickness in the lateral compartment of the ACLT group when compared to the control group (Table 7.2). In the control joints, the subchondral bone plate was on average 16% thicker in the lateral than medial femoral condyle, however, this difference was not statistically significant (p=0.50).

Table 0.2 Mean values (±SD) of subchondral bone plate and trabecular bone parameters in experimental (ACLT, n=8) and control (CTRL, n=8) groups

	Medial FC compartment			Lateral FC compartment		
	ACLT	CTRL	*p*	ACLT	CTRL	*p*
Subchondral bone plate						
Pt.Th (μm)	399.9±97.0*	471.7±59.7	0.017*	532.6±101.2	545.4±91.1	0.889
Trabecular bone						
BV/TV (%)	45.4±4.8*	49.8±6.3	0.012*	47.8±7.1	46.0±3.5	0.327
Tb.Th (μm)	208.5±31.0*	226.3±29.5	0.017*	233.3±27.2	228.3±18.1	0.484
SMI	0.0±0.2	-0.1±0.3	0.161	-0.0±0.3	0.0±0.2	0.575
Tb.Sp (μm)	296.2±19.3	284.3±24.4	0.093	321.3±36.8	317.5±40.2	0.484

* values are statistically significantly different from the CTRL group ($p<0.05$)

The trabecular bone in the ACLT model possessed statistically significantly less bone volume fraction (BV/TV, -8.45%) and thinner trabeculae (Tb.Th, -7.78%) only in the medial compartment as compared to the CTRL group (Table 7.2). Despite these changes in trabecular structure, no significant changes were seen in either trabecular spacing or SMI between the ACLT and CTRL joints. Additionally, in both compartments from both groups, SMI yielded values from 0 to negative indicating either a plate-like bone structure (SMI =0) or an enclosed cavity structure (SMI negative values) due to the presence of more concave than convex trabecular surfaces evaluated directly underneath the subchondral plate.

7.3.2. Mechanical, structural and compositional properties of articular cartilage

The elastic equilibrium modulus of cartilage (Table 7.3.) was significantly lower in both lateral and medial compartments of the ACLT joints compared to the CTRL joints ($p<0.05$). However, no significant change was observed in the dynamic modulus of the ACLT joint cartilage when compared to CTRL joint cartilage.

Table 0.3 Mean values (±SD) of cartilage equilibrium modulus and dynamic modulus of experimental (ACLT, n=8) and control (CTRL, n=8) groups. Lat = lateral compartment, Med = medial compartment.

	Equilibrium elastic modulus (MPa)	Dynamic elastic modulus (MPa)
ACLT Med	0.61±0.43*	1.98±0.56
CTRL Med	1.26±0.45	3.51±1.24
ACLT Lat	0.58±0.39*	2.86±1.32
CTRL Lat	1.12±0.48	3.44±1.44

* *p<0.05* vs. CTRL group

Digital densitometry revealed significantly reduced proteoglycan content in the ACLT joint cartilage compared to the CTRL group tissue, in both lateral and medial femoral condyles (Figure 7.5). PLM indicated significant collagen fibril orientation changes post-surgery in the ACLT group. The orientation angle of the collagen fibrils in the superficial cartilage was significantly less parallel to the surface ($p<0.05$) in the ACLT group than in the CTRL group. The altered orientation angle of cartilage extended up to over 50% of tissue thickness in the lateral femoral condyle. The collagen content increased significantly (Amide I absorption) in the deeper zones of the ACLT group cartilage compared to the CTRL group cartilage ($p<0.05$).

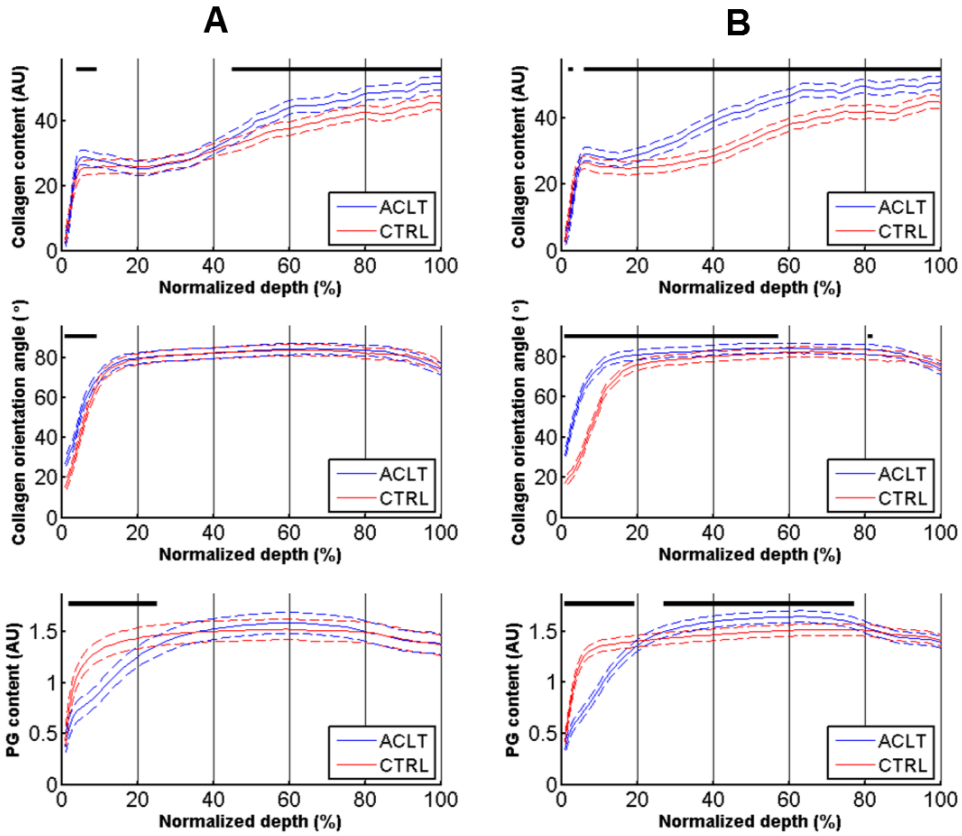

Figure 0.5 Collagen content (AU= absorption unit), collagen orientation angle and proteoglycan content of cartilage in ACLT (blue line) and CTRL (red line) groups as a function of tissue depth (mean, 95% CI, n=8 in both groups), measured with FTIR microspectroscopy, PLM and DD, respectively. (A) medial femoral condyle compartment; (B) lateral femoral condyle compartment. The superimposed line indicates where significant differences occurred ($p < 0.05$).

The average Mankin score in both lateral and medial femoral condyles of ACLT groups was mild to moderate, but significantly higher, as compared to both contralateral control CTRL (p=0.03) and non-operated control groups (p=0.01) (Table 7.4). Cartilage samples with mild OA showed a Mankin score of 1-6, while three samples with advanced OA had a Mankin score of 10-11. However, no significant differences were noted between lateral and medial femoral condyles of CTRL and control groups, indicating that CTRL knee joint can be used as a valid control.

Table 0.4 Mean (±SD) Mankin score values for experimental (ACLT, n=8), contralateral control (CTRL, n=8) and non-operated control (CL, n=6) groups. Lat = lateral compartment, Med = medial compartment

	Mankin score
ACLT Med	4.75±2.55*,**
CTRL Med	1.35±1.06
CL Med	0.00±0.00
ACLT Lat	4.50±4.07*,**
CTRL Lat	0.87±0.99
CL Lat	0.66±1.60

* $p<0.05$ vs. CTRL group
** $p<0.05$ vs. CL group

7.4. Discussion

The present study characterized bone and overlying articular cartilage properties in a rabbit ACLT model as early as 4 weeks post-surgery. Femoral condyles were chosen for this study because previous studies have shown that they are the most affected by ACLT when compared to the other locations in the rabbit knee joint (Chang et al. 1997; Mäkelä et al. 2014). To the best of our knowledge, this is the first study that quantifies parallel changes in the subchondral bone plate and trabecular structure with cartilage structure and function in this experimental model. The results indicated that significant thinning of the subchondral bone plate accompanied by decreased trabecular bone volume and thickness occurred only in the medial femoral condyle of the ACLT joint. These changes were concurrent with the loss of PGs, disorganization of the collagen fibrils, increased collagen content and alterations in the equilibrium modulus of cartilage. However, more severe alterations in cartilage structure were observed in the lateral compartment without alterations in the underlying bone. For comparative purposes, the current findings are discussed in the context of surgically induced animal models of OA, particularly with ACLT and menisectomy interventions.

In the medial condyles of the ACLT group, we found significant decreases in the subchondral plate thickness, bone volume fraction and trabecular thickness within 4 weeks post-surgery. This indicated accelerated bone resorption, consistent with an earlier study investigating surgically induced OA in the rabbit 8 weeks post-ACLT (Wang et al. 2007). In two ACLT canine models of OA, Sniekers et al. (2008) and Kuroki et al. (2011) also found early thinning of the subchondral bone plate and loss of trabecular bone 10-12 weeks post-surgery. These authors concluded that subchondral bone thinning is related to early changes of OA, whereas trabecular bone loss is likely a result of altered joint loading due to the ACLT. Also, thinning of the subchondral bone plate was associated with increased cartilage damage in the ACLT-menisectomy model of OA in both rabbits (Bellido et al. 2010) and dogs (Intema et al. 2010). In contrast to these earlier studies, we showed here significant subchondral bone plate thinning and trabecular bone loss only in the medial compartment. However, the lateral compartment contained no significant subchondral bone changes. These changes may be explained by the following reasons.

Firstly, gait alterations and joint unloading have been previously reported in a rabbit model (Bray et al. 1992) and also in canine models following ACLT (Korvick et al. 1994; O'Connor et al. 1989). ACLT produces instability of the knee by abnormal anterior-posterior and rotational motions (Nigg and Herzog 2007). Altered loading conditions are associated with changed contact pressures and stress distributions as well as diminished muscle function within feline ACLT joints (Herzog et al. 1998). According to Wolff's law, unloading will lead to an adaptive bone remodeling process that in the present study may have decreased subchondral plate thickness, trabecular bone volume fraction and trabecular thickness in more unloaded joint compartment.

Secondly, the mechanisms involved in early subchondral bone remodeling may also be explained by an activation of osteoclast formation through an inflammatory response (Yoneda 1993) or through increased blood flow in the subchondral bone (Judex et al. 1997) which may have enhanced bone resorption. Both of these mentioned biomechanical and biochemical pathways can contribute to subchondral and trabecular bone loss in the medial compartment seen in the present study.

Thirdly, unaltered bone properties in the lateral compartment as a result of the ACLT may suggest that forces transferred from cartilage into the bone and bone remodeling have remained in the normal level in the lateral side. It may also be that the adaptive process is faster in the lateral compartment, i.e. bone has recovered from the possible initial loss of mass.

Several studies of rabbit joint biomechanics (Bendele 2001; Gushue et al. 2005) have demonstrated the predominance of lateral compartment in knee joint loading. Therefore, as a result of greater loading bone modeling might be concentrated in the lateral compartment. The present study indirectly supports this finding as indicated by over 15% thicker subchondral bone plate in the lateral femoral condyle compartment compared to the medial compartment of the control groups.

As a result of ACLT, the collagen orientation angle (as quantified with PLM) became less parallel to the cartilage surface indicating collagen network fibrillation, while the PG content (as quantified with DD) was reduced significantly from the superficial to middle zone in the ACLT joint cartilage compared to the control group. This is in line with findings from previous studies in ACLT rabbit models of OA in patella, where early changes in collagen orientation and decreases in proteoglycan content were observed at four (Turunen et al. 2013) and eight (Mäkitalo et al. 2011) weeks post-surgery. Although changes in collagen orientation angles and proteoglycan content were observed in both cartilage compartments of the ACLT group, in contrast to bone changes, more pronounced cartilage changes that extended deeper into the tissue depth were found in the lateral than medial compartment. This is likely due to the instability in rotations and translations of the joint, leading to increased mechanical load and shear strains/stresses primarily in the lateral compartment (Bendele 2001).

The collagen content (as quantified with FTIR) increased significantly especially in the deep tissue of the ACLT joint cartilage compared to the control joint cartilage. Again, this alteration was more severe in the lateral than medial joint compartment. This was surprising since previous studies in surgically induced rabbit models of OA have either found a slight decrease in the collagen content (Bi et al. 2006; Rogart et al. 1999) or no change (Bi et al. 2006; Mäkitalo et al. 2011; Turunen et al. 2013). There is evidence that synthesis of type II collagen is strongly up-regulated in response to joint instability possibly indicating an active repair

response during the early phase of OA (Bi et al. 2007; Hotta et al. 2005; Lorenz et al. 2005; Matyas et al. 1999). Thus, the increased collagen content of the ACLT joint cartilage tissues from our study may also be attributable to this phenomenon.

The equilibrium modulus was reduced significantly in the ACLT joint samples. This was likely a result of the observed PG loss (Korhonen et al. 2003; Sah et al. 1997). Interestingly, even though significant alterations in the superficial collagen architecture occurred in the ACLT joints, and it was assumed to affect the dynamic modulus (Julkunen et al. 2008, Korhonen et al. 2003), no statistically significant difference in the dynamic modulus was found between the ACLT and control groups. Increased collagen content in the deeper tissue of the ACLT group samples, which should also contribute directly to the dynamic modulus (Korhonen et al. 2003), may have counteracted the effect of collagen fibrillation. On the other hand, the difference in the dynamic modulus between the experimental and control groups was ~20% and ~77% in the lateral and medial joint compartments, smaller values representing the ACLT joint. Thus, the difference between the groups might become significant with more number of samples.

More mild changes in cartilage properties in the medial than lateral compartment might be explained by the underlying bone. The observed subchondral bone loss in the medial compartment could theoretically reduce the stiffness of bone which could in turn result in higher levels of bone deformation, reducing forces experienced by cartilage in the contact areas. Degenerative changes of cartilage in the medial compartment might also be simply explained by joint unloading, since joint immobilization has been shown to cause glycosaminoglycan loss and reduced cartilage stiffness (Jurvelin et al. 1986; Tammi et al. 1983).

This study demonstrates that the contralateral knee joint can be used as a valid control (shown by Mankin score). This is consistent with the previous studies utilizing the contralateral knee joint as a control in a rabbit ACLT model of OA (Anetzberger et al. 2012; Han et al. 2010; Turunen et al. 2013).

A limitation of this study was the influence of global thresholding of micro-CT data to obtain a binary representation of mineralized subchondral bone. However, a consistently applied threshold ensured reliable comparison between study groups, although the absolute value of these measures may include a small uncertainly. Even though the resolution of the micro-CT measurements could have significant effects on the structural bone parameters (Isaksson et al. 2011), this source of error was unlikely to bias measures of trabecular thickness which were on the order of 200 μm.

This study provides novel information about the microstructural changes of subchondral plate and trabecular bone simultaneously with structural and functional changes of cartilage in a rabbit model of very early osteoarthritis. Based on our findings, it appears that the very early osteoarthritic changes of cartilage precede those of subchondral and trabecular bone in the lateral knee joint compartment, while in the medial compartment, cartilage and bone experience degenerative alterations simultaneously. Thus, this study increases the knowledge of the mechanisms at very early stages of OA. The present findings highlight the importance of considering both cartilage and bone and abnormal joint loading in the initiation of OA, which occur in a highly site-specific manner.

8. CONCLUSIONS

8.1. Conclusions

The work presented in this thesis provides essential insights into the role of biomechanical properties of single chondrocytes, structure-function relationships in articular cartilage and subchondral bone in healthy and diseased state.

AFM has rapidly become a valuable nanotool for quantifying the mechanical properties of single cells. At the nanoscale, the local nonlinear cellular mechanical responses at three different strain levels using AFM nanoindentation were analyzed in normal and Cytochalasin D treated condrocytes. A new approach consisting in FE analysis combined with optimization algorithms and AFM nanoindentation experiments was developed to determine the time-dependent cell responses.

At the tissue scale, a micro-CT scanner was used to determine the three-dimensional microarchitecture and volume in the subchondral bone plate and trabecular bone in early OA (rabbit ACLT model). Additionally, depth-wise changes in the proteoglycan content, collagen orientation angle and collagen content as well as biomechanical properties of cartilage were analyzed using DD, PLM, FTIR and indentation testing, respectively.

The main results and conclusions of the thesis can be summarized as follows:

- A consistent methodology for AFM nanoindentation was initially developed and optimized in order to quantify consistently mechanical properties of soft materials using Hertz model.
- The local elastic properties of chondrocytes changed as a function of strain, whereas in the Cytochalasin D treated condrocytes this nonlinear elastic behavior was negligible.
- The intracellular fluid flow redistribution together with the solid network viscoelasticity has a critical role in determining the time-dependent response of chondrocytes in AFM nanoindentation. While the elastic modulus was reduced substantially in Cytochalasin D treated chondrocytes, alterations in viscoelastic relaxation and permeability were minor. The hyperporoviscoelastic material models are suggested to be good candidates for investigating the mechanical responses of normal and altered chondrocytes in AFM nanoindentation.
- Significant decreases in the subchondral bone plate thickness, bone volume fraction and trabecular thickness were detected in a rabbit model of early OA by use of micro-computed tomography. This may be related to altered loading and kinematics in the experimental knee.
- In this rabbit model of early OA, structural changes in cartilage samples were severer in the lateral compartment and preceded alterations in the underlying bone. In the medial compartment, altered bone properties occurred together with structural changes in cartilage. Both cartilage and bone and abnormal joint loading should be considered in the initiation of OA, which occur in a highly site-specific manner.

To conclude, the combination of the abovementioned nano- and microscale techniques has proven to be reliable tools to study and quantify structural and biomechanical properties of cartilage and underlying bone across different length scales. A more detailed understanding of the mechanical properties of chondrocytes and early OA changes in the cartilage and subchondral bone is needed in order to develop therapies capable of identifying the early stage of the disease and prevent the cartilage from degradation.

8.2. Contributions

The main contributions are:

- Designing and performing the nanoindentation experiments with an atomic force microscope in order to determinine the local elastic properties of agarose gels;
- Analyzing the nanoindentation data of the agarose gels using a custom made LabVIEW programe based on the Hertz model, statistical analysis of the data and interpretation of the results;
- Designing and performing the nanoindentation experiments with an atomic force microscope in order to determinine the local nonlinear mechanical properties of normal and altered chondrocytes at three different levels of strain nanoindentation;
- Analyzing the nanoindentation data of the normal and altered chondrocytes using a custom made LabVIEW program based on the Hertz model, statistical analysis of the data and interpretation of the results;
- Analyzing the stress-relaxation curves of normal and degraded articular chondrocytes using a combined approach of experimental nanoindentation with finite element modelling by using three different material models (hyperporoelastic, hyperviscoelastic and hyperporoviscoelastic model) and interpretation of the results;
- Processing and performing the segmentation of the micro-CT bone image data using Mimics software;
- Analyzing the subchondral bone plate and trabecular bone parameters using CTAn software, statistical analysis of the data and interpretation of the results;
- Conducting the histological analysis of experimental and control cartilage samples using the Mankin scoring system, compared the bone and cartilage parameters and interpretation of the results;

8.3. Future research

This thesis is part of a research program in the Department of Applied Physics, University of Eastern Finland, which aims at the understanding of basic pathways in how changed mechanical loading and cartilage structure and composition affects chondrocyte deformation in health and disease. Therefore, a hierarchical approach is adopted, incorporating experimental and computational models at different length scales and levels of complexity (Korhonen et al., 2008,

Turunen et al., 2013, Tanska et al., 2013). Experimental studies include the evaluation of the mechanical behavior of cartilage at single cell level, as presented in this thesis and at tissue level (Turunen et al., 2013, Fick et al., 2014). Computational models include a single cell model (chapter 5), cell embedded in cartilage matrix (multi-scale models) (Tanska et al., 2013, Korhonen et al., 2008), tissue models (Mäkelä et al. 2013) and patient-specific knee joint models (Mononen et al., 2013). The main methods employed are macro-, micro- and nano- level mechanical testing, computational modeling coupled with different imaging modalities at different length scales. This is a multidisciplinary research area which combines engineering, biomechanics, material science and cell biology. The viscoelastic/poroelastic properties of chondrocytes as characterized in this thesis will be used as an input for the multi-scale computational models (Tanska et al. 2013). This will give insights into how forces experienced by joint surfaces for instance during human walking are transmitted through tissue to cells. Moreover, to accurately model the mechanical characteristics of single chondrocytes, an evaluation of the cellular microenvironment (chondron) is necessary to be further considered. This will eventually permit a better prediction of the cellular mechanical behavior and tissue responses under macroscopic loading conditions, thereby providing insights into the mechanisms and mechanotransduction in health and disease.

BIBLIOGRAPHY

Alexopoulos LG, Haider MA, Vail TP, Guilak F (2003) Alterations in the mechanical properties of the human chondrocyte pericellular matrix with osteoarthritis. J Biomech Eng 125:323-333.

Alexopoulos LG, Setton LA, Guilak F (2005) The biomechanical role of the chondrocyte pericellular matrix in articular cartilage. Acta Biomater 1:317-325.

Alford JW, Cole BJ (2005) Cartilage restoration, part 1: basic science, historical perspective, patient evaluation, and treatment options. Am J Sports Med 33:295-306.

Amblard D, Lafage-Proust MH, Chamson A, Rattner A, Collet P, Alexandre C, Vico L (2003) Lower bone cellular activities in male and female mature C3H/HeJ mice are associated with higher bone mass and different pyridinium crosslink profiles compared to C57BL/6J mice. J Bone Miner Metab 21:377-387.

Andriacchi TP, Mundermann A, Smith RL, Alexander EJ, Dyrby CO, Koo S (2004) A framework for the in vivo pathomechanics of osteoarthritis at the knee. Ann Biomed Eng 32:447-457.

Anetzberger H, Mayer A, Schulz CU, Muller-Gerbl M (2012) Computed tomography osteoabsorptiometry is reliable for the determination of the subchondral bone mineralization distribution in the rabbit knee. Eur Surg Res 48:208-214.

Ateshian GA, Costa KD, Hung CT (2007) A theoretical analysis of water transport through chondrocytes. Biomech Model Mechanobiol 6:91-101.

Bader DL, Ohashi T, Knight MM, Lee DA, Sato M (2002) Deformation properties of articular chondrocytes: a critique of three separate techniques. Biorheology 39:69-78.

Bae WC, Wong VW, Hwang J, Antonacci JM, Nugent-Derfus GE, Blewis ME, Temple-Wong MM, Sah RL (2008) Wear-lines and split-lines of human patellar cartilage: relation to tensile biomechanical properties. Osteoarthritis Cartilage 16:841-845.

Batiste DL, Kirkley A, Laverty S, Thain LM, Spouge AR, Holdsworth DW (2004) Ex vivo characterization of articular cartilage and bone lesions in a rabbit ACL transection model of osteoarthritis using MRI and micro-CT. Osteoarthritis Cartilage 12:986-996.

Bellido M, Lugo L, Roman-Blas JA, Castaneda S, Caeiro JR, Dapia S, Calvo E, Largo R, Herrero-Beaumont G (2010) Subchondral bone microstructural damage by increased remodelling aggravates experimental osteoarthritis preceded by osteoporosis. Arthritis Res Ther 12:R152.

Bendele AM (2001) Animal models of osteoarthritis. J Musculoskelet Neuronal Interact 1:363-376.

Benjamin M, Archer CW, Ralphs JR (1994) Cytoskeleton of cartilage cells. Microsc Res Tech 28:372-377.

Benninghoff A, 1925. Form und bau der gelenkknorpel in ihren beziehungen zur funktion. In: Anonymous II. Der Aufbau Des Gelenkknorpels in Seinen Beziehungen Zur Funktion. Zeitschrift fur Zellforschung und mikroskopische Anatomie, 783-862.

Benoit M, Gabriel D, Gerisch G, Gaub HE (2000) Discrete interactions in cell adhesion measured by single-molecule force spectroscopy. Nat Cell Biol 2:313-317.

Berdyyeva TK, Woodworth CD, Sokolov I (2005) Human epithelial cells increase their rigidity with ageing in vitro: direct measurements. Phys Med Biol 50:81-92.

Bhushan B (2008) Nanotribology and nanomechanics in nano/biotechnology. Philos Trans A Math Phys Eng Sci 366:1499-1537.

Bi X, Yang X, Bostrom MP, Bartusik D, Ramaswamy S, Fishbein KW, Spencer RG, Camacho NP (2007) Fourier transform infrared imaging and MR microscopy studies detect compositional and structural changes in cartilage in a rabbit model of osteoarthritis. Anal Bioanal Chem 387:1601-1612.

Bi X, Yang X, Bostrom MP, Camacho NP (2006) Fourier transform infrared imaging spectroscopy investigations in the pathogenesis and repair of cartilage. Biochim Biophys Acta 1758:934-941.

Bidhendi AJ, Korhonen RK (2012) A finite element study of micropipette aspiration of single cells: effect of compressibility. Comput Math Methods Med 2012:192618.

Biewener AA, Bertram JE (1994) Structural response of growing bone to exercise and disuse. J Appl Physiol (1985) 76:946-955.

Binnig G, Quate CF, Gerber C (1986) Atomic force microscope. Phys Rev Lett 56:930-933.

Bisson L, Brahmabhatt V, Marzo J (2005) Split-line orientation of the talar dome articular cartilage. Arthroscopy 21:570-573.

Blain EJ (2009) Involvement of the cytoskeletal elements in articular cartilage homeostasis and pathology. Int J Exp Pathol 90:1-15.

Blumenkrantz G, Lindsey CT, Dunn TC, Jin H, Ries MD, Link TM, Steinbach LS, Majumdar S (2004) A pilot, two-year longitudinal study of the interrelationship between trabecular bone and articular cartilage in the osteoarthritic knee. Osteoarthritis Cartilage 12:997-1005.

Bobinac D, Spanjol J, Zoricic S, Maric I (2003) Changes in articular cartilage and subchondral bone histomorphometry in osteoarthritic knee joints in humans. Bone 32:284-290.

Bouchgua M, Alexander K, Carmel EN, d'Anjou MA, Beauchamp G, Richard H, Laverty S (2009) Use of routine clinical multimodality imaging in a rabbit model of osteoarthritis--part II: bone mineral density assessment. Osteoarthritis Cartilage 17:197-204.

Boyce BF, Yao Z, Xing L (2009) Osteoclasts have multiple roles in bone in addition to bone resorption. Crit Rev Eukaryot Gene Expr 19:171-180.

Boyd SK, Muller R, Leonard T, Herzog W (2005) Long-term periarticular bone adaptation in a feline knee injury model for post-traumatic experimental osteoarthritis. Osteoarthritis Cartilage 13:235-242.

Brandt KD (1994) Insights into the natural history of osteoarthritis provided by the cruciate-deficient dog. An animal model of osteoarthritis. Ann N Y Acad Sci 732:199-205.

Bray RC, Shrive NG, Frank CB, Chimich DD (1992) The early effects of joint immobilization on medial collateral ligament healing in an ACL-deficient knee: a gross anatomic and biomechanical investigation in the adult rabbit model. J Orthop Res 10:157-166.

Broom ND (1984) Further insights into the structural principles governing the function of articular cartilage. J Anat 139 (Pt 2):275-294.

Brown H, Prescott R (2006) Applied mixed models in medicine. John Wiley & Sons, Chichester, West Sussex, England.
Buckland-Wright C (2004) Subchondral bone changes in hand and knee osteoarthritis detected by radiography. Osteoarthritis Cartilage 12 Suppl A:S10-9.
Bückle H, 1971. Science of Hardness Testing and its Research Applications. In: Westbrook, J.H., Conrad, H. (Eds.) American Society for Metals, Metals Park, Ohio, 453.
Buckwalter JA, Glimcher MJ, Cooper RR, Recker R (1996) Bone biology. II: Formation, form, modeling, remodeling, and regulation of cell function. Instr Course Lect 45:387-399.
Buckwalter JA, Mankin HJ (1998) Articular cartilage: tissue design and chondrocyte-matrix interactions. Instr Course Lect 47:477-486.
Buckwalter JA, Mankin HJ, Grodzinsky AJ (2005) Articular cartilage and osteoarthritis. Instr Course Lect 54:465-480.
Buie HR, Campbell GM, Klinck RJ, MacNeil JA, Boyd SK (2007) Automatic segmentation of cortical and trabecular compartments based on a dual threshold technique for in vivo micro-CT bone analysis. Bone 41:505-515.
Bullough PG, Jagannath A (1983) The morphology of the calcification front in articular cartilage. Its significance in joint function. J Bone Joint Surg Br 65:72-78.
Burr DB (2004) The importance of subchondral bone in the progression of osteoarthritis. J Rheumatol Suppl 70:77-80.
Burr DB, Gallant MA (2012) Bone remodelling in osteoarthritis. Nat Rev Rheumatol 8:665-673.
Burr DB, Schaffler MB (1997) The involvement of subchondral mineralized tissues in osteoarthrosis: quantitative microscopic evidence. Microsc Res Tech 37:343-357.
Buschmann MD, Grodzinsky AJ (1995) A molecular model of proteoglycan-associated electrostatic forces in cartilage mechanics. J Biomech Eng 117:179-192.
Butt HJ, Jaschke M (1995) Calculation of thermal noise in atomic force microscopy. Nanotechnology 6:1.
Caille N, Thoumine O, Tardy Y, Meister JJ (2002) Contribution of the nucleus to the mechanical properties of endothelial cells. J Biomech 35:177-187.
Cappella B, Baschieri P, Frediani C, Miccoli P, Ascoli C (1997) Force-distance curves by AFM. A powerful technique for studying surface interactions. IEEE Eng Med Biol Mag 16:58-65.
Carl P, Schillers H (2008) Elasticity measurement of living cells with an atomic force microscope: data acquisition and processing. Pflugers Arch 457:551-559.
Chahine NO, Blanchette C, Thomas CB, Lu J, Haudenschild D, Loots GG (2013) Effect of age and cytoskeletal elements on the indentation-dependent mechanical properties of chondrocytes. PLoS One 8:e61651.
Chahine NO, Hung CT, Ateshian GA (2007) In-situ measurements of chondrocyte deformation under transient loading. Eur Cell Mater 13:100-11.
Chang DG, Iverson EP, Schinagl RM, Sonoda M, Amiel D, Coutts RD, Sah RL (1997) Quantitation and localization of cartilage degeneration following the induction of osteoarthritis in the rabbit knee. Osteoarthritis Cartilage 5:357-372.
Clark JM (1991) Variation of collagen fiber alignment in a joint surface: a scanning electron microscope study of the tibial plateau in dog, rabbit, and man. J Orthop Res 9:246-257.

Clarke B (2008) Normal bone anatomy and physiology. Clin J Am Soc Nephrol 3 Suppl 3:S131-9.

Cleveland JP, Manne S, Bocek D, Hansma PK (1993) A nondestructive method for determining the spring constant of cantilevers for scanning force microscopy. Review of Scientific Instruments 64:403-405.

Cook SM, Schäffer TE, Chynoweth KM, Wigton M, Simmonds RW, Lang KM (2006) Practical implementation of dynamic methods for measuring atomic force microscope cantilever spring constants. Nanotechnology 17:2135.

Cooper JA (1987) Effects of cytochalasin and phalloidin on actin. J Cell Biol 105:1473-1478.

Costa KD, Ho MY, Hung CT (2003) Multi-scale Measurement of Mechanical Properties of Soft Samples with Atomic Force Microscopy.

Costa KD, Sim AJ, Yin FC (2006) Non-Hertzian approach to analyzing mechanical properties of endothelial cells probed by atomic force microscopy. J Biomech Eng 128:176-184.

Cremer MA, Rosloniec EF, Kang AH (1998) The cartilage collagens: a review of their structure, organization, and role in the pathogenesis of experimental arthritis in animals and in human rheumatic disease. J Mol Med (Berl) 76:275-288.

Darling EM, Topel M, Zauscher S, Vail TP, Guilak F (2008) Viscoelastic properties of human mesenchymally-derived stem cells and primary osteoblasts, chondrocytes, and adipocytes. J Biomech 41:454-464.

Darling EM, Zauscher S, Guilak F (2006) Viscoelastic properties of zonal articular chondrocytes measured by atomic force microscopy. Osteoarthritis Cartilage 14:571-579.

Dedrick DK, Goldstein SA, Brandt KD, O'Connor BL, Goulet RW, Albrecht M (1993) A longitudinal study of subchondral plate and trabecular bone in cruciate-deficient dogs with osteoarthritis followed up for 54 months. Arthritis Rheum 36:1460-1467.

Dimitriadis EK, Horkay F, Maresca J, Kachar B, Chadwick RS (2002) Determination of Elastic Moduli of Thin Layers of Soft Material Using the Atomic Force Microscope. Biophys J 82:2798-2810.

Ducy P, Schinke T, Karsenty G (2000) The osteoblast: a sophisticated fibroblast under central surveillance. Science 289:1501-1504.

Durrant LA, Archer CW, Benjamin M, Ralphs JR (1999) Organisation of the chondrocyte cytoskeleton and its response to changing mechanical conditions in organ culture. J Anat 194 (Pt 3):343-353.

Eggli PS, Hunziker EB, Schenk RK (1988) Quantitation of structural features characterizing weight- and less-weight-bearing regions in articular cartilage: a stereological analysis of medial femoral condyles in young adult rabbits. Anat Rec 222:217-227.

Eyre DR, McDevitt CA, Billingham ME, Muir H (1980) Biosynthesis of collagen and other matrix proteins by articular cartilage in experimental osteoarthrosis. Biochem J 188:823-837.

Eyre DR, Oguchi H (1980) The hydroxypyridinium crosslinks of skeletal collagens: their measurement, properties and a proposed pathway of formation. Biochem Biophys Res Commun 92:403-410.

Feldkamp LA, Goldstein SA, Parfitt MA, Jesion G, Kleerekoper M (1989) The direct examination of three-dimensional bone architecture in vitro by computed tomography. J Bone Miner Res 4:3-11.

Fletcher LM, Welsh GI, Oatey PB, Tavare JM (2000) Role for the microtubule cytoskeleton in GLUT4 vesicle trafficking and in the regulation of insulin-stimulated glucose uptake. Biochem J 352 Pt 2:267-276.

Florea C, Dreucean M, Laasanen MS, Halvari A (2011) Determination of young's modulus using AFM nanoindentation. Applications on bone structures. E-Health and Bioengineering Conference (EHB), Iasi, Romania 1:1-4.

Florea C, Berdich K, Dreucean M (2012) Topography imaging of material surfaces using Atomic Force Microscope. Solid State Phenomena 188, Advanced Materials and Structures 4:199-204.

Florea C, Malo MKH, Rautiainen J, Mäkelä J, Nieminen MT, Jurvelin JS, Davidescu A, Korhonen RK (2013) Alterations in bone and cartilage properties at 4 weeks after anterior cruciate ligament transection of rabbits, 8th Meeting of the Combined Orthopaedic Research Societies (CORS) Venice, Italy.

Florea C, Mononen ME, Tanska PK, Lammi MJ, Laasanen MS, Korhonen RK (2014) Intracellular fluid flow controls viscoelastic properties of chondrocytes in nanoindentation. Trans Orthop Soc 39:0434.

Florea C, Jakorinne A, Lammi M, Davidescu A, Korhonen RK (2013) Determination of Mechanical Properties of Chondrocytes in Articular Cartilage using Atomic Force Microscopy, 5th International Conference on advanced materials and structures (AMS) Timisoara, Romania.

Fritton JC, Myers ER, Wright TM, van der Meulen MC (2005) Loading induces site-specific increases in mineral content assessed by microcomputed tomography of the mouse tibia. Bone 36:1030-1038.

Gibson CT, Smith DA, Roberts CJ (2005) Calibration of silicon atomic force microscope cantilevers. Nanotechnology 16:234.

Gibson CT, Watson GS, Myhra S (1996) Determination of the spring constants of probes for force microscopy/spectroscopy. Nanotechnology 7:259.

Goldring SR, Goldring MB (2010) Bone and cartilage in osteoarthritis: is what's best for one good or bad for the other? Arthritis Res Ther 12:143.

Grodzinsky AJ, Levenston ME, Jin M, Frank EH (2000) Cartilage tissue remodeling in response to mechanical forces. Annu Rev Biomed Eng 2:691-713.

Grynpas MD, Alpert B, Katz I, Lieberman I, Pritzker KP (1991) Subchondral bone in osteoarthritis. Calcif Tissue Int 49:20-26.

Guilak F, Sah RL, Setton LA, 1997. Physical regulation of cartilage metabolism. In: Basic Orthopaedic Biomechanics. . In: Mow ,V.C.,Hayes,W.C (Ed.), Basic Orthopaedic Biomechanics. Lippincott-Raven, Philadelphia, 179-207.

Guilak F, Setton LA, Kraus VB, 2000. Structure and function of articular cartilage. In: Garett, W.E.J., Speer K.P., Kirkendall, D.T. (Eds.) Principles and Practice of Orthopaedic Sports Medicine. Lippincott Williams& Wilkins, Philadelphia, 53-73.

Guilak F (2000) The deformation behavior and viscoelastic properties of chondrocytes in articular cartilage. Biorheology 37:27-44.

Guilak F (1995) Compression-induced changes in the shape and volume of the chondrocyte nucleus. J Biomech 28:1529-1541.

Guilak F, Alexopoulos LG, Upton ML, Youn I, Choi JB, Cao L, Setton LA, Haider MA (2006) The pericellular matrix as a transducer of biomechanical and biochemical signals in articular cartilage. Ann N Y Acad Sci 1068:498-512.

Guilak F, Erickson GR, Ting-Beall HP (2002) The effects of osmotic stress on the viscoelastic and physical properties of articular chondrocytes. Biophys J 82:720-727.

Guilak F, Ratcliffe A, Lane N, Rosenwasser MP, Mow VC (1994) Mechanical and biochemical changes in the superficial zone of articular cartilage in canine experimental osteoarthritis. J Orthop Res 12:474-484.

Guilak F, Tedrow JR, Burgkart R (2000) Viscoelastic properties of the cell nucleus. Biochem Biophys Res Commun 269:781-786.

Gushue DL, Houck J, Lerner AL (2005) Rabbit knee joint biomechanics: motion analysis and modeling of forces during hopping. J Orthop Res 23:735-742.

Haider MA, Guilak F (2000) An axisymmetric boundary integral model for incompressible linear viscoelasticity: application to the micropipette aspiration contact problem. J Biomech Eng 122:236-244.

Han L, Grodzinsky AJ, Ortiz C (2011) Nanomechanics of the Cartilage Extracellular Matrix. Annu Rev Mater Res 41:133-168.

Han SK, Seerattan R, Herzog W (2010) Mechanical loading of in situ chondrocytes in lapine retropatellar cartilage after anterior cruciate ligament transection. J R Soc Interface 7:895-903.

Harding JW, Sneddon IN (1945) The elastic stresses produced by the indentation of the plane surface of a semi-infinite elastic solid by a rigid punch. Mathematical Proceedings of the Cambridge Philosophical Society 41:16-26.

Harris AR, Charras GT (2011) Experimental validation of atomic force microscopy-based cell elasticity measurements. Nanotechnology 22:345102.

Hayami T, Pickarski M, Zhuo Y, Wesolowski GA, Rodan GA, Duong le T (2006) Characterization of articular cartilage and subchondral bone changes in the rat anterior cruciate ligament transection and meniscectomized models of osteoarthritis. Bone 38:234-243.

Hayes WC, Keer LM, Herrmann G, Mockros LF (1972) A mathematical analysis for indentation tests of articular cartilage. J Biomech 5:541-551.

Henrotin Y, Pesesse L, Sanchez C (2009) Subchondral bone in osteoarthritis physiopathology: state-of-the art and perspectives. Biomed Mater Eng 19:311-316.

Herberhold C, Faber S, Stammberger T, Steinlechner M, Putz R, Englmeier KH, Reiser M, Eckstein F (1999) In situ measurement of articular cartilage deformation in intact femoropatellar joints under static loading. J Biomech 32:1287-1295.

Herzog W, Diet S, Suter E, Mayzus P, Leonard TR, Muller C, Wu JZ, Epstein M (1998) Material and functional properties of articular cartilage and patellofemoral contact mechanics in an experimental model of osteoarthritis. J Biomech 31:1137-1145.

Hildebrand T, Ruegsegger P (1997) Quantification of Bone Microarchitecture with the Structure Model Index. Comput Methods Biomech Biomed Engin 1:15-23.

Hochmuth RM (2000) Micropipette aspiration of living cells. J Biomech 33:15-22.

Hotta H, Yamada H, Takaishi H, Abe T, Morioka H, Kikuchi T, Fujikawa K, Toyama Y (2005) Type II collagen synthesis in the articular cartilage of a rabbit model of osteoarthritis: expression of type II collagen C-propeptide and mRNA especially during early-stage osteoarthritis. J Orthop Sci 10:595-607.

Hwang WS, Li B, Jin LH, Ngo K, Schachar NS, Hughes GN (1992) Collagen fibril structure of normal, aging, and osteoarthritic cartilage. J Pathol 167:425-433.

Intema F, Hazewinkel HA, Gouwens D, Bijlsma JW, Weinans H, Lafeber FP, Mastbergen SC (2010) In early OA, thinning of the subchondral plate is directly related to cartilage damage: results from a canine ACLT-meniscectomy model. Osteoarthritis Cartilage 18:691-698.

Isaksson H, Toyras J, Hakulinen M, Aula AS, Tamminen I, Julkunen P, Kroger H, Jurvelin JS (2011) Structural parameters of normal and osteoporotic human trabecular bone are affected differently by microCT image resolution. Osteoporos Int 22:167-177.

Janmey PA, Georges PC, Hvidt S, YuLi W, Dennis ED, 2007. Basic rheology for biologists. In: Anonymous Methods in Cell Biology. Academic Press, 3-27.

Janovjak H, Struckmeier J, Muller DJ (2005) Hydrodynamic effects in fast AFM single-molecule force measurements. Eur Biophys J 34:91-96.

Jones WR, Ting-Beall HP, Lee GM, Kelley SS, Hochmuth RM, Guilak F (1999) Alterations in the Young's modulus and volumetric properties of chondrocytes isolated from normal and osteoarthritic human cartilage. J Biomech 32:119-127.

Judex S, Gross TS, Bray RC, Zernicke RF (1997) Adaptation of bone to physiological stimuli. J Biomech 30:421-429.

Julkunen P, Korhonen RK, Herzog W, Jurvelin JS (2008) Uncertainties in indentation testing of articular cartilage: a fibril-reinforced poroviscoelastic study. Med Eng Phys 30:506-515.

Jurvelin J, Kiviranta I, Tammi M, Helminen JH (1986) Softening of canine articular cartilage after immobilization of the knee joint. Clin Orthop Relat Res (207):246-252.

Kempson GE, Freeman MA, Swanson SA (1968) Tensile properties of articular cartilage. Nature 220:1127-1128.

Koay EJ, Shieh AC, Athanasiou KA (2003) Creep indentation of single cells. J Biomech Eng 125:334-341.

Kohler T, Stauber M, Donahue LR, Muller R (2007) Automated compartmental analysis for high-throughput skeletal phenotyping in femora of genetic mouse models. Bone 41:659-667.

Kojima H, Ishijima A, Yanagida T (1994) Direct measurement of stiffness of single actin filaments with and without tropomyosin by in vitro nanomanipulation. Proc Natl Acad Sci USA 91:12962-12966.

Korhonen RK, Laasanen MS, Toyras J, Lappalainen R, Helminen HJ, Jurvelin JS (2003) Fibril reinforced poroelastic model predicts specifically mechanical behavior of normal, proteoglycan depleted and collagen degraded articular cartilage. J Biomech 36:1373-1379.

Korhonen RK, Laasanen MS, Toyras J, Rieppo J, Hirvonen J, Helminen HJ, Jurvelin JS (2002) Comparison of the equilibrium response of articular cartilage in unconfined compression, confined compression and indentation. J Biomech 35:903-909.

Korvick DL, Pijanowski GJ, Schaeffer DJ (1994) Three-dimensional kinematics of the intact and cranial cruciate ligament-deficient stifle of dogs. J Biomech 27:77-87.

Kuhn JL, Goldstein SA, Feldkamp LA, Goulet RW, Jesion G (1990) Evaluation of a microcomputed tomography system to study trabecular bone structure. J Orthop Res 8:833-842.

Kuroki K, Cook CR, Cook JL (2011) Subchondral bone changes in three different canine models of osteoarthritis. Osteoarthritis Cartilage 19:1142-1149.

Kuznetsova TG, Starodubtseva MN, Yegorenkov NI, Chizhik SA, Zhdanov RI (2007) Atomic force microscopy probing of cell elasticity. Micron 38:824-833.

Laasanen MS, Toyras J, Korhonen RK, Rieppo J, Saarakkala S, Nieminen MT, Hirvonen J, Jurvelin JS (2003) Biomechanical properties of knee articular cartilage. Biorheology 40:133-140.

Ladjal H, Hanus JL, Pillarisetti A, Keefer C, Ferreira A, Desai JP (2009) Atomic force microscopy-based single-cell indentation: Experimentation and finite element simulation. Intelligent Robots and Systems, 2009 IROS 2009 IEEE/RSJ International Conference, 1326-1332.

Lai WM, Hou JS, Mow VC (1991a) A triphasic theory for the swelling and deformation behaviors of articular cartilage. J Biomech Eng 113:245-258.

Lai WM, Hou JS, Mow VC (1991b) A triphasic theory for the swelling and deformation behaviors of articular cartilage. J Biomech Eng 113:245-258.

Langelier E, Suetterlin R, Hoemann CD, Aebi U, Buschmann MD (2000) The chondrocyte cytoskeleton in mature articular cartilage: structure and distribution of actin, tubulin, and vimentin filaments. J Histochem Cytochem 48:1307-1320.

Layton MW, Goldstein SA, Goulet RW, Feldkamp LA, Kubinski DJ, Bole GG (1988) Examination of subchondral bone architecture in experimental osteoarthritis by microscopic computed axial tomography. Arthritis Rheum 31:1400-1405.

Lee H, Ferrer JM, Lang MJ, Kamm RD (2010) Molecular origin of strain softening in cross-linked F-actin networks. Phys Rev E Stat Nonlin Soft Matter Phys 82:911-919.

Leipzig ND, Athanasiou KA (2005) Unconfined creep compression of chondrocytes. J Biomech 38:77-85.

Leo BM, Turner MA, Diduch DR (2004) Split-line pattern and histologic analysis of a human osteochondral plug graft. Arthroscopy 20 Suppl 2:39-45.

Li X, Bhushan B, Takashima K, Baek CW, Kim YK (2003) Mechanical characterization of micro/nanoscale structures for MEMS/NEMS applications using nanoindentation techniques. Ultramicroscopy 97:481-494.

Lieleg O, Schmoller KM, Claessens MM, Bausch AR (2009) Cytoskeletal polymer networks: viscoelastic properties are determined by the microscopic interaction potential of cross-links. Biophys J 96:4725-4732.

Lin DC, Dimitriadis EK, Horkay F (2007a) Robust strategies for automated AFM force curve analysis--I. Non-adhesive indentation of soft, inhomogeneous materials. J Biomech Eng 129:430-440.

Lin DC, Dimitriadis EK, Horkay F (2007b) Robust strategies for automated AFM force curve analysis-II: adhesion-influenced indentation of soft, elastic materials. J Biomech Eng 129:904-912.

Lorenz H, Wenz W, Ivancic M, Steck E, Richter W (2005) Early and stable upregulation of collagen type II, collagen type I and YKL40 expression levels in cartilage during early experimental osteoarthritis occurs independent of joint location and histological grading. Arthritis Res Ther 7:R156-65.

Lu XL, Mow VC (2008) Biomechanics of articular cartilage and determination of material properties. Med Sci Sports Exerc 40:193-199.

Mäkelä JT, Rezaeian ZS, Mikkonen S, Madden R, Han SK, Jurvelin JS, Herzog W, Korhonen RK (2014) Site-dependent changes in structure and function of lapine articular cartilage 4 weeks after anterior cruciate ligament transection. Osteoarthritis Cartilage in press.

Mäkitalo J, Saarakkala S, Rieppo L, Han S, Herzog W, Korhonen RK (2011) Can collagen fibrillation or preoteoglycan depletion of cartilage explain changed deformation behaviour of chondrocytes 9 weeks after anterior cruciate ligament transection? Trans Orthop Soc 36:2026.

Malo MK, Rohrbach D, Isaksson H, Toyras J, Jurvelin JS, Tamminen IS, Kroger H, Raum K (2013) Longitudinal elastic properties and porosity of cortical bone tissue vary with age in human proximal femur. Bone 53:451-458.

Mankin HJ, Dorfman H, Lippiello L, Zarins A (1971) Biochemical and metabolic abnormalities in articular cartilage from osteo-arthritic human hips. II. Correlation of morphology with biochemical and metabolic data. J Bone Joint Surg Am 53:523-537.

Marijnissen AC, van Roermund PM, TeKoppele JM, Bijlsma JW, Lafeber FP (2002) The canine 'groove' model, compared with the ACLT model of osteoarthritis. Osteoarthritis Cartilage 10:145-155.

Maroudas A, 1979. Physiochemical properties of articular cartilage. In: Freeman MAR (Eds.), Adult Articular Cartilage. Cambridge University Press, United Kingdom, 215-290

Maroudas A (1975) Glycosaminoglycan turn-over in articular cartilage. Philos Trans R Soc Lond B Biol Sci 271:293-313.

Maroudas A, Venn M (1977) Chemical composition and swelling of normal and osteoarthrotic femoral head cartilage. II. Swelling. Ann Rheum Dis 36:399-406.

Maroudas A, Ziv I, Weisman N, Venn M (1985) Studies of hydration and swelling pressure in normal and osteoarthritic cartilage. Biorheology 22:159-169.

Marti O, Ruf A, Hipp M, Bielefeldt H, Colchero J, Mlynek J (1992) Mechanical and thermal effects of laser irradiation on force microscope cantilevers. Ultramicroscopy 42-44:345-350.

Martin-Badosa E, Elmoutaouakkil A, Nuzzo S, Amblard D, Vico L, Peyrin F (2003) A method for the automatic characterization of bone architecture in 3D mice microtomographic images. Comput Med Imaging Graph 27:447-458.

Matsui H, Shimizu M, Tsuji H (1997) Cartilage and subchondral bone interaction in osteoarthrosis of human knee joint: a histological and histomorphometric study. Microsc Res Tech 37:333-342.

Matyas JR, Ehlers PF, Huang D, Adams ME (1999) The early molecular natural history of experimental osteoarthritis. I. Progressive discoordinate expression of aggrecan and type II procollagen messenger RNA in the articular cartilage of adult animals. Arthritis Rheum 42:993-1002.

McDevitt CA, Muir H (1976) Biochemical changes in the cartilage of the knee in experimental and natural osteoarthritis in the dog. J Bone Joint Surg Br 58:94-101.

McGlashan SR, Cluett EC, Jensen CG, Poole CA (2008) Primary cilia in osteoarthritic chondrocytes: from chondrons to clusters. Dev Dyn 237:2013-2020.

Meachim G, Stockwell RA, 1973. The matrix. In: Freeman, M.A.R. (Ed.), Adult Articular Cartilage. Alden Press, Oxford, England.

Minns RJ, Steven FS (1977) The collagen fibril organization in human articular cartilage. J Anat 123:437-457.

Moeendarbary E, Valon L, Fritzsche M, Harris AR, Moulding DA, Thrasher AJ, Stride E, Mahadevan L, Charras GT (2013) The cytoplasm of living cells behaves as a poroelastic material. Nat Mater 12:253-261.

Mow VC, Ratcliffe A, 1997. Structure and Function of Articular Cartilage and Meniscus. In: Mow, VC, Hayes, WC (Eds.) Basic Orthopaedic Biomechanics. Lippincott-Raven, 113-177.

Mow VC, Gu WY, Chen FH, 2005. Structure and function of articular cartilage and meniscus. In: Mow VC, Huiskes R, (Eds.), Orthopaedic Biomechanics and Mechano-Biology. Lippincott Williams & Wilkins, 181-258.

Mow VC, Proctor CS, Kelly MA, 1989. Biomechanics of Articular Cartilage. In: Nordin M, Frankel VH, (Eds.), Basic Biomechanics of the Musculoskeletal System. Lea and Febiger, Philadelphia, 31-57.

Mow VC, Ateshian GA, 1997. Friction, Lubrication, and Wear of Diarthrodial Joints. In: Mow VC, Hayes WC (Eds.) Basic Orthopaedic Biomechanics. Raven Press, New York, 273-315.

Mow VC, Holmes MH, Lai WM (1984) Fluid transport and mechanical properties of articular cartilage: a review. J Biomech 17:377-394.

Mow VC, Kuei SC, Lai WM, Armstrong CG (1980) Biphasic creep and stress relaxation of articular cartilage in compression? Theory and experiments. J Biomech Eng 102:73-84.

Mow VC, Wang CC, Hung CT (1999) The extracellular matrix, interstitial fluid and ions as a mechanical signal transducer in articular cartilage. Osteoarthritis Cartilage 7:41-58.

Muir H, Bullough P, Maroudas A (1970) The distribution of collagen in human articular cartilage with some of its physiological implications. J Bone Joint Surg Br 52:554-563.

Muller FJ, Setton LA, Manicourt DH, Mow VC, Howell DS, Pita JC (1994) Centrifugal and biochemical comparison of proteoglycan aggregates from articular cartilage in experimental joint disuse and joint instability. J Orthop Res 12:498-508.

Murray CJ, Lopez AD (1996) Evidence-based health policy--lessons from the Global Burden of Disease Study. Science 274:740-743.

Naumann D, Helm D, Labischinski H (1991) Microbiological characterizations by FT-IR spectroscopy. Nature 351:81-82.

Nayar VT, Weiland JD, Nelson CS, Hodge AM (2012) Elastic and viscoelastic characterization of agar. J Mech Behav Biomed Mater 7:60-68.

Neumeister JM, Ducker WA (1994) Lateral, normal, and longitudinal spring constants of atomic force microscopy cantilevers. Review of Scientific Instruments 65:2527-2531.

Ng L, Hung HH, Sprunt A, Chubinskaya S, Ortiz C, Grodzinsky A (2007) Nanomechanical properties of individual chondrocytes and their developing growth factor-stimulated pericellular matrix. J Biomech 40:1011-1023.

Nigg BM, Herzog W, 2007. Joints. In: Nigg, B.M., Herzog, W. (Eds.) Biomechanics of the Musculoskeletal System. John Wiley & Sons, Chichester, West Sussex, England, 244-291.

Nitta T, Haga H, Kawabata K, Abe K, Sambongi T (2000) Comparing microscopic with macroscopic elastic properties of polymer gel. Ultramicroscopy 82:223-226.

O'Connor BL, Visco DM, Heck DA, Myers SL, Brandt KD (1989) Gait alterations in dogs after transection of the anterior cruciate ligament. Arthritis Rheum 32:1142-1147.

Odenbring S, Egund N, Lindstrand A, Lohmander LS, Willen H (1992) Cartilage regeneration after proximal tibial osteotomy for medial gonarthrosis. An arthroscopic, roentgenographic, and histologic study. Clin Orthop Relat Res (277):210-216.

Ofek G, Natoli RM, Athanasiou KA (2009a) In situ mechanical properties of the chondrocyte cytoplasm and nucleus. J Biomech 42:873-877.

Ofek G, Wiltz DC, Athanasiou KA (2009b) Contribution of the cytoskeleton to the compressive properties and recovery behavior of single cells. Biophys J 97:1873-1882.

Ohler B (2007) Cantilever spring constant calibration using laser Doppler vibrometry. Rev Sci Instrum 78.

Oswald ES, Chao PH, Bulinski JC, Ateshian GA, Hung CT (2008) Dependence of zonal chondrocyte water transport properties on osmotic environment. Cell Mol Bioeng 1:339-348.

Özkaya N, Nordin M, 1999. Fundamentals of biomechanics: equilibrium, motion and deformation. In: Leger DL, (Ed.), Springer, New York.

Parfitt AM, Drezner MK, Glorieux FH, Kanis JA, Malluche H, Meunier PJ, Ott SM, Recker RR (1987) Bone histomorphometry: standardization of nomenclature, symbols, and units. Report of the ASBMR Histomorphometry Nomenclature Committee. J Bone Miner Res 2:595-610.

Park S, Costa KD, Ateshian GA (2004) Microscale frictional response of bovine articular cartilage from atomic force microscopy. J Biomech 37:1679-1687.

Park S, Goodman MB, Pruitt BL (2005) Measurement of mechanical properties of Caenorhabditis elegans with a piezoresistive microcantilever system. Microtechnology in Medicine and Biology, 2005 3rd IEEE/EMBS Special Topic Conference , 400-403.

Parkinson IH, Badiei A, Fazzalari NL (2008) Variation in segmentation of bone from micro-CT imaging: implications for quantitative morphometric analysis. Australas Phys Eng Sci Med 31:160-164.

Plaas A, Osborn B, Yoshihara Y, Bai Y, Bloom T, Nelson F, Mikecz K, Sandy JD (2007) Aggrecanolysis in human osteoarthritis: confocal localization and biochemical characterization of ADAMTS5-hyaluronan complexes in articular cartilages. Osteoarthritis Cartilage 15:719-734.

Pogoda K, Jaczewska J, Wiltowska-Zuber J, Klymenko O, Zuber K, Fornal M, Lekka M (2012) Depth-sensing analysis of cytoskeleton organization based on AFM data. Eur Biophys J 41:79-87.

Poole CA (1997) Articular cartilage chondrons: form, function and failure. J Anat 191 (Pt 1):1-13.

Pritzker KP, Gay S, Jimenez SA, Ostergaard K, Pelletier JP, Revell PA, Salter D, van den Berg WB (2006) Osteoarthritis cartilage histopathology: grading and staging. Osteoarthritis Cartilage 14:13-29.

Qu CJ, Karjalainen HM, Helminen HJ, Lammi MJ (2006) The lack of effect of glucosamine sulphate on aggrecan mRNA expression and (35)S-sulphate incorporation in bovine primary chondrocytes. Biochim Biophys Acta 1762:453-459.

Quinteiro Rodríguez MP (2000) Fourier Transform Infrared (FTIR) Technology for the Identification of Organisms. Clin Microbiol Newsl 22:57-61.

Radin EL, Burr DB, Caterson B, Fyhrie D, Brown TD, Boyd RD (1991) Mechanical determinants of osteoarthrosis. Semin Arthritis Rheum 21:12-21.

Radin EL, Paul IL, Lowy M (1970a) A comparison of the dynamic force transmitting properties of subchondral bone and articular cartilage. J Bone Joint Surg Am 52:444-456.

Radin EL, Paul IL, Tolkoff MJ (1970b) Subchondral bone changes in patients with early degenerative joint disease. Arthritis Rheum 13:400-405.

Radmacher M (2007) Studying the mechanics of cellular processes by atomic force microscopy. Methods Cell Biol 83:347-372.

Radmacher M, Fritz M, Hansma PK (1995) Imaging soft samples with the atomic force microscope: gelatin in water and propanol. Biophys J 69:264-270.

Radmacher M, Tillmann RW, Gaub HE (1993) Imaging viscoelasticity by force modulation with the atomic force microscope. Biophys J 64:735-742.

Rantakokko J, Uusitalo H, Jamsa T, Tuukkanen J, Aro HT, Vuorio E (1999) Expression profiles of mRNAs for osteoblast and osteoclast proteins as

indicators of bone loss in mouse immobilization osteopenia model. J Bone Miner Res 14:1934-1942.

Ratcliffe A, Mow VC, 1991. The structure, function and biologic repair of articular cartilage. In: Friedlaender, G.E., Goldberg, V.M. (Eds.) Bone and Cartilage Allografts. American Academy of Orthopaedic Surgeons, Park Ridge, pp. 123-154.

Reimann I, Mankin HJ, Trahan C (1977) Quantitative histologic analyses of articular cartilage and subchondral bone from osteoarthritic and normal human hips. Acta Orthop Scand 48:63-73.

Rico F, Roca-Cusachs P, Gavara N, Farre R, Rotger M, Navajas D (2005) Probing mechanical properties of living cells by atomic force microscopy with blunted pyramidal cantilever tips. Phys Rev E Stat Nonlin Soft Matter Phys 72:021914.

Rieppo J, Hallikainen J, Jurvelin JS, Kiviranta I, Helminen HJ, Hyttinen MM (2008) Practical considerations in the use of polarized light microscopy in the analysis of the collagen network in articular cartilage. Microsc Res Tech 71:279-287.

Rieppo J, Hyttinen MM, Jurvelin JS, Helminen HJ (2004) Reference sample method reduces the error caused by variable cryosection thickness in Fourier transform infrared imaging. Appl Spectrosc 58:137-140.

Rivlin RS (1949) Large Elastic Deformations of Isotropic Materials. VI. Further Results in the Theory of Torsion, Shear and Flexure. Philosophical Transactions of the Royal Society of London Series A, Mathematical and Physical Sciences 242:173-195.

Rogart JN, Barrach HJ, Chichester CO (1999) Articular collagen degradation in the Hulth-Telhag model of osteoarthritis. Osteoarthritis Cartilage 7:539-547.

Roth V, Mow VC (1980) The intrinsic tensile behavior of the matrix of bovine articular cartilage and its variation with age. J Bone Joint Surg Am 62:1102-1117.

Rotsch C, Braet F, Wisse E, Radmacher M (1997) AFM imaging and elasticity measurements on living rat liver macrophages. Cell Biol Int 21:685-696.

Ruegsegger P, Koller B, Muller R (1996) A microtomographic system for the nondestructive evaluation of bone architecture. Calcif Tissue Int 58:24-29.

Saarakkala S, Julkunen P, Kiviranta P, Makitalo J, Jurvelin JS, Korhonen RK (2010) Depth-wise progression of osteoarthritis in human articular cartilage: investigation of composition, structure and biomechanics. Osteoarthritis Cartilage 18:73-81.

Sacksteder C, Barry BA (2001) Fourier transform infrared spectroscopy: A molecular approach to an organismal question. J Phycol 37:197-199.

Sader JE (1995) Parallel beam approximation for V-shaped atomic force microscope cantilevers. Review of Scientific Instruments 66:4583-4587.

Sader JE, Chon JWM, Paul M (1999) Calibration of rectangular atomic force microscope cantilevers. Review of Scientific Instruments 70:3967-3969.

Sah RL, Yang AS, Chen AC, Hant JJ, Halili RB, Yoshioka M, Amiel D, Coutts RD (1997) Physical properties of rabbit articular cartilage after transection of the anterior cruciate ligament. J Orthop Res 15:197-203.

Sato M, Theret DP, Wheeler LT, Ohshima N, Nerem RM (1990) Application of the micropipette technique to the measurement of cultured porcine aortic endothelial cell viscoelastic properties. J Biomech Eng 112:263-268.

Setton LA, Mow VC, Muller FJ, Pita JC, Howell DS (1994) Mechanical properties of canine articular cartilage are significantly altered following transection of the anterior cruciate ligament. J Orthop Res 12:451-463.

Shakibaei M, Csaki C, Mobasheri A (2008) Diverse Roles of Integrins Receptors in Articular Cartilage. Springer Verlag, Berlin.
Shieh AC, Athanasiou KA (2006) Biomechanics of single zonal chondrocytes. J Biomech 39:1595-1602.
Shimizu M, Tsuji H, Matsui H, Katoh Y, Sano A (1993) Morphometric analysis of subchondral bone of the tibial condyle in osteoarthrosis. Clin Orthop Relat Res (293):229-239.
Shin D, Athanasiou K (1999) Cytoindentation for obtaining cell biomechanical properties. J Orthop Res 17:880-890.
Shinto H, Aso Y, Fukasawa T, Higashitani K (2012) Adhesion of melanoma cells to the surfaces of microspheres studied by atomic force microscopy. Colloids Surf B Biointerfaces 91:114-121.
Sniekers YH, Intema F, Lafeber FP, van Osch GJ, van Leeuwen JP, Weinans H, Mastbergen SC (2008) A role for subchondral bone changes in the process of osteoarthritis; a micro-CT study of two canine models. BMC Musculoskelet Disord 9:20-2474-9-20.
Steklov N, Srivastava A, Sung KL, Chen PC, Lotz MK, D'Lima DD (2009) Aging-related differences in chondrocyte viscoelastic properties. Mol Cell Biomech 6:113-119.
Stockwell RA (1991) Cartilage failure in osteoarthritis: Relevance of normal structure and function. A review. Clinical Anatomy 4:161-191.
Stolz M, Raiteri R, Daniels AU, VanLandingham MR, Baschong W, Aebi U (2004) Dynamic elastic modulus of porcine articular cartilage determined at two different levels of tissue organization by indentation-type atomic force microscopy. Biophys J 86:3269-3283.
Stoop R, Buma P, van der Kraan PM, Hollander AP, Billinghurst RC, Meijers TH, Poole AR, van den Berg WB (2001) Type II collagen degradation in articular cartilage fibrillation after anterior cruciate ligament transection in rats. Osteoarthritis Cartilage 9:308-315.
Storm C, Pastore JJ, MacKintosh FC, Lubensky TC, Janmey PA (2005) Nonlinear elasticity in biological gels. Nature 435:191-194.
Tammi M, Saamanen AM, Jauhiainen A, Malminen O, Kiviranta I, Helminen H (1983) Proteoglycan alterations in rabbit knee articular cartilage following physical exercise and immobilization. Connect Tissue Res 11:45-55.
Theret DP, Levesque MJ, Sato M, Nerem RM, Wheeler LT (1988) The application of a homogeneous half-space model in the analysis of endothelial cell micropipette measurements. J Biomech Eng 110:190-199.
Ting TCT (1966) The Contact Stresses Between a Rigid Indenter and a Viscoelastic Half-Space. Journal of Applied Mechanics 33:845-854.
Trickey WR, Baaijens FP, Laursen TA, Alexopoulos LG, Guilak F (2006) Determination of the Poisson's ratio of the cell: recovery properties of chondrocytes after release from complete micropipette aspiration. J Biomech 39:78-87.
Trickey WR, Lee GM, Guilak F (2000) Viscoelastic properties of chondrocytes from normal and osteoarthritic human cartilage. J Orthop Res 18:891-898.
Trickey WR, Vail TP, Guilak F (2004) The role of the cytoskeleton in the viscoelastic properties of human articular chondrocytes. J Orthop Res 22:131-139.
Tripathy S, Berger EJ (2009) Measuring viscoelasticity of soft samples using atomic force microscopy. J Biomech Eng 131:094507.

Turunen SM, Han SK, Herzog W, Korhonen RK (2013) Cell deformation behavior in mechanically loaded rabbit articular cartilage 4 weeks after anterior cruciate ligament transection. Osteoarthritis Cartilage 21:505-513.

Urban JP (1994) The chondrocyte: a cell under pressure. Br J Rheumatol 33:901-908.

Vargas-Pinto R, Gong H, Vahabikashi A, Johnson M (2013) The Effect of the Endothelial Cell Cortex on Atomic Force Microscopy Measurements. Biophys J 105:300-309.

Vignon E, Bejui J, Mathieu P, Hartmann JD, Ville G, Evreux JC, Descotes J (1987) Histological cartilage changes in a rabbit model of osteoarthritis. J Rheumatol 14 Spec No:104-106.

Waarsing JH, Day JS, Weinans H (2004) An improved segmentation method for in vivo microCT imaging. J Bone Miner Res 19:1640-1650.

Walters DA, Cleveland JP, Thomson NH, Hansma PK, Wendman MA, Gurley G, Elings V (1996) Short cantilevers for atomic force microscopy. Review of Scientific Instruments 67:3583-3590.

Wang N, Butler JP, Ingber DE (1993) Mechanotransduction across the cell surface and through the cytoskeleton. Science 260:1124-1127.

Wang SX, Laverty S, Dumitriu M, Plaas A, Grynpas MD (2007) The effects of glucosamine hydrochloride on subchondral bone changes in an animal model of osteoarthritis. Arthritis Rheum 56:1537-1548.

Weisenhorn AL, Maivald P, Butt H, Hansma PK (1992) Measuring adhesion, attraction, and repulsion between surfaces in liquids with an atomic-force microscope. Phys Rev B Condens Matter 45:11226-11232.

Wilkins RJ, Browning JA, Ellory JC (2000) Surviving in a matrix: membrane transport in articular chondrocytes. J Membr Biol 177:95-108.

Wilson W, van Donkelaar CC, van Rietbergen B, Huiskes R (2005) A fibril-reinforced poroviscoelastic swelling model for articular cartilage. J Biomech 38:1195-1204.

Woolf AD, Pfleger B (2003) Burden of major musculoskeletal conditions. Bull World Health Organ 81:646-656.

Wright M, Jobanputra P, Bavington C, Salter DM, Nuki G (1996) Effects of intermittent pressure-induced strain on the electrophysiology of cultured human chondrocytes: evidence for the presence of stretch-activated membrane ion channels. Clin Sci (Lond) 90:61-71.

Wu JZ, Herzog W, Epstein M (2000) Joint contact mechanics in the early stages of osteoarthritis. Med Eng Phys 22:1-12.

Yaszemski MJ, Payne RG, Hayes WC, Langer R, Mikos AG (1996) Evolution of bone transplantation: molecular, cellular and tissue strategies to engineer human bone. Biomaterials 17:175-185.

Yoneda T, 1993. Cytokines in bone: local translators in cell-to-cell communications. In: Noda, M. (Ed.), Cellular and Molecular Biology of Bone. Academic Press Limited, San Diego, pp. 375-412.

Yoshioka M, Coutts RD, Amiel D, Hacker SA (1996) Characterization of a model of osteoarthritis in the rabbit knee. Osteoarthritis Cartilage 4:87-98.